Probing Coherent States and Nonlinear Properties in Multifunctional Material Systems

Rathsara Rasanjalee Herath Herath Mudiyanselage

Dissertation submitted to the Faculty of the

Virginia Polytechnic Institute and State University

in partial fulfillment of the requirements for the degree of

Doctor of Philosophy

in

Physics

Giti A. Khodaparast, Chair

Vinh Nguyen

Sophia Economou

Satoru Emori

March 19, 2021

Blacksburg, Virginia

Keywords: Time Resolved Spectroscopy, Mutiferroics, Ferroelectrics, Piezolectrics, Coherent Phonons, Magnons, Second Harmonic Generation, Hot Carrier Absorber, InAsP Films

Copyright 2021, Rathsara Rasanjalee Herath Herath Mudiyanselage

Probing Coherent States and Nonlinear Properties in Multifunctional Material Systems

Rathsara Rasanjalee Herath Herath Mudiyanselage

(ABSTRACT)

The rapid progress on developing new and improved multifunctional materials, for optoelectronic and spin based phenomena/devices, have increased the importance of the fundamental understanding of their coherent states and nonlinear optical properties. This study is aimed at characterizing, modeling, and controlling the fundamental electronic, phononic, and spin properties of several classes of materials through nonequilibrium and nonlinear light-matter interactions, coupled with a novel design of the material phases, interfaces, and heterostructures. This research directly addresses the Grand Challenges identified in the Basic Energy Sciences Advisory Committee report "Directing Matter and Energy: Five Challenges for Science and the Imagination" (Hemminger, 2007) [1], in particular, the area: "*Matter far beyond equilibrium" and addresses the questions, "How do remarkable properties of matter emerge from complex correlations of the atomic or electronic constituents and how can we control these properties?" and "How do we design and perfect atom- and energy-efficient synthesis of revolutionary new forms of matter with tailored properties?*". The knowledge gained from these fundamental studies can provide new information for a broad community to provide concepts for the next generation of multifunctional materials and devices, and resulted in several publications and conference presentations. The materials studied in this dissertation included multiferroic $BaTiO_3$-$BiFeO_3$ [2], ferroelectric $Pb_{0.52}Zr_{0.48}TiO_3$ (PZT), InAs/AlAsSb multi-quantum-well [3], lead halide perovskite [4], n-type InAsP films [5, 6], and nanolaminate plasmonic crystals [7].

Probing multiferroics, which are materials that can exhibit ferromagnetic, ferroelectric, and

ferroelastic orders simultaneously in a single phase, was a main focus of this study. $BiFeO_3$ (BFO) is the most widely investigated multiferroic due to its high Neel and Curie temperatures and has antiferromagnetic and ferroelectric properties [8]. An inherent drawback of BFO is its large leakage currents. In this project, $(1-x)BaTiO_3$-$(x)BiFeO_3$, $x = 0.725$ (BTO-BFO) heterostructures were investigated [9], where the conductivity of the solid solution can be reduced by adding another perovskite material, $BaTiO_3$ [2]. We aimed to study optically induced coherent states in our BTO-BFO structures. Time resolved pump-probe spectroscopic measurements were performed at room temperature as well as at low temperature (100 K) up to 10 T. Coherent acoustic phonons were observed both in a film and nanorods, resulting in coherent phonon frequencies of 27 and 33 GHz, respectively [2]. Coherent phonon spectroscopy is a sensitive tool to characterize the interfaces and can be employed as an effective ultrasensitive quantum sensor [10]. Furthermore, in the nanorods arrays of BTO-BFO, an additional oscillation with frequency in the range of 8.1 GHz was observed. This frequency is close to a theoretically predicted magnon frequency which could indicate the coexistence of coherent phonons and magnons in the nanorods arrays [2]. In an analogy to photonics which relies on electromagnetic waves, magnonics utilizes spin waves to carry and process information, offering several advantages such as an operation frequency in the THz range. Recently, "*a quantum tango*" [11] was reported where coupled coherent magnon and phonons modes were formed on a surface patterned ferromagnet.

Furthermore, BTO-BFO heterostructures were probed using transient birefringence and magneto-optical Kerr effect spectroscopy. The results demonstrated that the magnetic field dependence of coherent phonons, measured by these two techniques, exhibits more sensitivity to the external magnetic fields compared to the differential reflectivity technique [2]. Moreover, nonlinear optical properties of this structure were investigated via second harmonic generation spectroscopy, where wavelength and polarization dependence of this nonlinear

observation will be discussed in this dissertation.

As part of this study, another class of multiferroic materials, with strong ferroelectric and piezoelectric properties, $Pb_{0.52}Zr_{0.48}TiO_3$ (PZT) was studied [12]. In this project, the nonlinear optical properties of PZT nanorod arrays were investigated. Clear signatures of second harmonic generations from 490-525 nm (2.38-2.53 eV) at room temperature, were observed. Furthermore, time resolved differential reflectivity measurements were performed to study dynamical properties in the range of 690-1000 nm where multiphoton processes were responsible for the photoexcitations. We compared this excitation scheme, which is sensitive mainly to the surface states, to when the photoexcited energy ($\sim$ 3.1 eV) was close to the bandgap of the nanorods. Our results offer promises for employing these nanostructures in nonlinear photonic applications. Furthermore, the established techniques during my research provided new insights on optical properties of InAs/AlAsSb multi-quantum-well [3], lead halide perovskite [4], n-type InAsP films [5, 6], and nanolaminate plasmonic crystals [7], and the results will be briefly presented in this dissertation.

Probing Coherent States and Nonlinear Properties in Multifunctional Material Systems

Rathsara Rasanjalee Herath Herath Mudiyanselage

(GENERAL AUDIENCE ABSTRACT)

My research activities have explored multifunctional materials and heterostructures with strongly enhanced coupled electric and magnetic orders and optical properties. In particular, pursuing novel heterostructure designs such as multiferroics can provide control over electric and magnetic ordering in mixed dimensionality. This, together with control at the level from lattice structure to electron spin states can give rise to improved or even qualitatively new and robust materials properties. For example, a better understanding of the phenomena associated with the spin degree of freedom of electrons allows for advancement in spintronic device applications such as storage, logic, and sensors, which are associated with quantum computers and quantum communications [13, 14, 15]. Overarching questions and goals of my activities included: What are the microscopic origins and mechanisms of nonlinear response in strongly coupled nanostructured materials and its relationship to electronic, spin, and lattice degrees of freedom? (2) What are the effects of dimensionality and quantum confinement on optical properties? (3) How do we control and manipulate the coherent states, such as coherent phonons and magnons using external and internal fields, material composition, and morphology to achieve maximal efficiency and tunability? Addressing many of the challenges in the fast-paced technological world requires continued developments of new materials with enhanced optical properties. The knowledge gained from my fundamental studies can provide new information for the next generation of multifunctional materials and devices with advanced optical properties and resulted in several publications and conference presentations.

Dedication

To my family

Acknowledgments

First and foremost, I would like to convey my sincere gratitude to my advisor, Prof. Giti Khodaparast. I cannot thank you enough for your continuous assistance and encouraging involvement in every step of the way throughout the process of my doctoral studies. I could not have asked for a better mentor and would sincerely like to thank you very much for your support and understanding over these past six years, which has inspired me to become an independent researcher and helped me grasp the value of critical reasoning.

My sincere thanks must also go to the members of my Ph.D. committee, Prof. Vinh Nguyen, Prof. Sophia Economou, and Prof. Satoru Emori, for their generous advice and time to offer me valuable comments towards improving my work.

I would also like to thank, Dr. Brenden Magill, for his assistance with various projects, and for offering me valuable advice and encouragement. I also want to thank Dr. Michael Meeker for teaching and training me on how to perform various experiments.

Throughout my Ph.D. program, I had the opportunity to collaborate with many other knowledgeable fellow researchers. I would like to show my sincere appreciation to my collaborators Prof. Shashank Priya, Prof. Chris Stanton, Prof. Stephen McGill, Prof. Ian Sellers, Prof. Chris Palmstrom, and Prof. Wei Zhou for offering me their expertise and time for my scientific and technical research.

I would also like to thank all my undergraduate and graduate lab mates, John Burton, Moira

Miller, Kiara McMillan, Joe Spencer, Gabi Galliano, Ada Morral, and Nicholas Smith, for assisting me with various experiments as well as for their friendship. I would like to pay my special regards to Betty Wilkins. I whole-heartedly appreciated your great advice and guidance given to fulfill the requirements as a graduate student at Virginia Tech.

This journey which resulted in the culmination of this dissertation required more than academic support. I would like to thank my roommates and all my friends in Blacksburg and outside. I cannot begin to express my gratitude for their friendship and continuous support.

Last but not least and most importantly, none of this could have happened without the pillars of strength of my life, my parents, my husband, and my brothers. This dissertation stands as a testament to your unconditional love, support, and encouragement.

GRANT INFORMATION

This work supported by the Air Force Office of Scientific Research under award numbers: FA9550-14-1-0376, FA9550-17-1-0341, and FA9550-16-1-0358 under DURIP2016 program. Any opinions, finding, and conclusions or recommendations expressed in this material are those of the author(s) and do not necessarily reflect the views of the United States Air Force.

ATTRIBUTIONS

Chapter 3 and 4: In this project, the authorship is shared with Brenden Magill, Han Byul Kang, and Jade Holleman. The material structures were fabricated by Han Byul Kang, who was under the supervision of Shashank Priya. The high magnetic field measurements were conducted by Jade Holleman with the assistance of Steve McGill, at National High Magnetic Field Laboratory, Tallahassee. The theoretical analysis was performed by Christohper J. Stanton at the University of Florida. The project was supervised by Professor Giti Khodaparast.

Chapter 5: In this project, the authorship is shared with Min Gyu Kang, who fabricated the material under the supervision of Shashank Priya. The project was supervised by Professor Giti Khodaparast.

My research activities as a graduate student resulted in the following publications:

1- Rathsara R. H. H. Mudiyanselage, Brenden A. Magill, John Burton, Moira Miller, Joseph Spencer, Kiara McMillan, Giti A. Khodaparast, Han Byul Kang Min Gyu Kang, Deepam Maurya, Shashank Priya, Jade Holleman, Steve McGill , and Christopher J. Stanton,"Coherent Acoustic Phonons and Ultrafast Carrier Dynamics in Hetero-epitaxial $BaTiO_3$-$BiFeO_3$ Films and Nanorods", J. Mater. Chem. C, 7, 14212-14222 (2019).

2- V. Whiteside, B. Magill, M. Lumb, H. Esmaielpour, M. Meeker, R. Mudiyanselage, A. Messager, S. Vijeyaragunathan, T. Mishima, M. Santos, I. Vurgaftman, G. A. Khodaparast, I. Sellers, "Valence Band States in an InAs/AlAsSb Multi-quantum-well Hot Carrier Absorber", Semicond. Sci. Technol., 34 025005 (2019).

3- C. Wu, H. Li, Y. Yan, Bo Chi, K. M. Felice, R. B. Moore, B. A. Magill, R. R. H. H. Mudiyanselage, G. A. Khodaparast, M. Sanghadasa, and S. Priya " Highly-Stable Organo-Lead Halide Perovskites Synthesized through Green Self-Assembly Process," Advanced Science News: Solar RRL 2, 1800052 (2018), Selected for cover page.

4- M. A. Meeker, S. Kundu, D. Maurya, M-G Kang, A. Sosa, R. R. H. H. Mudiyanselage, M. Clavel, S. Gollapudi, M. K. Hudait, S. Priya, and G. A. Khodaparast, "The Permittivity and Refractive Index Measurements of Doped Barium Titanate (BT-BCN)," Optical Materials 73, 793 (2017).

5- Rathsara R. H. H. Mudiyanselage, John Burton, Brenden A. Magill, Kiara McMillan, Gabi Gagliano, Ada J. Morral, Min Gyu Kang, Han-Byul Kang, Shashank Priya, Christopher J. Stanton, Giti A. Khodaparast "Optical Properties of $Pb_{0.52}Zr_{0.48}TiO_3$ Nanorod Arrays: Second Harmonic Generation and Multiphoton Carrier Dynamics" Under review

6- Tao Ye, Ke Wang, Yuchen Hou, Dong Yang, Nicholas Smith, Brenden Magill, Jungjin Yoon, Rathsara R. H. H. Mudiyanselage, Giti A. Khodaparast, Kai Wang, Priya Shashank, "Ambient-air-stable lead-free CsSnI3 solar cells with >7.5% efficiency" Journal of American Chemical Society, 143, 11, 4319–4328 (2021).

Contents

List of Figures xvi

List of Tables xxvii

1 Introduction 1

1.1 Ultrafast Coherent Phonon Dynamics and Nonlinear Light-Matter Interactions in Multiferroic $BaTiO_3$-$BiFeO_3$ (BTO-BFO) Material Systems: 3

1.1.1 Motivation 3

1.1.2 Background: 7

1.2 Nonlinear Spectroscopy in Ferroelectric $PbZr_{1-x}Ti_xO_3$ (PZT) Material Systems 16

1.2.1 Second Harmonic Generation: 16

2 Experimental Techniques 23

2.1 Ultrafast Pump-Probe Spectroscopy 23

2.1.1 Time Resolved Differential Reflectivity Spectroscopy 26

2.1.2 Time Resolved Optically Induced Birefringence Spectroscopy 28

2.1.3 Time Resolved Magneto Optical Kerr Effect Spectroscopy 29

2.2 Non-linear Optics 31

2.2.1 Second Harmonic Generation Spectroscopy 32

3 Coherent Acoustic Phonons and Ultrafast Carrier Dynamics in Hetero-Epitaxial $BaTiO_3$-$BiFeO_3$ Films and Nanorods **34**

3.1 Introduction 35

3.2 Sample Preparation and Characterization 37

3.2.1 $BaTiO_3$-$BiFeO_3$ Films 37

3.2.2 $BaTiO_3$-$BiFeO_3$ Nanorods 41

3.3 Results and Discussion 43

3.3.1 Carrier Relaxation Dynamics in $BaTiO_3$-$BiFeO_3$ Films 44

3.3.2 Coherent Phonons in $BaTiO_3$-$BiFeO_3$ Film at Low Temperature . . . 49

3.3.3 Coherent Dynamics in $BaTiO_3$-$BiFeO_3$ Nanorods at Low Temperature 54

3.3.4 Carrier Relaxation Dynamics in $BaTiO_3$-$BiFeO_3$ Nanorods Using a Degenerate Pump-Probe Scheme 60

3.4 Conclusions 61

4 Probing Sensitivity of Longitudinal Coherent Acoustic Phonons to External Magnetic Fields in $BaTiO_3$-$BiFeO_3$ **63**

4.1 Introduction 64

4.2 Samples Characteristics 65

4.3 Results and Discussions 66

4.3.1 TROIB and TRMOKE Measurements of BTO-BFO Films 66

4.3.2 SHG in BTO-BFO Films 72

4.4 Conclusions 78

5 Optical Properties of $Pb_{0.52}Zr_{0.48}TiO_3$ Nanorod Arrays: Second Harmonic Generation and Multiphoton Carrier Dynamics 80

5.1 Introduction 81

5.2 Sample Preparation and Characterization 82

5.3 SHG in PZT Nanostructures 83

5.4 SHG: Polarization Dependence 88

5.5 Carrier Relaxation Dynamics in PZT Nanorods 91

5.6 SHG and Carrier Relaxation Dynamics in PZT Films 98

5.7 Conclusion 99

6 Contributions to Other Studies 101

6.1 TRDR Measurements of Self-Assembled $CH_3NH_3PbI_3$ Perovskites 101

6.2 Photoluminescence Measurements of InAs/AlAsSb Multi-quantum-well Hot Carrier Absorber 105

6.3 TRMOKE Measurements of InAsP Films 107

6.4 SHG and Up-conversion Luminescence Measurements of Multiresonant Nanolaminate Plasmonic Crystals 114

7 Summary and Future Works 117

Bibliography 122

Appendices **150**

Appendix A Laser Systems **151**

A.1 Ti:sapphire Oscillator 151

Appendix B Experimental setups **152**

B.1 Time Resolved Differential Reflectivity Setup 152

B.1.1 BBO Crystal 153

B.1.2 Detector 154

B.2 Time Resolved OIB and MOKE Spectroscopy Setup 154

B.2.1 Wave-plates 154

B.2.2 Wallaston Prism 156

B.3 Photoluminescence/SHG/Up-conversion Luminesence Spectroscopy Setup . . 156

B.3.1 Spectral Filters 157

B.3.2 Spectroscopy Artifacts 157

List of Figures

1.1 Multiferroics. The electric polarization (P), magnetization (M) and strain (ϵ) is a function of, the electric field (E), magnetic field (H) and stress (σ), respectively. In multiferroics, multiple ferroic orders coexist in a single phase, giving rise to coupling order parameters such as magnetoelectric coupling, where E can control the M and vice versa [16]. 8

1.2 (a) Crystal structure of $BiFeO_3$ (Perovskite structure) [17]. (b) Schematic representation of inherent spiral spin structures in $BiFeO_3$ [18]. 10

1.3 This schematic represents the coherent phonon generation and detection via pump-probe technique. The pump pulse generates an acoustic pulse at the surface that can propagate into the material at the longitudinal speed of sound in the material (V_{LS})and δz is the strain layer where the absorbed pump energy is deposited. The probe light is reflected at the surface and other regions of the sample, leading to a detection scheme similar to the Fabry-Perot interference.(b) The resultant oscillatory pattern observed in a transient reflectivity curve from a propagating coherent phonon. Adopted from data provided by Brenden Magill on GaMnAs [10]. 13

1.4 Hierarchy of functional materials, which represent the relation between ferroelectric, pyroelectric, piezoelectric, and dielectric materials. 19

2.1 Schematic representation of a photoexcitation and relaxation process in a direct gap semiconductor, where CB is the conduction band, VB the valence band, and E_g is the energy gap. Here, an electron and hole pair is generated through pulse laser excitation, and in the process of cooling down, both *non-coherent phonons* and *coherent phonons* can be generated. 24

2.2 Time resolved pump-probe setup. (a) Non-degenerate pump-probe (400 nm pump and 800 nm probe) setup with Coherent amplified Ti:sapphire oscillator with a repetition rate of 1 kHz, a wavelength of 800 nm, and a pulse duration of 100 fs. (b) Degenerate pump-probe setup with a Coherent Chameleon Ti:sapphire laser with a repetition rate of 80 MHz, a wavelength range from 700 -1050 nm and a pulse duration of 100 fs. This setup also includes a 1 T variable electromagnet. 25

2.3 (a) A schematic representation of pump and the probe beam overlapping on the sample. (b) Differential reflectivity plot for relaxation dynamics of GaAs at room temperature. We use GaAs to test our setup. 27

2.4 TRMOKE responses collected for GaAs at room temperature with a degenerate pump-probe setup. Green and blue plots reprecent the TRMOKE signal from right circularly polarized (σ^+) and left circularly polarized (σ^-) light respectively. We use GaAs to test our setup. 29

2.5 Photoluminescence experiment setup. SHG can be detected using our photoluminescence setup. 32

3.1 (a) SEM image of the layer structure of the $BaTiO_3$-$BiFeO_3$ film investigated in this study (sample 20). (b) The magnetization as a function of temperature at 0.5 T, and the inset shows FE loop at room temperature demonstrating the multiferroic nature. (c) The XRD of sample 20 shows a single phase for the $BaTiO_3$-$BiFeO_3$ film. (d) Here we present, (101) Phi-scan XRD patterns of $BaTiO_3$-$BiFeO_3$/LSMO epitaxial layers grown on (100) STO substrate (sample 20). The films are grown through (001) direction and the phi scan was performed with (101) space to evaluate the epitaxial quality. Note: The labels BTO-BFO refer to $BaTiO_3$-$BiFeO_3$. 40

3.2 (a) Schematic of the nanorods growth on spherical LSMO seed particles. The seeds were arranged using polymer nano-sphere coating followed by LSMO deposition. (b) A side view SEM image of the nanorods on 100 nm Pt film. The red region refers to the LSMO spherical seed particles. (c) Atomic Force Microscopy images of $BaTiO_3$-$BiFeO_3$ nanorod arrays grown on Pt-coated Si substrate displaying topography, FE, and FM domains. (d) XRD patterns of $BaTiO_3$-$BiFeO_3$ nanorod arrays. Note: The labels BTO-BFO refer to $BaTiO_3$-$BiFeO_3$. 42

3.3 (a) TRDR of 80-nm thick $BaTiO_3$-$BiFeO_3$ (sample 17), measured at room temperature with the pump wavelength at 400 nm and probe at 800 nm, for different pump powers. The traces are offset for clarity and we refer to TRDR as the change in the transient reflectivity at positive time delay respect to the negative time delay. (b) TRDR on an LSMO (sample 1) film showing no detectable pump-induced response. Note: The labels BTO-BFO refer to $BaTiO_3$-$BiFeO_3$. 46

3.4 (a) The experimental differential reflectivity ($\Delta R/R$) of sample 17 at room temperature at pump power of 0.9 mW. Experimental reflectivity trace scales (red) compared with calculated $N_0(t)$ (black) from the diffusion model, assuming $1/\alpha^2 D = 10$ ps, plotted in the linear (b) and the natural log scale (c). 48

3.5 TRDR for sample 8 at 100 K for different external magnetic fields. The strain pulses arrive at the interface at $\sim$ 20 ps and CP oscillations are not observed in this sample likely due to the response being dominated by carrier relaxation in the region $<$ 20 ps where we would expect to observe them. The inset compares the reflectivity response of sample 8 at room temperature and 100 K, both without applying an external magnetic field (B=0). At 100 K, the carrier-induced change in the refractive index could be responsible for the change in the sign of $\Delta R/R$ [19]. 51

3.6 Transient reflectivity for sample 20 at 100 K for different external magnetic field. We were able to detect CPs, corresponding to an LA phonon frequency of $\sim$ 27 GHz. We observed no magnetic field dependence in the CP oscillations and the reproducibility of the observation at zero field, was confirmed by a post ramp trace, at the end. The feature at 170 ps represents the time for the strain pulses to reach to the interface. The inset shows the dynamics for the first 140 ps at zero magnetic field and the fit to the CP oscillations is to guide the eye. Note: The labels BTO-BFO refer to $BaTiO_3$-$BiFeO_3$ and the arrow shows the time that strain pulses arrive at the interface. 52

3.7 a) The magnetic field dependence of TRDR and CPs in nanorods (sample 23) at 100 K showing nearly periodic modulations at two different frequencies, 33 and 8.1 GHz. This lower frequency mode (8.1 GHz) is very close to the theoretically predicted magnon frequency [20]. Panels (a-c) show the same traces with different x ranges and y offsets. In panel (c) matching the traces at the negative delays and focusing on the first 50 ps, a weak magnetic field dependence was noted. The fits to the CP oscillations are shifted for clarity and are the guides to the eye. Note: The labels BTO-BFO refer to $BaTiO_3$-$BiFeO_3$ and the arrow shows the time that strain pulses arrive at the interface. 55

3.8 TRDR at 700 nm for sample 23, (a) Sensitivity to the external magnetic felds. The measurements were started from -600 mT and ended at +600 mT. The magnitude of TRDR is a factor of 10 larger in this scheme. (b) A smaller subset of the observation in panel (a). (c) TRDR at 1000 nm for sample 23 with smaller amplitude but with a similar sensitivity to external magnetic felds at 700 nm. The signal recovers after increasing the field from zero to 750 mT and come back to zero field. 59

4.1 Here we present an example of x-ray diffraction for the sample 8, displaying the single phase nature of our BTO-BFO films. 66

4.2 (a) The TROIB response of sample 8 with pump-probe of 400/800 nm at 100 K. The inset shows the transient reflectivity at the same temperature and experimental condition. (b) The TROIB detected in sample 20 at 100 K, clearly shows the CLAPs and the sensitivity to the external magnetic fields. 67

4.3 (a) Focusing on the first 140 ps of the TROIB for 3 different magnetic fields we can see both the amplitude of $\Delta\theta$ and the strength of CPs are affected by the field's strength. (b) The evolution of CPs' amplitude by increasing the magnetic field. We expect the magnetic field modifies the bandgap and alter the absorption strength of the pump pulses reducing the amplitude of the CPs. (c) Focusing on the first 20 ps one can see the amplitude of $\Delta\theta$ reduces by increasing the external magnetic field. 68

4.4 (a) TRMOKE at 100 K with the pump pulses at 400 nm being circularly polarized. The over all feature of the CP dynamics including the frequency and the arrival time at the interface remained mainly similar to the OIB measurements and by increasing magnetic field both the amplitude of the MOKE signal as well as the CPs' strength decreased. The traces are shifted for clarity. The inset compares two traces for two different circular polarizations and are shifted slightly for clarity. As shown in this inset, we did not observe any differences when the pump circular polarization was switched between left and right. 70

4.5 SHG in (a) sample 8 and (b) sample 20 intensity distribution of incident wavelength with 150 mW incident power at room temperature with 120 s exposure time. 74

4.6 (a) Schematic diagram of the SHG incident polarization setup. (b) Testing the analyzer sensitivity to polarization with a laser at 488 nm. We used this wavelength as the SHG in the nanorods are close to this range.The incident polarization dependence of SHG in the sample 8 at 980 nm using an analyzer on the emission path. (c),(d) analyzer configuration for S and P respectively. 75

5.1 Cross-sectional FESEM image (a) and surface morphology (b) of PZT nanorod arrays. While each nanorod is a single crystal, the ensemble is composed of nanorods with random orientations. The array has a close-packed structure and is nearly homogeneous in diameter and height. (c) Polarization vs electric field (P-E) loop for the nanorod arrays displaying ferroelectric behavior. . . 82

5.2 Piezoresponse force microscopy (PFM) images of PZT nanorod arrays with (a) unpoled, (b) poled down, (c) and poled up states. The images present both the topology (top panels) and phase signals indicating the polarization directions (lower panels) of the nanorods. The samples are different pieces from the same wafer. (d) The amplitude of SHG response for the unpoled (S1), poled up (S2), and poled down (S3) PZT nanorod arrays. (e) Power dependence of the samples show the SHG intensity is proportional to the square of the intensity of the incident light. 84

5.3 (a) Here we present the amplitude of the SHG for sample (S2) for when it was poled and then after it was heated to 400 ^0C. The measurements are under the exact same conditions. The SHG amplitude of the unpoled state of sample S2 is comparable to S1 (unpoled), in Fig. 5.2(d). (b) Topology from PFM measurements and (c) the phase of Sample S2, after it was heated to 400 ^0C for about 10 minutes, confirming the sample is unpoled after being heated. 86

5.4 (a) Testing the analyzer sensitivity to polarization with a laser at 488 nm. We used this wavelength as the SHG in the nanorods are close to this range. (b) The incident polarization dependence of SHG in the unpoled nanorod at 980 nm using an analyzer, with an analyzer set at S polarization on the emission path, similar to the measurements in panel (a). 88

5.5 (a-d) Here we present the examples of the polarization dependence at 980 nm and 1000 nm for the samples S1 and S3. We observe some polarization dependence in the SHG, for different configurations of the incident and analyzer states. 90

5.6 (a) Room temperature TRDR of PZT nanorods of the unpoled sample (S1). We observed carrier dynamics where both the pump/probe wavelengths were tuned in NIR. We should note, except at 800 nm, we observed an increase in the transient reflectivity, with the largest increase of ($\Delta R/R$) at 730 nm. The inset shows the topology and the phase of the nanorods using SEM. (b) Similar measurements on the LSMO seed show a much smaller response to the NIR optical excitations with no sensitivity to the variations in the excitation wavelengths. The inset displays the SEM image of the LSMO seeds to compare with the PZT nanorods' topology. 93

5.7 The transient reflectivity of the nanorods in a two color scheme where the pump tuned at 400 nm is close to the expected bandgap of PZT. The inset shows the pump-probe measurements on the LSMO seeds under the exact experimental condition. 95

5.8 SHG response for PZT thin film structures. These measurements were taken with 120 second exposure time. 97

5.9 Room temperature TRDR of PZT thin film structure. Similar to nanorod structures in thin film structures, we observe carrier dynamics where the pump-probe wavelengths are tuned at 730 nm (∼1.70 ev) where two photon absorption were involved in the photoexcitation. The inset shows the pump-probe measurements on the LSMO substrate with same experimental condition. 98

6.1 Schematic illustration of procedure for fabrication of coated perovskites through the self-assembly process and TRDR spectra of perovskite films. (a) The complexation between PMMA polymer chain and 2D layered perovskite intermediates. (b) Upon evaporation of solvent, the layered perovskite will be self-assembled, leaving PMMA anchored at the boundary of perovskite grains (c) TRDR of $MAPbI_3$ film (sample 1), $MAPbI_3$+PMMA film (sample 1), and $MAPbI_3$-PMMA film (sample 1) as a function of time delay, represents the relaxations of the photo-induced carriers in three samples. An example of a double exponential fit to extract τ_1 and τ_2 is shown for sample 2 and it is shifted for clarity. The exponential fits identify τ_2 to be ∼260 ps for sample 1 and 3 and much longer, ∼590 ps, for sample 2. We observed CP in all three samples in the panel (c) but increasing the pump power from 0.3 mW to 0.6 mW made the amplitude larger. (d) Close up of the CP oscillations from the perovskite film (sample 1), in which the fit is shifted for clarity and is corresponding to a phonon frequency of 14.6 GHz. 103

6.2 Time resolved measurements at 850 nm pump-probe excitations for $InAs_xP_{(1-x)}$ with (a) $x = 0.07$ and (b) $x = 0.34$. In both samples, we observed bumps at 500 ps. Sound velocity in InAs 3.83×10^3 m/s and for InP is $\sim 4.58 \times 10^3$ m/s. Using these values and the thickness of InAsP layer (1.2 μ m), we can conclude the pulses were reflected back at the interface to observe the bumps at 500 ps. 109

6.3 Time resolved differential reflectivity at 950 nm with 0 mT and 800 mT magnetic field. 110

6.4 (a) Schematic representation of the experimental configuration for the TRMOKE as a function of the field. (b) TRMOKE response of $InAs_{0.34}P_{0.66}$ for two circular polarizations. 111

6.5 TRMOKE at different magnetic fields show the clear signature of precession above 500 mT followed by fast decay in 150 ps. These measurements were taken with 950 nm, 128 mW pump beam with -σ polarization. 112

6.6 High field CR was used to measure the effective mass for the two InAsP alloys. The data was taken sweeping the field up and down. 113

6.7 Schematic representation of the PL setup that was used to probe SHG and up-conversion luminescence of the plasmonic structures. To probe spectral shape dependence on the emission polarization a polarizer (analyzer) and an iris was introduced to the emission path (a). Note: GLP is Glan Laser polarizer. 115

6.8 SHG and up-conversion luminescence spectrum for 1000, 1020, and 1040 nm, 128 mW, and P polarized incident beam. The inset shows the material structure where the TiO_2 thickness for this sample is 150 nm (Three samples with variable TiO_2 thickness (20, 60, and 130 nm) were studied in this project). . 116

B.1 Schematic diagram of the TRDR setup 153

B.2 Schematic diagram of the TRMOKE Setup 155

B.3 Schematic diagram of the SHG setup 156

B.4 Transmission profile of the two 900 shortpass filters (a) FES0900 (b) FESH0900, provided by Thorlabs, Inc. 158

B.5 Observed fluorescence from the Ti:sapphire oscillator on different reference samples (a) Cu tape (b) Frosted glass surfaces. Here the observed oscillations in (b) are resulted from the transmission profile of the 900 Shortpass filter (Fig. B.4), which was before the spectrometer. 159

List of Tables

3.1 Structural details of the samples studied in this work. (In our preliminary investigations, we have probed the following structures and the published work presents the structures with the best dynamical responses.) Note: *In the case of the nanorods, the LSMO layer refers to nano-sphere arrays. 38

4.1 The samples studied in this work. The thicknesses refer to the BTO-BFO layers and LSMO layers. 65

Chapter 1

Introduction

The remarkable progress in the field of information technology has led to a greater need for higher switching rates, higher capacity, and faster processing time. As the conventional semiconductor technologies are reaching their limits, there is an increased interest in implementing optoelectronic, spintronics [13, 14, 15, 21], and all-optical technologies by using new classes of materials with multifunctionality. The ability to control and manipulate the electronic, vibrational, and spin degrees of freedom in nanostructured materials and/or heterostructures promises to be revolutionary in the fields of quantum information and sensing [10, 22, 23]. This, together with control at the level from lattice structure to electron spin states, can give rise to improved or even qualitatively new and robust materials properties.

With the advancements of pulsed lasers, ultrafast nonlinear optical spectroscopy has progressed into an essential spectroscopic technique that provides vital information on many fundamental physics phenomena as well as device aspects of functional materials. This includes not only band structure, underlying symmetries, and defects, but also non-linear non-equilibrium properties such as carrier and spin dynamics, scattering, coherent phonons, magnons, and transport properties. Time resolved pump-probe spectroscopy is an excellent tool to probe fast microscopic processes and their temporal behavior. Ultrafast optical spectroscopy can provide insight into fundamental microscopic interactions, dynamics and the coupling of several degrees of freedom. Time resolved pump-probe spectroscopy allows us to understand the relaxation dynamics of photoexcited carriers; where after photoexcita-

tion, the non-equilibrium population of electrons and holes can relax by several scattering mechanisms such as carrier-carrier, carrier-phonon, and carrier-impurity. Using femtosecond pulses, carriers can be excited within a narrow energy band of states, and as time progresses, the carrier-carrier interaction results in thermalization of the carrier distribution. On a longer time scale electron-phonon interactions bring the system to a quasi-equilibrium. On even a longer time scale, recombination of the carriers across the gap activates a true equilibrium [24, 25].

The ability to generate and manipulate the time resolved, phononic, and magnonic degrees of freedom in materials with external optical, electric, and magnetic fields promises to usher in a new era of revolutionary advances in science and in device applications [2]. To probe coherent states in several less explored materials system, in this study several ultrafast techniques including Time Resolved Differential Reflection (TRDR)/Transmission (TRDT) were employed. While TRDR and TRDT are often used to study carrier dynamics of materials, these techniques can also be employed to study coherent phonons and magnons [2]. Furthermore, we employed Time Resolved Optically Induced Birefringence (TROIB) and Time Resolved Magneto-Optic Kerr Effect (TRMOKE) which provided complementary information on several materials systems studied here.

Another valuable approach in this dissertation was taking advantages of Second Harmonic Generation (SHG) spectroscopy. Since the discovery of SHG in 1961 by Franken *et.al* [26], this technique considers as one of the most popular nonlinear optical spectroscopy tool that has been used for many applications. This includes fundamental research of materials such as symmetric and non-symmetric structures [27, 28, 29, 30, 31, 32], high-resolution imaging [33, 34] as well as device-based applications such as ultrafast pulse laser generation [35], ultrafast pulse measurement, optical parametric generation [36], optical parametric amplification [37], optical switches, modulators [38, 39], and sensors [40]. Towards these

advancements, employing low dimensional material systems have attracted many research activities, aiming for more tunability, miniaturization, and integration on chips. In this study, to the best of our knowledge I am reporting for the first time the SHG on $Pb_{0.52}Zr_{0.48}TiO_3$ nanorod arrays. This experimental study can provide valuable information for employing these nanostructures in nonlinear photonic applications.

Although my research activities contributed to several directions, in the following sections I will elaborate two major projects: 1) ultrafast coherent phonon dynamics and nonlinear light-matter interactions in multiferroic $BaTiO_3$-$BiFeO_3$ (BTO-BFO), and 2) ultrafast dynamics and second harmonic generation in ferroelectric $Pb[Zr_xTi_{1-x}]O_3$ (PZT) materials systems. The information provided in this introduction chapter will help to elaborate the findings in other chapters.

1.1 Ultrafast Coherent Phonon Dynamics and Nonlinear Light-Matter Interactions in Multiferroic $BaTiO_3$-$BiFeO_3$ (BTO-BFO) Material Systems:

1.1.1 Motivation

Impacts of Coherent Phonons:

The ultrafast, femtosecond photoexcitation of solids can trigger oscillations in the solid known as coherent phonons. Typically, these oscillations are in the 5-20 THz region and result from the coherent excitation of optical phonons [41, 42, 43, 44, 45]. If the absorption is not uniform, such as in layered structures or for short absorption depths, one can additionally

trigger coherent acoustic phonons (CAP) which propagate as strain pulses into the sample [2, 46, 47, 48]. Usually, coherent phonons are used to provide detailed spectroscopy information and characterize surfaces and buried interfaces. However, the ability to generate strain via ultrafast optics offers the intriguing possibility of dynamically manipulating the strain in a given sample with ultrashort optical pulses and opens the possibility of creating a new class of devices, where the strain is manipulated in time to control the properties and operation of the device. Experimental studies of coherent phonons and the ability to control and manipulate them in solids have gained increased interest due to the wide variety of applications of coherent phonons and their interactions (phonon-phonon, electron-phonon, etc.). These studies have been conducted in several different materials such as semiconductors [49, 50, 51], semiconductor super-lattices [52, 53], quantum well [47, 54, 55], etc [56]. The ability to control the generation and detection of CAPs can lead to a wide range of novel applications in heat management [57, 58] and phonon-lasing [59, 60, 61]. Furthermore, the photonic-like behavior of phonons opens up the possibilities to develop nano-mechanical cooling via optomechanics [62, 63, 64, 65], trapping of phonons in artificial phononic bandgap cavities [62, 66], and indirect qubit-phonon coupling [67, 68].

The sensitivity of coherent phonon oscillations to the internal field (electric, magnetic, strain) makes way for potential applications in high sensitivity quantum detectors as well as in quantum-sensing [10]. Apart from that, in recent discoveries, it was shown that spin-phonon coupling can be used to manipulate spins. This fact has been reported in several different crystalline structures [69, 70, 71, 72] which includes multiferroics [47]. It has recently been demonstrated that dynamical strains in Surface Acoustic Wave (SAW) devices can interact with spins in silicon carbide [73]. Moreover, recent publications on a hybrid state of coherent phonon and magnon [11, 74] have increased the interest in the field for fundamental studies of coherent phonons in strongly correlated systems. In both Ref.[11] and Ref.[74], the magnetic

field-dependent magnon mode is tuned into resonance with the magnetic field-independent phonon modes by an external magnetic field and they have observed magnon-phonon hybridization (magnon–phonon quasiparticle) at the resonance points. In both of these material structures the coherent phonon- magnon hybridization is demonstrated using the generation of SAW. However, ultrafast optical generation of the strain by employing CAP offers a potentially better means of generating the dynamic strain that can bypass the need to fabricate a SAW device and allow for higher frequencies and faster manipulation [10].

Probing Coherent States in Multiferroic BTO-BFO:

Recently, it has been demonstrated that the dynamics in multiferroics can be governed by the excitation of electromagnons where, unlike the magnetic excitations which interact with the magnetic field, the electromagnons are excited by the electric field of the electromagnetic wave. Rovillain *et al.* [75] demonstrated that the spin wave frequency (>600 GHz) in $BiFeO_3$ can be tuned at room temperature by over 30%, in a nonvolatile fashion using an electrical field. Theoretical calculations suggested that this effect can originate from a linear ME effect related to spin-orbit coupling induced by the applied electric field. Here we employ ultrafast optical spectroscopy which can provide insights into fundamental microscopic interactions, dynamics and the coupling of several degrees of freedom. Multiferroic BTO-BFO [2] systems have gained recent interest due to the simultaneous coexistence of electric and magnetic orders. BTO-BFO is a room temperature multiferroic with ferroelectric and antiferromagnetic order and displays good coupling between the magnetic, piezoelectric and elastic properties. This fact provides opportunities to investigate not only the transient coupling between the phonon, photons, carriers, and the lattice, but also how to tailor and control the coherent states.

In ferromagnetic based memories, the speed of operation is constrained to the GHz range

because the spin dynamics are dominated by magnetic anisotropy. On the other hand, spin dynamics in antiferromagnets (AFs) are dictated by interatomic exchange interaction energies which are several orders of magnitudes larger than magnetic anisotropy energies. This provides the potential for ultrafast processes in sub-THz to THz range. Recently, it has been demonstrated theoretically that a structure consisting of a metallic layer with a strong spin-orbit interaction (such as Pt) and a layer of a bi-axial antiferromagnetic dielectric (such as NiO) can be a platform for a tunable room temperature THz-frequency signal generator [76, 77]. In general AF magnons can also offer a chiral degree of freedom, which can provide new directions for processing information. One of the advantages of magnon spin current is that no conduction electrons are required, so that information can be propagated even in insulating materials [76, 77, 78, 79]. Furthermore, magnons are based on collective dynamics of magnetic moments; therefore, magnon spin current can have a large attenuation length (∼mm), especially in magnetic media with low damping [78]. One should note here that maximum attenuation length for electron-mediated pure spin current in a conductor is limited by the electron mean free path, which can be of the order of a few microns. Furthermore, magnon spin currents can behave as coherent waves even above room temperature, to achieve wave-based computing. The AF character of BTO-BFO also makes it an excellent candidate for ultrafast processes in the sub-THz to THz range. [76]

In this project, we report on coherent states of both BTO-BFO films and BTO-BFO nanorod arrays and the tunability of these states as a function of magnetic field. Probing the effect of the structural composition and the dimensionality can provide important insights in generation and controlling CAPs; thus, we investigated several different configurations of BTO-BFO films and nanorod structures. This dissertation includes studies on BTO-BFO/LSMO/STO (Here, LSMO is Lanthanum Strontium Manganite and STO is Strontium Titanate) hetero-epitaxial thin-film structures with different layer thicknesses and BTO-

BFO/Pt/Si nanorod arrays. Here, we have carried out TRDR, TRMOKE, TROIB, and SHG measurements, to study the coherent states, ultrafast dynamics, and nonlinear optical properties of these less explored material structures.

1.1.2 Background:

A Brief Background on Multiferroic BTO-BFO:

Ferroic materials fall under the subgroup of functional materials and have a large contribution to developing modern-day technologies. The most well-known three categories under ferroic materials are ferroelectric, ferromagnetic, and ferroelastic that possess long-range electric or magnetic or elastic orders respectively. Thus, the main characteristic of these materials is the non-zero value of their respective order parameters, polarization, magnetization, and self-strain below a critical temperature. Spontaneous symmetry breaking in these materials are important to understand the macroscopic properties of their structures. From the crystal symmetry point-of-view, symmetry breaking in a crystal results in diverse ferroic orders. The magnetization (axial vector) and polarization (polar vector) have different symmetry properties [80]. Ferromagnets exhibit a spontaneous magnetization, where the origin is from the orbital spin of the electron. The current associated with these unpaired spins of the electrons break the time-reversal symmetry [80]. On the other hand, spontaneous polarization of ferroelectrics arises from spatial-inversion symmetry breaking [80]. Moreover, this spontaneous symmetry breaking result in domain structures. One important feature of "functional" materials is the ability to change their properties with respect to the external fields in a controlled manner [81].

The inversion symmetry breaking in a non-centrosymmetric crystallographic structure results in a directional vector (magnetization or polarization or strain) that can be coupled

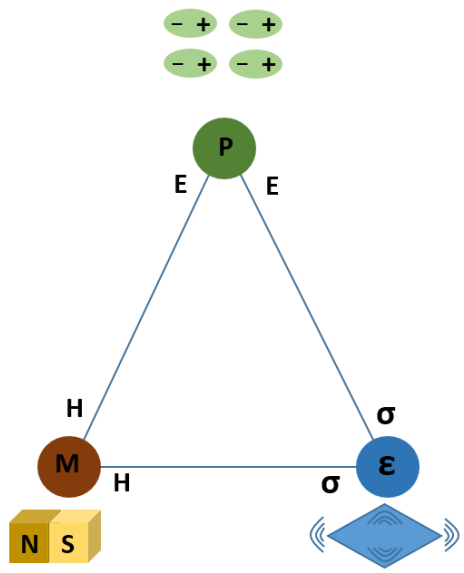

Figure 1.1: Multiferroics. The electric polarization (P), magnetization (M) and strain (ϵ) is a function of, the electric field (E), magnetic field (H) and stress (σ), respectively. In multiferroics, multiple ferroic orders coexist in a single phase, giving rise to coupling order parameters such as magnetoelectric coupling, where E can control the M and vice versa [16].

to an external field. For example, in ferroelectric materials the polarization direction in each domain structure is different, minimizing electrostatic and elastic energy. Domain wall movement and switching as a response to an external electric field results in a hysteresis behavior [82]. Similarly, all ferroic orders follow a hysteresis when coupled with the respective external fields (electric or magnetic or strain). A class of materials that consist of multiple ferroic properties are multiferroics. Multiferroicity has opened the door to "multi-functional" materials. According to H. Schmid's definition (1994) [83], multiferroics are materials that showcase two or more primary ferroic orders in a single phase simultaneously. In the present day, the term multiferroic has broadened, including not just ferroic properties but slight variations of properties such as Ferro-, Ferri- or anti-Ferro- order. The majority of devices today are based on electric and magnetic properties of materials. Therefore, multiferroics have a broad range of applications such as new-generation of high-density high-speed data storage [84], sensing and actuating devices [85], tunneling magnetoresistance [86, 87].

Furthermore, when magnetic and electric orders coexist in a single-phase, coupling between

them gives rise to the magnetoelectric (ME) coupling. Through ME coupling one can switch the electric polarization upon applying a magnetic field and vice versa. Similar to ferroic materials, multiferroic properties are also associated with crystal structural symmetries. As discussed earlier local dipole moment has the time-inversion symmetry but breaks the spatial-inversion symmetry, whereas, the magnetic moment breaks the time-inversion symmetry. Having these two properties in a single-phase, multiferroics possess neither symmetry, resulting in ME coupling [80]. Moreover, this can be expressed using the Landau theory. The free energy of a magnetoelectric system with an applied magnetic (H) and electric(E) field, can be expressed as [80]:

$$-F(E,H) = \frac{1}{2}\epsilon_0\epsilon_{ij}E_iE_j + \frac{1}{2}\mu_0\mu_{ij}H_iH_j + \alpha_{ij}E_iH_j + ..., \tag{1.1}$$

where ϵ_0 is the permittivity of free space and μ_0 is the permeability of free space. ϵ_{ij} is the relative permittivity and μ_{ij} is the relative permeability of the medium. The first two terms of the above equation represent the response to an external electric or a magnetic field, respectively. α_{ij} is the linear magnetoelectric coupling constant (second-rank ME-susceptibility tensor) which gives rise to the linear coupling between electric and magnetic components.

In Eq. (1.1), higher-order terms are weaker compared to the linear magnetoelectric coupling term. Thus, considering the sum of the first three terms to be greater than zero [80]:

$$\alpha_{ij}^2 \leq \epsilon_0\mu_0\epsilon_{ij}\mu_{ij}, \tag{1.2}$$

Inherently ferroelectric materials have higher ϵ_{ij}, whereas most naturally occurring single-phase multiferroic materials, have small α_{ij}. ME coupling in a multiferroic material can be

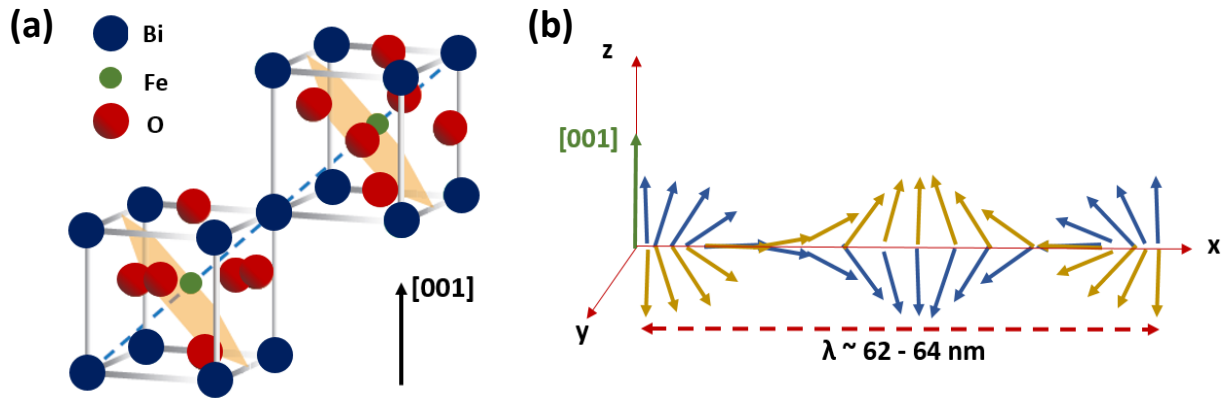

Figure 1.2: (a) Crystal structure of $BiFeO_3$ (Perovskite structure) [17]. (b) Schematic representation of inherent spiral spin structures in $BiFeO_3$ [18].

enhanced by improving the permittivity and permeability (Eq.1.2) of the material. Thus, one commonly used method to enhance the magnetoelectric coupling in single-phase multiferroic, is to add a given material with a large permittivity or permeability. Hence, ferroelectrics and ferromagnetics are key candidates to develop composite material structures, to enhance room temperature magnetoelectric effect in single-phase multiferroics.

The origin of magnetism in a material is from the partially filled d or f orbitals, whereas ferroelectric materials have empty d orbitals. Moreover, most ferromagnets tend to exhibit metallic properties due to their high-density states, whereas, ferroelectrics are insulators. Due to the competition between these ferroic orders, only a few ME multiferroics exist in nature. $BiFeO_3$ (BFO) is one of the most extensively studied room temperature single-phase multiferroic. BFO has gained much attention due to its room temperature ferroelectric and antiferromagnetic properties with high Curie ($T_C \approx 1103$ K) and Neel temperatures ($T_N \approx 643$ K) [8]. At room temperature, bulk BFO has a rhombohedral distorted perovskite structure with the R3c crystal symmetry ($a = b = c = 5.63$ Å, $\alpha = \beta = \gamma = 59.4^0$ [88]. In BFO the polarization (ferroelectricity) results from the anisotropic distribution of unbounded valence electrons, $6s^2$ lone pair of the Bi^{3+} ion. In contrast, the spin of the unpaired electrons

in the Fe^{3+} cation (d^5 electronic configuration) gives rise to the magnetic order.

BFO is a G-type antiferromagnetic, where intra-plane and inter-plane antiferromagnetic coupling exhibit weak magnetism at room temperature. Below Neel temperature, all the spins are aligned ferromagnetically along the [111] plane and antiferromagnetically with the adjacent planes. But these spins are not exactly collinear, instead, the antiparallel spin sublattices are canted as a result of the superexchange interaction [8, 80]. This canted antiferromagnetic order leads to a spiral spin structure with a period length of 62-64 nm [89], which results in weak ferromagnetism via the Dzyaloshinskii-Moriya (DM) interaction [90]. DM interaction is the antisymmetric exchange contribution to the total magnetic exchange interaction, which results in a weak magnetization in an AF at room temperature. This spiral spin structure can be suppressed, to release the inherent magnetization by applying a high external magnetic field or through spatial confinements. It has been reported in previous studies that low-dimensional structures have improved magnetic character leading to a higher ME coupling [91]. Furthermore, the linear magnetoelectric effect could also be improved by applying large magnetic fields of 20 T [92]. It was also reported that chemical substitutions and strain engineering are effective methods to improve magnetoelectric coupling in BFO [91]. Another drawback of BFO is its large leakage current, associated with the oxidation of Fe ions (Fe^{+3} and Fe^{+2}) thus, increasing the conductivity via oxygen vacancies [88].

In this study, we used a solid-state solution of $BaTiO_3$-$BiFeO_3$ (BTO-BFO) which has enhanced ferroelectric and ferromagnetic order compared to BFO [2, 93]. Here, by adding another perovskite material with a higher dielectric constant, the ferroelectric characteristics in the admixture can be improved, resulting in higher ME coupling. Moreover, with the addition of BTO, the resulting increase in the radius of the A-site ion can lead to the improved magnetic character via suppression of the spin cycloid [93]. The composition of the solid solution, specifically the mole fraction of BFO, is an important parameter to achieve the opti-

mum magnetoelectric order in BTO-BFO. The solid solution with the composition of (0.285) BTO and (0.725) BFO shows the maximum ME coupling coefficient of 0.87 mV/cm.Oe and also high piezoelectric properties ($g_{33} = 18.5 \times 10$ mV.m/N and $d_{33} = 124$ pC/N) [93]. Large ME coupling enables optical rectification in multiferroics, which opens up new avenues for promising new nonlinear ME effects in nanostructured multiferroic materials.

Coherent Phonons:

The ultrafast, femtosecond photoexcitation of solids can trigger oscillations (Brillouin oscillations) in time resolved optical properties such as the differential reflectivity or transmission, known as coherent phonons (CPs). These phonons are different from the phonons that are emitted at random, when the photoexcited hot electrons and holes, relax back to the conduction and valence band edges, which are the incoherent phonons. Instead, coherent phonons are a superposition of phonon number eigenstates $|n>$ with a distinct phase relationship much like the familiar coherent states of the harmonic oscillator which are minimum uncertainty Gaussian wavepackets that oscillate in the harmonic potential without broadening. However, if the absorption is not uniform, such as in layered structures or for short absorption depths, one can additionally trigger coherent acoustic phonons (CAP) which propagate as strain pulses into the sample which are in the GHz range. In a pump-probe scheme the probe light is reflected at the surface and the other regions of the sample, leading to the detection of oscillation similar to the Fabry-Perot interference. Let us review the differences between incoherent and coherent phonons closer.

When a photoexcited carrier system reaches its thermal equilibrium, the excess energy is transferred to the lattice via incoherent phonons. This increases the temperature of the lattice causing thermal expansion, which creates thermoelastic stress. Assuming the absorption length of the incident light in the material is smaller than the film thickness the isotropic

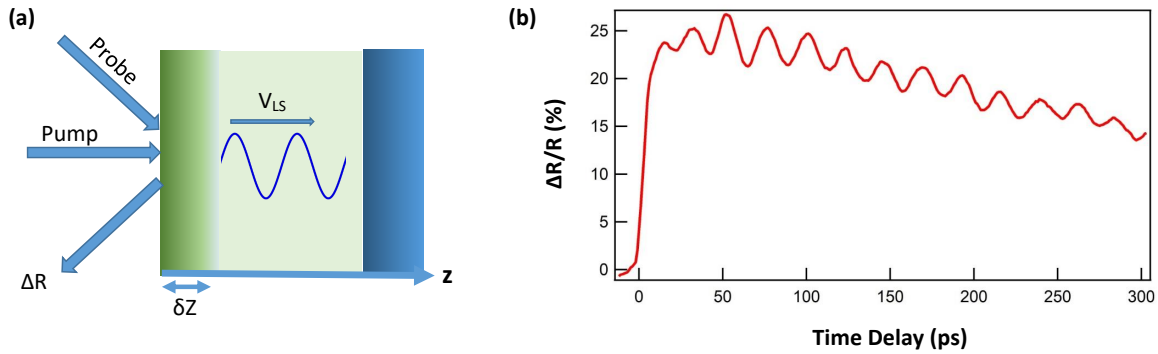

Figure 1.3: This schematic represents the coherent phonon generation and detection via pump-probe technique. The pump pulse generates an acoustic pulse at the surface that can propagate into the material at the longitudinal speed of sound in the material (V_{LS})and δz is the strain layer where the absorbed pump energy is deposited. The probe light is reflected at the surface and other regions of the sample, leading to a detection scheme similar to the Fabry-Perot interference.(b) The resultant oscillatory pattern observed in a transient reflectivity curve from a propagating coherent phonon. Adopted from data provided by Brenden Magill on GaMnAs [10].

thermal stress can be expressed as highlighted by Thomsen et al. [94]:

$$\sigma(z) = -3B\beta\Delta T(z), \tag{1.3}$$

where B is the bulk modulus and β is the linear expansion coefficient, $\Delta T(z)$ is the temperature rise that is dependent on the pump energy density and the heat capacity of the medium. This thermoelastic stress generates CAPs. For metals, the main source of CAP generation is the thermoelastic effect which results from the thermal stress generated by the shorter absorption length. In the case of anisotropic thermoelastic stress, a shear strain can generate via the non-uniform longitudinal strain. This shear strain can result in transverse acoustic waves.

Another source of coherent phonons is the deformation potential. Upon photoexcitation, the

electron and phonon distribution functions change, resulting in the change in the interatomic forces generating additional stress in the system, where the change in electronic distribution function generate a deformation potential in the system. The total generated stress can be expressed as [94]:

$$\sigma_{ij} = \sum_k \delta n_e(k) \frac{dE_k}{d\eta_{ij}} + \sum_k \delta n_p(k) \hbar \frac{d\omega_k}{d\eta_{ij}}. \tag{1.4}$$

Here, $\frac{dE_k}{d\eta_{ij}}$ is the deformation potential. $\delta n_e(k)$ and $\delta n_p(k)$ are the change in the electron and phonon distribution functions respectively, where E_k is the energy of an electron and ω_k is the frequency of a phonon with wave vector k. When the system (both electron and phonon) is in a thermal equilibrium, the more prominent source of stress is the thermoelastic stress (*i.e* Eq. 1.4 reduces to Eq. 1.3) [94].

In semiconductors, photogenerated electrona and holes as well as the emitted phonons during the relaxation process, can contribute to the total strain generated in the system. Assuming the material is elastically isotropic and the phonons are at a thermal equilibrium, this can be analytically expressed as [94]:

$$\sigma^e_{ij} = -B \frac{dE_g}{dP} \delta_{ij} \delta n_e - \frac{3B\beta}{C} (E - E_g) \delta_{ij} \delta n_e, \tag{1.5}$$

where E_g is the bandgap, P is the pressure, $(E - E_g)$ is the energy of phonons, and δn_e is the total number of electrons.

Apart from the strain generation mechanisms discussed above, the inverse piezoelectric effect induces lattice strain that can be an additional source for the generation of CAP [51]. As a result of photoexcitation, the photoexcited carriers modulate the internal electric field of the material resulting in an inverse piezoelectric effect. The CAP generated at the surface

travels into the structure at the speed of longitudinal sound of the material and bounce back and forth between the interfaces or propagates into the substrate. The reflectivity of the acoustic pulse at an interface depends on the acoustic impedance mismatch between the two layers. The propagating CAP is classically modeled by traveling strain pulses moving away from the surface with longitudinal acoustic velocity of the material [94].

In the pump-probe scheme, the generated CAP is observed via the change in transient reflectivity (transmission) of the probe beam (Fig. 1.3(a)). The propagating CAP results in localized changes in the complex dielectric function of the material and also through the surface interface displacement caused by the acoustic pulse generation. Both the photoelastic effect and the interferometric effect contribute to the transient optical reflectivity. The period of oscillation of the acoustic pulse can be observed by choosing a probe beam that is transparent or has a longer penetration depth in the material under investigation. The local refractive index modulates owing to the photoelastic effect as the strain pulse propagates through the medium. This results in a change in the optical path of the probe beam, causing a phase shift in the scattered probe beam. The interference of this scattered probe beam by the propagating strain pulse, and the probe beam reflected at the surface and interfaces, results in a periodic modulation in the measured transient reflectivity (Fig. 1.3(b)). The detected transient reflectivity is:

$$\frac{\Delta R}{R} = 2Re\frac{\Delta r}{r_0}, \tag{1.6}$$

Changes in the refractive index reflects on to the observed differential reflectivity. Thus, pump induced changes to the refractive index for a uniform material is given by [95]:

$$\frac{\Delta R}{R} = 2Re\int_0^\infty e^{(i2kz)}\frac{d}{dz}\delta n(z,t)dz, \tag{1.7}$$

where is $k = nk_0$ and $\delta n(z,t)$ is the change in the complex index of refraction resulted from the pump induced change in the dielectric constant ϵ:

$$2n\delta n(z,t) = \delta\epsilon = -a_{cv}\frac{d\epsilon}{dE}\eta. \tag{1.8}$$

Here, η is the propagating strain, a_{cv} is the deformation potential, and $d\epsilon/dE$ is the Seraphin coefficients that reflects on the amplitude of the oscillations for different probe energies [95]. In the linear regime, the strain pulse propagates undistorted through the media with a velocity v_s away from the surface. Thus [95],

$$\frac{\Delta R}{R} \propto 2Re\left\{\frac{d\epsilon}{dE}e^{(i2kv_st)}\int_0^\infty e^{(i2ku)}\frac{\delta}{\delta u}\delta\eta_0(u)du\right\}, \tag{1.9}$$

where $u = z - vt$. The frequency of these oscillations in $\Delta R/R$ is proportional to the frequency of the propagating CAP thus, the period T given by $T = \lambda_0/(2nv_s)$ where v_s depends on material properties, stiffness and the density of the medium. More detailed discussion on these CAPs observed in BTO-BFO is given in Chapter 3.

1.2 Nonlinear Spectroscopy in Ferroelectric $PbZr_{1-x}Ti_xO_3$ (PZT) Material Systems

1.2.1 Second Harmonic Generation:

Investigations in nonlinear light-matter interaction plays a particular role in the development of optoelectronics. Laser (pulse generation, frequency conversion) [35, 96, 97, 98], optical parametric generation and amplification [36, 37, 97, 99], actuators and modulators [38, 39,

100, 101], and optical switches [102] are a few of the most widely used optoelectronics applications. Since most of the present-day applications are based on bulk crystals, there has been an increased interest in developing nano-structured material systems with advanced nonlinear properties which will facilitate device miniaturization attempts and can be easily integrated with modern devices. When implementing novel materials in these devices higher light conversion efficiencies and fabrication strategies for large scale production is needed. A number of studies have been conducted to obtain an efficient light conversion in nonlinear materials. The common mechanisms to achieve high efficiency is "phase-matching", which is further discussed in the section 1.2.1. On the other hand, PZT nanostructures are a well-established functional material with excellent ferroelectric, piezoelectric, and nonlinear optical properties. Not only there exist efficient strategies for bulk production of PZTs for industrial applications, there also exist well developed means to fabricate low dimensional PZT structures with enhanced properties [103, 104, 105, 106]. These PZT nanorods can be easily grown on silicon thus making it compatible to incorporate with already existing devices.

Moreover, SHG spectroscopy is also widely used to investigate the electronic structure and the underlying symmetries in materials. The breaking of both space-inversion symmetry and the time-inversion symmetry gives rise to SHG. Thus, SHG spectroscopy has been employed to study the underlying crystal symmetries in non-centrosymmetric materials and also to study magnetic domain structure [27, 28, 29, 30, 31, 32]. The most commonly used nonlinear optical technique is the SHG spectroscopy. Here, we are mainly focusing on the SHG in these PZT nanostructures. We have studied and employed SHG on our material structures and have performed power dependence, wavelength dependence and polarization dependence measurements on PZT nanostructures. Our main motivation behind this study was to investigate the relaxation dynamics of these newly developed nanostructures and to

study nonlinear light-matter interactions of these structures via SHG.

Impacts of Ferroelectric PZT:

Ferroelectric materials have inherent coupling between the electromechanical parameter and polarization switching behavior that opens up a wide variety of applications. In this class of materials, spontaneous polarization below the Curie temperature, which originates through space inversion symmetry breaking, can occur. In a ferroelectric material, each domain has an inherent polarization direction and the electrostatic energy is minimized through the alignment of dipoles. The domain switching and domain wall movement under an external electric field results in a hysteresis loop (Polarization (P)-Electric field (E) loop). An important feature of ferroelectrics is that most of the ferroelectrics are in the category of dielectrics, piezoelectrics, and pyroelectrics (Fig. 1.4). The piezoelectric property of a material can be used to convert mechanical energy to electrical energy and vice versa. These materials can be electrically "poled", via external electric fields to utilize the inherent piezoelectric property in commercial applications. During the poling treatment via an applied external electric field the material achieves a preferred organization of ferroelectric domains. However, this poling would only exist below the material's Curie temperature.

One of the most popular ferroelectric materials being developed since their introduction is the lead zirconate titanate (PZT). PZT is a perovskite with an excellent ferroelectric and a piezoelectric character and a high Curie temperature. Moreover, PZT possesses a wide range of dielectric constant and also can be easily poled. PZT exhibits an excellent piezoelectric response near the morphotropic phase boundary (MPB) where the crystal structure transitions from tetragonal to the rhombohedral phase, thus changing the polarization axis from [001] to [111]. Moreover, instability of the structure due to the presence of MPB results in a high piezoelectric property in PZT [107]. It is widely used to develop sensors (pressure, in-

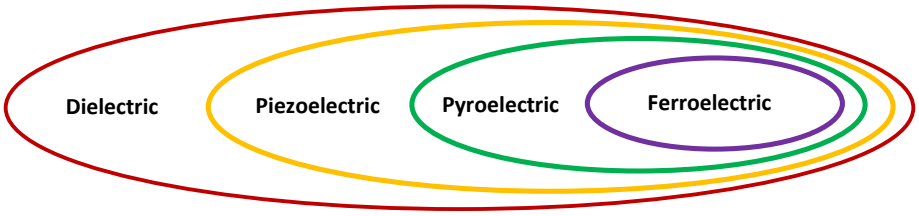

Figure 1.4: Hierarchy of functional materials, which represent the relation between ferroelectric, pyroelectric, piezoelectric, and dielectric materials.

frared, speed) and actuators [108], which are important components when developing smart devices. The ferroelectric polarization switching property is used in non-volatile memory applications like ferroelectric random-access memory (FeRAM) [109].

In this study, we investigated 1D ferroelectric $PbZr_{0.52}Ti_{0.48}O_3$ (PZT) nanostructures. Scaling down materials from bulk to nanostructure is essential for device miniaturization, as well as to exploit and enhance material properties. These close-packed single-crystalline ferroelectric nanorod arrays were grown on Pt coated commercial silicon (Si) which would be compatible with commercial applications. In comparison with thin-films, these PZT nanorod structures show an improved piezoelectric response owing to its reduced substrate clamping [110]. Our nanorod arrays have exhibited an excellent ferroelectric hysteresis behavior with remnant polarization of $\sim 16\ \mu C/cm^2$ with improved polarization switching behavior [110]. Since, each nanorod polarization can be controlled independently it also gives an added advantage to nonvolatile memory elements for the read/write operation [110].

The PZT nanorod arrays with the dimensions of 200 nm diameter, 600 nm height, and with an aspect ratio of 1:4, were grown on LSMO seed particles by magnetron RF sputtering [110]. Also, these nanorods display a hysteresis loop exhibiting a good ferroelectric character. These PZT nanorod arrays exhibit randomly oriented polycrystalline perovskite nanostructure, where each nanorod is single crystalline. Thus, the ferroelectric switching behavior is improved in these structures. Also, the polarization state of the domains is aligned along the

growth direction and each nanorod allows an independent control of the polarization state.

In the following section I provide some background on the nature of SHG and relevant mechanisms such as phase matching. To the bast of our knowledge, for the first time, SHG has been observed using PZT nanorod arrays. This observation would be important as in modern industry device miniaturization, larger storage capacity, and higher processing speeds have become the main priorities. To this end, we also demonstrated multiphoton pump-probe spectroscopy as part of this study and reported transient dynamics in these newly developed PZT nanostructures.

Phase Matching in SHG:

For efficient nonlinear frequency conversion, constructive interference of the SHG emissions generated by different sources in a material is needed. When a light incident on a material resulting in SHG, at a given point z in the material, there exist two second harmonic (SH) waves: (1) the SHG wave generated at z propagating with the phase velocity c/n_ω, (2) SH waves generated in the material up to z propagating with the phase velocity $c/n_{2\omega}$ (c is the speed of light and n_ω and $n_{2\omega}$ are refractive indices of the material at frequency ω and 2ω respectively). The constructive and destructive interference of these two waves will result in the total SHG intensity. The incident beam with the electric field E_ω at frequency ω generate SHG emission with 2ω frequency and $P_{2\omega}$ nonlinear polarization. This $P_{2\omega}$ radiates an electromagnetic field with $E_{2\omega}$ [111],

$$\Delta^2 E_{2\omega} - \epsilon_0 \mu \frac{\partial E_{2\omega}}{\partial t^2} = \mu \frac{\partial P_{2\omega}}{\partial t^2}. \tag{1.10}$$

By solving the evolution of the SHG field $E_{2\omega}$ and the fundamental field E_ω, and considering the intensity $I_{2\omega} \propto |E_{2\omega}|^2$, the SHG intensity at a distance z is given as [111]:

$$I_{2\omega} = 2\left(\frac{\mu_0}{\epsilon_0}\right)^{(3/2)} \frac{\omega^2 \chi^{(2)} z^2}{{n_\omega}^2 n_{2\omega}} I_w(0)^2 \left(\frac{\sin\frac{1}{2}\Delta k z}{\frac{1}{2}\Delta k z}\right)^2, \tag{1.11}$$

where $\Delta K = K_{2\omega} - K_\omega($ where $K = 2\pi/\lambda$, is the wave vector), ω is the fundamental frequency, and $\chi^{(2)}$ is the second order susceptibility. In Eq. 1.9, the fundamental intensity I_ω deplete when propagating into the material lowering the efficiency of the SHG. Moreover, for efficient SHG conversion $\Delta K = 0$ has to be fulfilled, consequently the *sinc* term goes to its limit 1. This is the "phase matching condition". Thus,

$$K_{2\omega} = 2K_\omega, \tag{1.12}$$

which also showcases that momentum is conserved in the SHG process. By translating Eq. 1.10 into a relation between refractive indices(n_ω and $n_{2\omega}$) one can arrive at $n_\omega = n_{2\omega}$. This condition can only be satisfied in a birefringent material.

For an isotropic material due to the normal dispersion, where the refractive index increase with the increasing frequency of light, this condition is not satisfied. In the case of $\Delta K \neq 0$, the distance over which SHG intensity falls off to zero is the coherence length, l_c is given as [111]:

$$l_c = \frac{2\pi}{\Delta k} = \frac{\lambda_\omega}{2(n_{2\omega} - n_\omega)}. \tag{1.13}$$

For practical applications, high conversion efficiency of SHG is needed. The most widely used technique is using a birefringent crystal to satisfy the phase-matching condition. Another technique is "quasi-phase matching". Here, the material structures are engineered such that each layer is made up with the thickness of coherence length of the material and every alternating layer with opposite crystal orientations (*i.e.* changing the nonlinear susceptibility),

such that the SH waves become in-phase at each coherence length. Thus, the constructive interference of SHG emissions generated by two adjacent layers results in enhanced SHG intensity. However the fabrication of quasi-phase matched material structures require costly and complex fabrication technologies, and are mainly employed for ferroelectric crystal applications.

For disordered polycrystalline materials, Baudrier-Raybaut *et.al* [112] have reported a "random quasi-phase-matching" condition as an alternative method to enhance SHG conversion efficiency [112]. They report that SH waves generated at different domains with different domain parameters (orientation, shape, and size) in a polycrystalline disordered sample, would acquire random phases [112, 113]. Thus, the interference effects are prevented and the sum of intensities of individual domains contribute to the total SHG intensity. Even though, "random quasi-phase-matching" frequency conversion efficiency is less than phase-matched or a Quasi-phase matched system, there exist less complex and low cost technologies to fabricate low dimensional polycrystalline material structures that are compatible with already existing commercial devices. Thus, random quasi-phase-matched systems allow applications of nonlinear optical technologies to be cost effective and also it facilitate the device miniaturization down to electronic chip scales [112].

Chapter 2

Experimental Techniques

2.1 Ultrafast Pump-Probe Spectroscopy

Pump-probe spectroscopy is a powerful tool to study ultrafast dynamical properties of materials. Altering a material system with short laser pulses using this approach can strongly modify the thermodynamic equilibrium among the carriers, spins, and ultimately the lattice. The dynamical behavior of non-equilibrium carriers generated by intense pump pulses can provide valuable information about: (1) electronic structure, (2) different carrier scattering and relaxation mechanisms, including carrier phonon coupling and carrier-carrier scattering, and (3) carrier spin states and spin relaxation. Furthermore, as the switching rates in electronic devices are pushed to even higher frequencies, it is important to understand carrier dynamics phenomena in semiconductors on femtosecond time-scales. Optical spectroscopy with femtoscecond time resolution allows us to generate and monitor coherent optical polarization and carrier distribution in real time.

In a typical pump-probe setup, the pump pulse excites the material system creating non-equilibrium distribution of carriers, and time delayed probe beam can probe the material's response as a function of time. Following photoexcitation, the photon energy can be transferred to the carriers creating a non-equilibrium distribution of carriers with elevated lattice temperature. Eventually the excited systems' energy and momentum relax back as the system achieves equilibrium. Before relaxing back to the thermal equilibrium, these excited

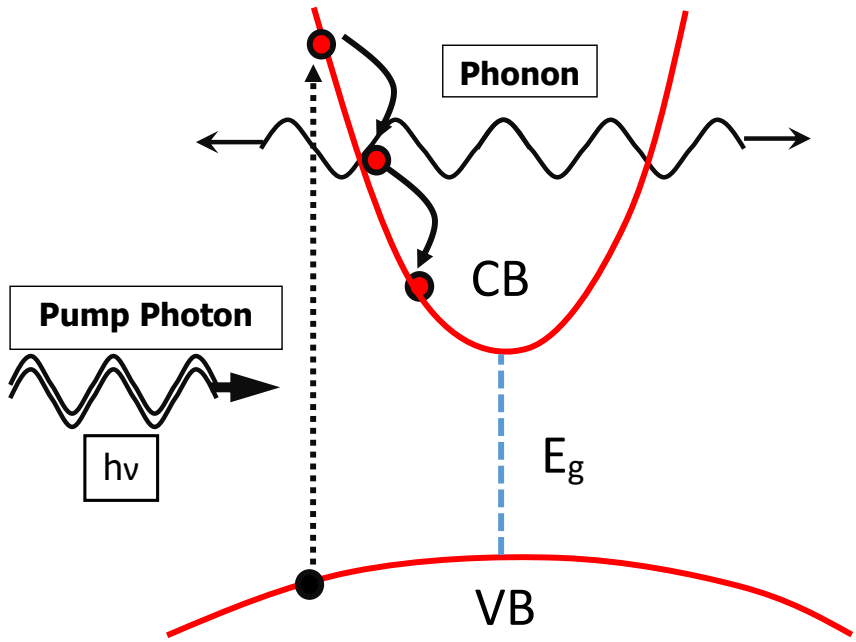

Figure 2.1: Schematic representation of a photoexcitation and relaxation process in a direct gap semiconductor, where CB is the conduction band, VB the valence band, and E_g is the energy gap. Here, an electron and hole pair is generated through pulse laser excitation, and in the process of cooling down, both *non-coherent phonons* and *coherent phonons* can be generated.

carriers go through several relaxation processes. These relaxation regimes are categorized into four temporal regimes: Coherent Regime, Non-Thermal Regime, Hot-Carrier Regime, and the Isothermal Regime [114]. These are temporally overlapping regimes where different regimes can occur concurrently.

In the coherent regime, the excited carriers have a well defined phase with respect to the electromagnetic field of the pump beam. This coherence lasts only a few femtoseconds as the scattering processes destroy the coherence [114]. The distribution function of the non-thermal regime is not characterized by a temperature, as in this regime, the excited carries are far from equilibrium [114]. Scattering processes such as carrier-carrier and exciton-exciton can

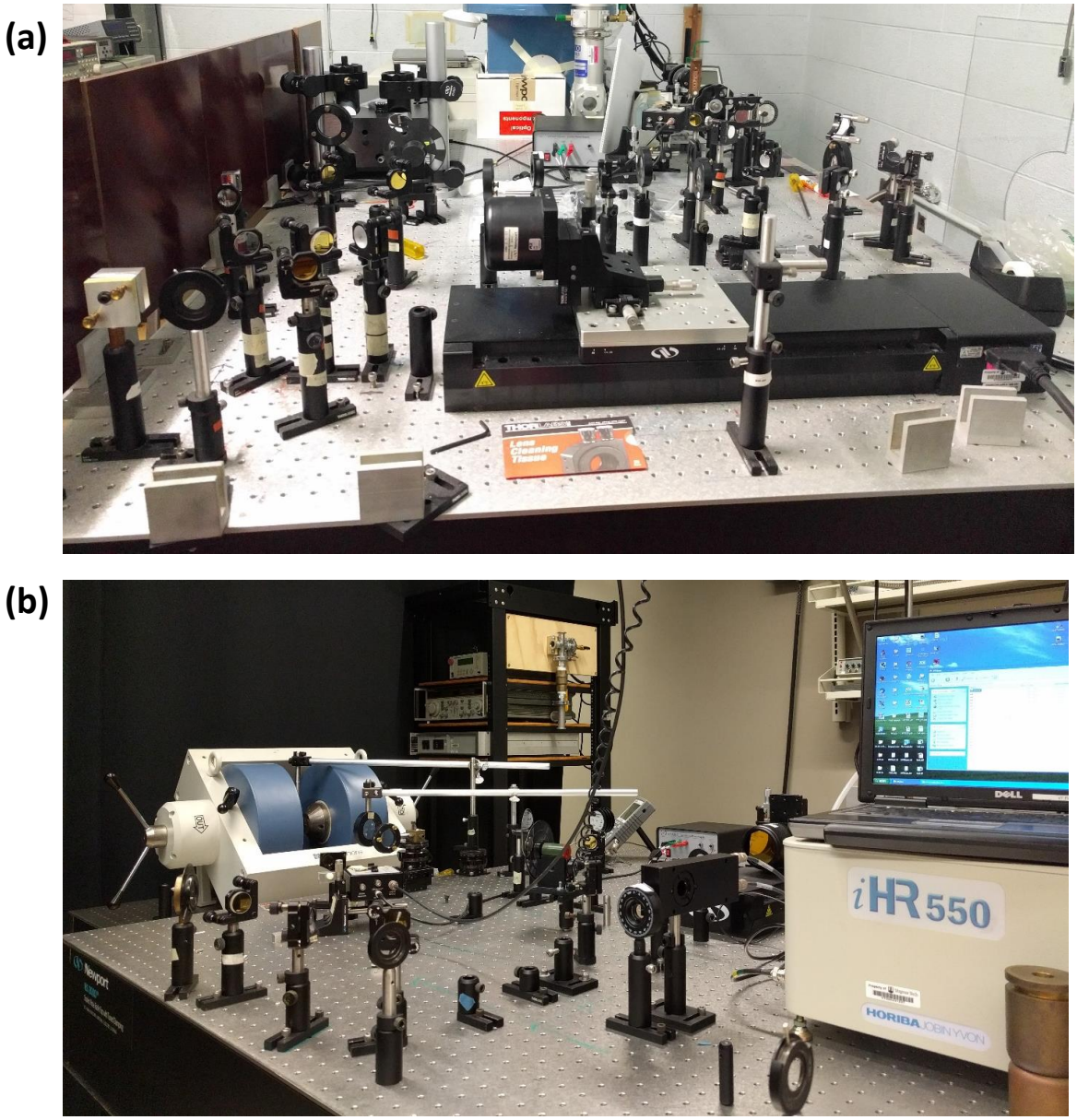

Figure 2.2: Time resolved pump-probe setup. (a) Non-degenerate pump-probe (400 nm pump and 800 nm probe) setup with Coherent amplified Ti:sapphire oscillator with a repetition rate of 1 kHz, a wavelength of 800 nm, and a pulse duration of 100 fs. (b) Degenerate pump-probe setup with a Coherent Chameleon Ti:sapphire laser with a repetition rate of 80 MHz, a wavelength range from 700 -1050 nm and a pulse duration of 100 fs. This setup also includes a 1 T variable electromagnet.

be investigated in this regime where the Coulomb interaction between carriers (electrons, holes) facilitate carrier-carrier scattering. Through these scattering processes, energy can redistribute among photoexcited carriers, resulting in a thermalized distribution of carriers [114].

After carrier thermalization, the temperature difference between the carriers and the lattice is mediated through creation of phonons [114]. In this hot carrier regime, the carrier temperature is higher than the lattice where the hot carriers achieve equilibrium with the lattice through the creation of optical phonons. At this stage a large population of optical phonons are generated and a majority of these phonons decay into multiple low energy acoustic phonons [114]. Finally, in the isothermal regime the system achieves the thermodynamic equilibrium through carrier recombination (radiative or non-radiative) and carrier diffusion [114, 115]. Due to the finite absorption depths in materials, carriers are generated only in the absorption volume generated by pump pulses. This fact can result in carrier diffusion in the system toward reaching to the equilibrium [115]. Apart from these relaxation processes, the creation of large electron densities after photoexcitation can also result in several many body effects such as bandgap renormalization, exciton screening, and band-filling [24, 116].

2.1.1 Time Resolved Differential Reflectivity Spectroscopy

The refractive index of a material is directly correlated with its optical absorption, reflection, and the transmission properties, besides, the change in the dielectric function of a material can change the corresponding refractive index. The Drude model describes the relationship between dielectric function and the carrier density as following [115]:

$$\Delta\epsilon(\omega_L, t) = \sum_i \frac{\Delta N_i(t) e^2}{\epsilon_0 m_i \omega_L^2}, \tag{2.1}$$

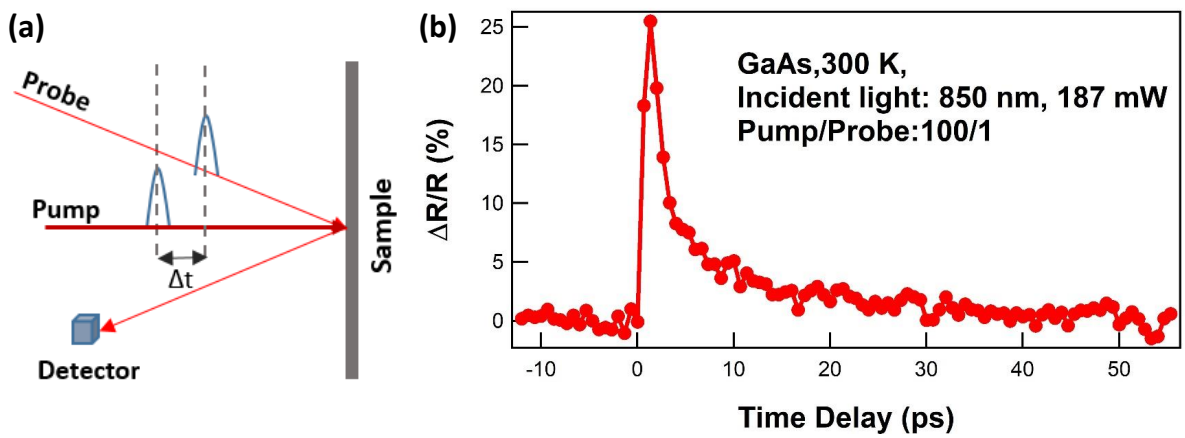

Figure 2.3: (a) A schematic representation of pump and the probe beam overlapping on the sample. (b) Differential reflectivity plot for relaxation dynamics of GaAs at room temperature. We use GaAs to test our setup.

where ω_L is the laser frequency, $N_i(t)$ is the carrier density, and m_i is the mass in the ith energy band. Thus, following a pump excitation, changes in the carrier density directly alters the dielectric function, which changes the optical properties in the system.

When it comes to time resolved transmission and reflection there are major differences. In differential transmission dynamics, the results are based on the exact energies and states of the photoexcited carriers. In contrast, differential reflection dynamics are based on the band that carriers occupied [115]. Moreover, the many-body effects are more prominent in differential transmission experiments compared to the differential reflection experiments [116].

The time resolved experiments pursued in this dissertation were mainly focused on transient reflectivity (differential reflectivity), using both degenerate and non-degenerate pump-probe. In the degenerate case, the laser source is divided into two paths using a beam splitter, and the pump pulses reflects off of a retroreflector, on a moving stage which controls the required time delay (path difference) between the pump and the probe. (Fig. 2.3(a)). In

our measurements, we used a Si photodiode detector. In the non-degenerate scheme (two-color), a BBO crystal was used on the pump path to double the frequency. In the initial alignments of the optical setup, we often use GaAs as our test sample. Figure 2.3(b) displays a degenerate differential reflectivity measurements in GaAs at 300 K.

2.1.2 Time Resolved Optically Induced Birefringence Spectroscopy

Optically induced birefringence (OIB) [117] can occur when the electric field of the incident light induces a change in refractive index in the medium. Birefringence is a nonlinear optical property, where the refractive index of the material depends on the properties of light such as polarization and direction of propagation. This fact originates from the third order susceptibility term of the optical medium. Thus, this is only observed in optically anisotropic media. However, optically isotropic materials with anisotropic third-order susceptibility tensor can induce birefringence under uniaxial stress where, the most common example for this scenario is GaAs.

A pump-probe scheme can be employed to investigate the temporal evolution of OIB: TROIB. Here, as noted earlier, pump pulses create the non-equilibrium carriers resulting in the change in refractive index in the medium. Thus, inducing two separate refractive indices in the two different transverse directions, which are perpendicular to the propagation direction of the incident pump beam. The resultant optically induced anisotropic birefringent medium changes the linearly polarized probe beam to an elliptically polarized beam. The temporal evolution of the OIB is monitored by measuring the induced phase change via a Si balanced detector. In the process of carrier relaxation, OIB follows a similar evolution as a function of time, allowing one to investigate the temporal dynamics of OIB.

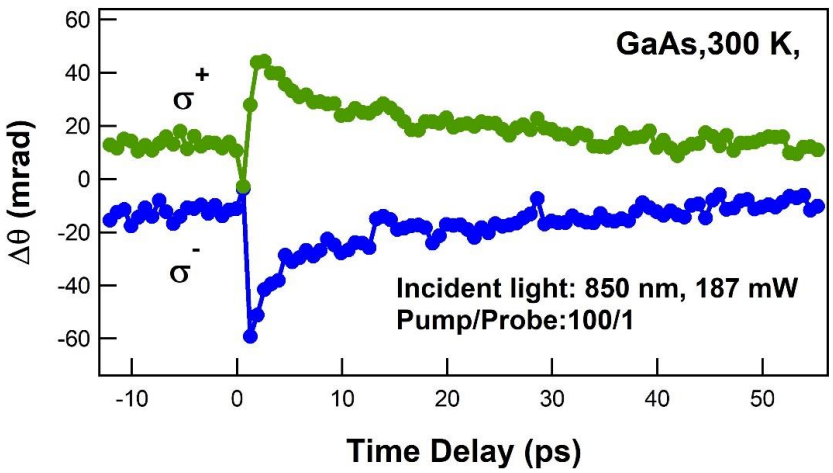

Figure 2.4: TRMOKE responses collected for GaAs at room temperature with a degenerate pump-probe setup. Green and blue plots reprecent the TRMOKE signal from right circularly polarized (σ^+) and left circularly polarized (σ^-) light respectively. We use GaAs to test our setup.

2.1.3 Time Resolved Magneto Optical Kerr Effect Spectroscopy

In the case of Magneto-Optic Kerr Effect (MOKE) [118], when light is reflected off of a magnetized medium, the resultant rotation of the polarization plane of the light is dependent on the magnetization of the sample. Here, the magnetization of the material can result from inherent magnetization of the material, when the material is subjected to an external magnetic field, and also by optically induced magnetization after a photoexcitation using circularly polarized light. Thus, MOKE is also observed due to the optical anisotropy of the medium. Similar to the Faraday effect [119], where light transmitted through a magnetized medium changes its polarization state, in MOKE, when a linearly polarized light is reflected off of a magnetized medium, it changes into an elliptically polarized beam [21, 118].

The interaction of the electric and magnetic field of the incident probe beam with the spin of the electron causes the change in polarization state of the incident beam; that is from linearly polarized to elliptically polarized. Linearly polarized light can be illustrated as a

superposition of right and left circularly polarized light and has different refractive indices when traveling through a magnetic material (n_{σ^+} and n_{σ^-}) resulting in an elliptically polarized beam. The Kerr rotation (θ_k) and the Kerr ellipticity (η_k) along with inherent material properties are as following:

$$\eta_k + i\theta_k = \frac{-(\kappa^+ - \kappa^-)}{2n(n^2 - 1)}, \tag{2.2}$$

where n is the index of refraction, and κ^+ and κ^- are the optical susceptibilities of the material for right (σ^+) and left (σ^-) circularly polarized light, respectively. Here, $(\kappa^+ - \kappa^-)$ is proportional to the magnetization of the material; thus, the change in the polarization state is proportional to the magnetization of the material system. MOKE has been widely used to study magnetic materials, to study the magnetic characteristics of material systems such as magnetic phase transitions, spin density of states, and magnetic domain structure [120, 121, 122].

Taking advantage of the selection rules in the presence of the spin orbit interaction, one can use a circularly polarized pump beam to selectively excite spin polarized carriers. The excited non-equilibrium spin population can induce an instantaneous magnetic characteristic (laser induced magnetism). The relaxation of this spin population can be investigated through a transient rotation of a linearly polarized probe beam. Thus, TRMOKE is an essential spectroscopic technique to investigate the high speed magnetization dynamics of the magnetic materials as well as to study the spin relaxation dynamics of non-magnetic materials [123]. Similar to TRDR optical setup, for initial TRMOKE setup testing we use GaAs as the test sample. Figure 2.4 shows a TRMOKE response of a GaAs film, which showcase the helicity dependence of the pump beam.

2.2 Non-linear Optics

Nonlinear optical techniques are essential to understand the underlying electronic and magnetic structures of materials via light-matter interactions. In contrast with linear optical techniques, nonlinear optics provide additional degrees of freedom to reveal underlying properties in material systems. High degree of coherence and high intensity are the crucial requirements of the laser excitation to observe and investigate nonlinear optical properties of material systems. The relative displacement of the atoms or molecules of a material, upon incidence of a light beam induce a secondary electric field. The induced polarization (P) is linearly dependent on the electric field of the incident light (E). Furthermore, with high intensity light the induced polarization can be expressed as a power series of the E [124].

$$P(t) = P_0 + \varepsilon_0 \chi_e E(t) + \chi^{(2)} E^2(t) + \chi^{(3)} E^3(t) + ..., \tag{2.3}$$

where P_0 is a constant polarization, χ_e is the linear susceptibility of the material and $\chi^{(2)}, \chi^{(3)}, ...$ are the higher order susceptibility terms.

This can be explained classically using a electron in a medium under a strong electric field. The high frequency of the electric field causes the electron to oscillate anharmonically, resulting in nonlinear dipole moments. Thus, the resultant polarization depends nonlinearly on the incident electric field resulting in different frequency generations. Depending on the inherent material properties, materials will display zero or non-zero susceptibilities. For an example, every material exhibits nonzero χ_e and $\chi^{(3)}$ values whereas, $\chi^{(2)}$ is nonzero only in non-centrosymmetric material structures where the inversion symmetry is broken [125].

The nonlinear optical phenomenon results from the interaction of light with a nonlinear medium. To be precise, the field generated by the incident light in a nonlinear medium, gives rise to nonlinear effects such as SHG. The electric field of the incident light results

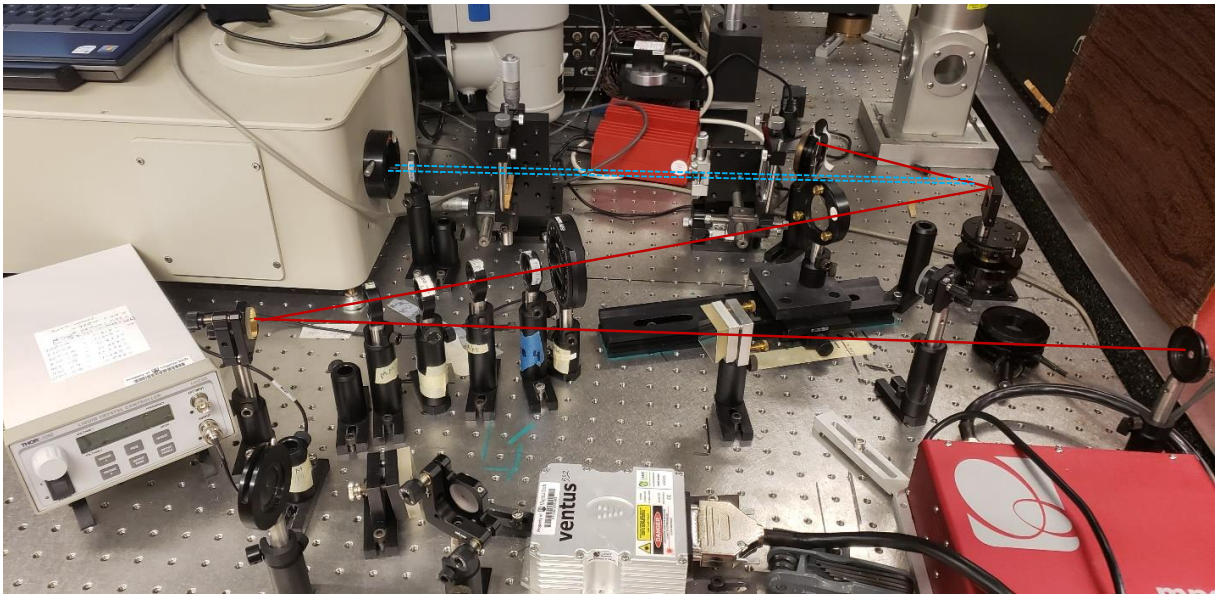

Figure 2.5: Photoluminescence experiment setup. SHG can be detected using our photoluminescence setup.

in an atomic dipole moment in the material. In the regime of week electric field, one can consider $P(t)$ and $E(t)$ are linear. The nonlinear optical response can be observed only in high intensity electric field regimes, where the electric field of the light is comparable with the interatomic electric fields. Therefore, pulse lasers are suitable as sources to observe nonlinear optical phenomena [126].

2.2.1 Second Harmonic Generation Spectroscopy

SHG is the lowest order nonlinear process where incoming photons interact with a nonlinear media and emit light with twice the energy of the initial. The second term in Eq.(2.2) gives rise to the second-order nonlinear optical phenomena. This is also known as the three-wave mixing, where a nonlinear medium interacts with two light waves with different frequencies (ω_1 and ω_2) and produce a third wave with either sum of frequency ($\omega_3 = \omega_1 + \omega_2$) or the

difference of frequency ($\omega_3 = \omega_1 - \omega_2$) [111]. In the case of SHG sum of the frequency is resultant from two waves with the same frequency ($\omega_1 = \omega_2$). Here, $\chi^{(2)}$ is the second-order nonlinear electric susceptibility. Three-wave mixing is widely explored in the pulse laser industry, for laser amplification and to generate broadband frequency laser pulses. The high-order terms are relatively weak, therefore in most cases, one can only observe second- and third-order nonlinearities. The polarization is an odd function, in a nonlinear material system with an inversion symmetry (*i.e.* a centrosymmetric medium). Therefore, one can only observe second-order nonlinear phenomena in a medium where inversion symmetry is broken.

SHG is generated in media where the inversion symmetry is broken. Thus, it is commonly observed in non-centrosymmetric media and at the surfaces and interfaces. SHG has effectively been used to explore symmetric and non-symmetric structures [27, 28, 29, 30, 31, 32]. On the other hand, SHG is an effective tool to study magnetically ordered materials [127], as long-range magnetic order breaks the time inversion symmetry. In a magnetically ordered material, the second-order nonlinear electric susceptibility has both structural and magnetic order parameter contributions: a time-invariant component with a crystallographic contribution and a time-variant component with a linear spin-dependent contribution. Therefore, SHG is a vital tool to study underlying electric and magnetic symmetries in multiferroic materials. In this study I will present the observed SHG in several multiferroics.

Chapter 3

Coherent Acoustic Phonons and Ultrafast Carrier Dynamics in Hetero-Epitaxial $BaTiO_3$-$BiFeO_3$ Films and Nanorods

This chapter was reproduced from Ref. ***J. Mater. Chem. C, 2019, 7, 14212*** *with permission from The Royal Society of Chemistry, with minor changes*

In this chapter, I am sharing one of my main findings which in the study of coherent acoustic phonons and ultrafast carrier dynamics in multiferroic structures. In this study, we performed time resolved differential reflectivity measurements of $(1-x)$BaTiO$_3$-(x)BiFeO$_3$, with $x = 0.725$ epitaxial films grown on a Lanthanum Strontium Manganite (LSMO) layer with a Strontium Titanate (STO) substrate, and BaTiO$_3$-BiFeO$_3$ nanorods grown on Pt/Si. Our results demonstrate the intriguing possibility dynamically manipulating the strain in less explored materials systems. My contribution to this project was, setting up the degenerate and two color pump-probe experiments and conducting room temperature TRDR measurements of all available BTO-BFO structures (more

than 23 structures) in order to find suitable structures for this study. I also wrote a large portion of the experimental sections.

3.1 Introduction

The desire to create monolithic multifunctional devices has driven significant research toward exploring multiferroics, where the coupling between electric, magnetic, optical, and structural order parameters [9, 110, 128, 129, 130], can provide new functionality. Multifunctionality in a single material allows for the development of novel devices such as: low energy and high speed computer memory elements [131, 132], high efficiency photoelectric devices [133], conversion of photons from optical to THz [134, 135] frequencies, and new electronic architectures [136]. Multiferroics have potentials for many applications [9, 128, 137, 138, 139, 140, 141], such as ultrafast non-volatile ferroelectric memory [139, 142], spintronic devices [140], and energy harvesting [143, 144]. Furthermore, strained multiferroic materials and their heterostructures have the potential for phononic device applications in which photons and phonons can couple strongly [145, 146, 147, 148, 149, 150, 151].

Among the various multiferroics, bismuth ferrite ($BiFeO_3$) is one of the most studied lead-free material systems. However, it suffers from decreased ferroelectric polarizability which results from large leakage currents mainly due to the presence of multivalent Fe ions and oxygen vacancies [138, 139, 140, 141, 142, 143]. We have shown earlier [9] that the addition of $BaTiO_3$ to $BiFeO_3$ reduces the conductivity of the mixture which decreases the leakage current, potentially allowing for a better multiferroic material. A similar observation was reported by Park *et al.* [152]. In both studies, a wide range of material compositions were synthesized. This solid solution approach has the advantage of enhancing the magnetoelectric (ME) properties. In our previous study [9], (1-x)$BaTiO_3$-(x)$BiFeO_3$ admixtures

with x between 0.725 and 0.750, were demonstrated to have a larger ME coupling compared to $BiFeO_3$ due to active spin modulation of the Fe-O-Fe bond [9, 152]. We also recently reported room temperature ferromagnetic resonance in 80 nm thick $BaTiO_3$-$BiFeO_3$ grown on 100 nm thick lanthanum strontium manganite (LSMO), where this hybrid heterostructure was found to show small Gilbert damping of 0.004 [153]. This fact offers opportunities for employing this material system for a spin transfer where potentially a spin current can be generated without the existence of charge current in the $BaTiO_3$-$BiFeO_3$ layer [153].

In this paper, we use time resolved pump-probe differential reflectivity measurements (TRDR) to study our (1-x)$BaTiO_3$-(x)$BiFeO_3$ admixtures. We studied several different (1-x)$BaTiO_3$-(x)$BiFeO_3$, $x = 0.725$ films as well as nanorods. Our studies provide information primarily on generation and propagation of acoustic coherent phonons (CPs) (sound velocities and indices of refraction) and to a lesser extent on the dynamics of photo-excited carriers (diffusion constants). For carrier dynamics, pump-probe studies of the transient reflectivity allow probing the time scales for carrier diffusion, inter-band scattering, carrier trapping, and band to band recombination of the photoexcited electrons and holes [116]. Compared to our previous studies on (1-x)$BaTiO_3$-(x)$BiFeO_3$ poly-crystalline structures reported in [154, 155], these new films studied here have the advantage of lower disorders and a well-defined layered structure. In addition to the films, we also examined $BaTiO_3$-$BiFeO_3$ *nanorods*, in which the smaller substrate clamping effect is expected to lead to stronger mechanical coupling and thereby to higher piezoelectricity and magnetostriction than in the films [110].

$BiFeO_3$ is G-type antiferromagnetic (AFM), where within the (111) plane, the magnetic spins are ferromagnetically aligned, while between the adjacent (111) planes, they are antiferromagnetically aligned. The Dzyaloshinskii-Moriya interaction produces a weak canting moment, thereby leading to weak in-plane FM [156]. In bulk (as opposed to the films) this orientation is modulated to a spiral spin structure, whose AFM vector has a wavelength of

62-64 nm, resulting in local weak AFM in $BiFeO_3$ [157, 158]. Several investigations have shown that an inherent net magnetization can be achieved if one can suppress the spiral spin structure [156, 157, 158, 159, 160, 161].

This spiral structure is believed to be suppressed in nanostructures, such as nanoparticles, nanotubes, and nano-wires. This is our motivation for studying the nanorods. Recent approaches show enhanced magnetization correlated with the decreasing of the nanorod diameter below the wavelength of the spiral order [158]. Reducing the dimensionality from the films to nanorods (quasi-1 dimensional) was expected to enhance the possibility of detecting coherent magnons in the nanorods [20]. For antiferromagnet or ferromagnet magnons, one would expect an increase in frequency with applied magnetic field which motivated us to probe the magnetic field dependence of the time resolved dynamics in our studies. We also note that multiferroics networks of $BiFeO_3$ nanorods [162] displayed enhanced magnetism compared to the bulk $BiFeO_3$, arrays of $BiFeO_3$ quantum dots [132] exhibited bipolar resistive switching, and composite rod-bulk structures [163] demonstrated enhanced ferroelectricity. This also is a motivation for studying the nanorods.

3.2 Sample Preparation and Characterization

3.2.1 $BaTiO_3$-$BiFeO_3$ Films

The characteristics and geometry of the samples investigated in this paper are summarized in Table 4.1 and we provide a brief introduction to the growth procedures. The lattice mismatch of the $BaTiO_3$-$BiFeO_3$ with respect to the strontium titanate, $SrTiO_3$ (STO) substrate and LSMO film is small which allows it to be epitaxially grown on both materials. Hetero-epitaxial $BaTiO_3$-$BiFeO_3$/LSMO thin films were grown on (001) oriented STO substrates

Table 3.1: Structural details of the samples studied in this work. (In our preliminary investigations, we have probed the following structures and the published work presents the structures with the best dynamical responses.) Note: *In the case of the nanorods, the LSMO layer refers to nano-sphere arrays.

Sample	Thickness LSMO (nm)	Thickness BTO-BFO (nm)	STO Orientation	Structure
1		100	(001)	LSMO/STO
2	5	660	(001)	BTO-BFO/LSMO/STO
3	5	660	(110)	BTO-BFO/LSMO/STO
4	5	660	(111)	BTO-BFO/LSMO/STO
5	20	80	(001)	BTO-BFO/LSMO/STO
6	20	80	(110)	BTO-BFO/LSMO/STO
7	20	80	(111)	BTO-BFO/LSMO/STO
8	40	80	(001)	BTO-BFO/LSMO/STO
9	40	80	(110)	BTO-BFO/LSMO/STO
10	40	80	(111)	BTO-BFO/LSMO/STO
11	40	40	(001)	BTO-BFO/LSMO/STO
12	40	40	(110)	BTO-BFO/LSMO/STO
13	40	40	(111)	BTO-BFO/LSMO/STO
14	40	660	(001)	BTO-BFO/LSMO/STO
15	40	660	(110)	BTO-BFO/LSMO/STO
16	40	660	(111)	BTO-BFO/LSMO/STO
17	100	80	(001)	BTO-BFO/LSMO/STO
18	100	80	(110)	BTO-BFO/LSMO/STO
19	100	80	(111)	BTO-BFO/LSMO/STO
20	100	660	(001)	BTO-BFO/LSMO/STO
21	100	660	(110)	BTO-BFO/LSMO/STO
22	100	660	(111)	BTO-BFO/LSMO/STO
23 (nanorods)*	500			BTO-BFO/LSMO/Pt/Si

by off-axis RF magnetron sputtering. Prior to the film deposition, the surface of the STO substrates was treated by buffered oxide etchant (BOE) and subsequently annealed at 900°C under an O_2 atmosphere to make a Ti-terminated surface. First, the LSMO thin film was deposited on the Ti-terminated STO substrate at 600 ^{o}C under 5 mTorr of pressure with 8:2 O_2:Ar gas ratio and 4.93 W/cm^2 of RF power. The $BaTiO_3$-$BiFeO_3$ thin film was grown

on the epitaxial LSMO thin films at 400 ^{o}C using an in-situ deposition under the same RF power and pressure with 1:9 O_2:Ar gas ratio.

Cross-sectional scanning electron microscopy (SEM) image for one of the samples (sample 20), shows the $BaTiO_3$-$BiFeO_3$/LSMO thin film grown on the STO (Fig. 4.1(a)). The ferromagnetic (FM) and FE characteristics of this sample are presented in Fig. 4.1(b). The temperature dependent magnetization of the $BaTiO_3$-$BiFeO_3$/LSMO at 0.5 T, indicates that the film has non-zero magnetization at room temperature (RT). The inset in Fig. 4.1(b) shows the FE polarization-electric field (P-E) curve of the $BaTiO_3$-$BiFeO_3$ film. It shows the typical and unambiguous FE characteristics. The crystal structures of the epitaxial LSMO film and hetero-epitaxial $BaTiO_3$-$BiFeO_3$/LSMO thin films grown on (001) oriented STO substrates were confirmed through X-ray diffraction (XRD) analysis. The films were found to be epitaxially grown along the c-axis of the STO substrate without any secondary phases, as illustrated in Fig. 4.1(c). The peak splitting corresponding to (001) and (002) planes, indicates that the film is grown with the rhombohedral phase as reported in Ref. [9]. Our previous X-ray diffraction of the $BaTiO_3$-$BiFeO_3$ poly-crystalline film also showed that the film was in a pure perovskite phase and no pyrochlore phase was observed [155].

Figure 4.1(d) shows phi-scan XRD patterns of $BaTiO_3$-$BiFeO_3$/LSMO epitaxial films. Azimuthal phi-scans of $BaTiO_3$-$BiFeO_3$ and LSMO films show in-plane epitaxy with a cube-on-cube epitaxial relation. The $(1-x)BaTiO_3$-$(x)BiFeO_3$, $x = 0.725$ used in this work, is a solid solution with the rhombohedral phase which has lattice parameter of a=3.982 Å, rhombohedral distortion angle of 89.99^o and unit cell volume of 63.31 Å^3 in its bulk form.

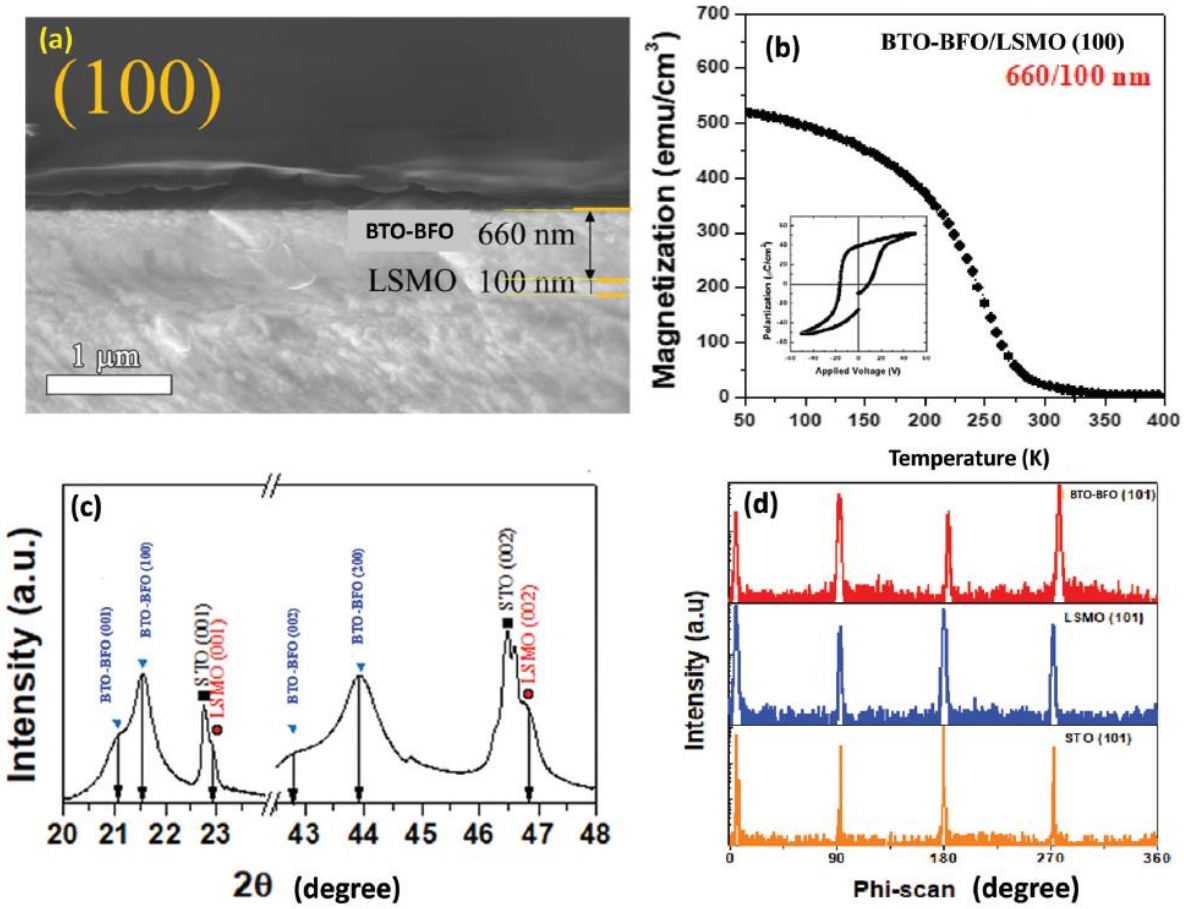

Figure 3.1: (a) SEM image of the layer structure of the $BaTiO_3$-$BiFeO_3$ film investigated in this study (sample 20). (b) The magnetization as a function of temperature at 0.5 T, and the inset shows FE loop at room temperature demonstrating the multiferroic nature. (c) The XRD of sample 20 shows a single phase for the $BaTiO_3$-$BiFeO_3$ film. (d) Here we present, (101) Phi-scan XRD patterns of $BaTiO_3$-$BiFeO_3$/LSMO epitaxial layers grown on (100) STO substrate (sample 20). The films are grown through (001) direction and the phi scan was performed with (101) space to evaluate the epitaxial quality. Note: The labels BTO-BFO refer to $BaTiO_3$-$BiFeO_3$.

3.2.2 $BaTiO_3$-$BiFeO_3$ Nanorods

As shown in Fig. 3.2(a), 0.275 $BaTiO_3$ - 0.725 $BiFeO_3$ nanorods (sample 23) were grown on 20 nm size LSMO seeds. These nano-sphere seeds were patterned on top of Pt coated Si (100) substrate through polymer nano-template method followed by RF sputtering, at 400^oC. The spherical LSMO seeds drive vertical growth of the $BaTiO_3$-$BiFeO_3$ nanorods due to the minimization of overall surface energy. The nanorod arrays were synthesized with ∼200 nm diameter and ∼500 nm height, as shown in the side view image in Fig. 3.2(b). This method for growing $BaTiO_3$-$BiFeO_3$ nanorods is similar to the techniques employed for synthesizing $PbZr_{0.52}Ti_{0.4_8}O_3$ (PZT) nanorods and the details can be found in Ref. [110].

Through SEM measurements, we found that the $BaTiO_3$-$BiFeO_3$ nanorods (Fig. 3.2(b)) exhibit close-packed structure [110] and have a nearly homogeneous diameter and height (these closed-packed microstructures are homogeneous up to 3-inch wafer scale). From XRD measurements, the nanorod arrays were found to be single perovskite phase without any secondary phases such as pyrochlore phase ($A_2B_2O_7$), as shown in Fig. 3.2(d). The XRD pattern also indicates that the nanorods are poly-crystalline. However, based on previous results on $PbZr_{0.52}Ti_{0.48}O_3$ using the same growth procedure [110], we expect that a single nanorod, is a single crystal but each nanorod has different crystal orientation, which imparts the overall poly-crystalline nature.

The difference in the thermal expansion coefficient between the thin film and substrate usually can create internal stress when they are synthesized at high temperature and then cooled down to room temperature. This thermal stress results in the preferred orientation of the thin films because the thin film is strongly clamped on the substrate during the cooling process. The nanorods show randomly oriented XRD peaks like bulk materials. This indicates that thermal stress is not induced into the sample during the cooling process

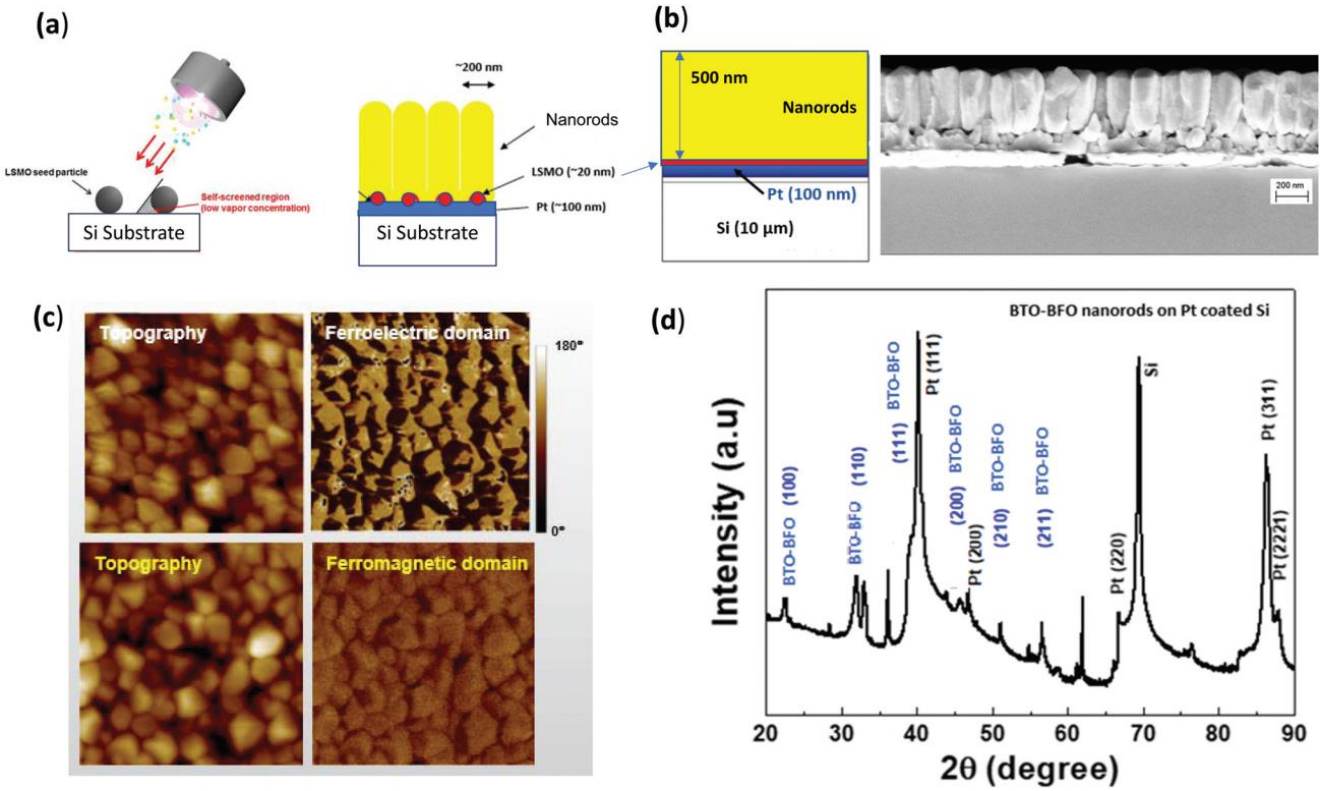

Figure 3.2: (a) Schematic of the nanorods growth on spherical LSMO seed particles. The seeds were arranged using polymer nano-sphere coating followed by LSMO deposition. (b) A side view SEM image of the nanorods on 100 nm Pt film. The red region refers to the LSMO spherical seed particles. (c) Atomic Force Microscopy images of $BaTiO_3$-$BiFeO_3$ nanorod arrays grown on Pt-coated Si substrate displaying topography, FE, and FM domains. (d) XRD patterns of $BaTiO_3$-$BiFeO_3$ nanorod arrays. Note: The labels BTO-BFO refer to $BaTiO_3$-$BiFeO_3$.

and the nanorods overcome the substrate clamping effect. This is significant because the substrate clamping effect in thin films significantly hinders the mechanical coupling of the ferroic orders, such as piezoelectricity in the FE materials, and magnetostriction in the FM materials. This effect occurs because the film is chemically bonded on the rigid substrate, which limits the mechanical movement of the thin film, under external excitation such as applied electric or magnetic field [110].

3.3 Results and Discussion

Time resolved differential reflectivity spectroscopy was performed on the epitaxial $BiFeO_3$ films and nanorods discussed above. Our results show a decay in $\Delta R/R$ with time which we attribute to the dynamics of the photoexcited carriers [19, 164, 165]. In our signals, we observe clear oscillations and "bumps" and we associate them to the generation of coherent longitudinal acoustic (LA) phonons near the surface of the sample and their subsequent propagation into the sample and other layers [166].

We previously [154, 155] performed time resolved measurements on *polycrystalline* $BaTiO_3$-$BiFeO_3$ where the second harmonic generation nano-imaging revealed disordered but distinct ferroelectric domains. In a two color pump-probe scheme (400/800 nm), we observed transient reflectivity responses and described the dynamics using a double exponential function, representing fast (2-7 ps) and slow (a few hundred ps) components [154]. We attributed the relaxation process to phonon-mediated as well as the diffusion of the photoexcited carriers. We also attribute an oscillation in $\Delta R/R$ (in GHz range) to the transverse acoustic phonons [155]. Furthermore, we observed a small magnetic field dependence in the amplitude of the transient reflectivity [155]. The electronic energy relaxation of polycrystalline $BiFeO_3$, deposited on STO and ytrrium stabilized ZrO2 (YSZ) substrates, were also studied using

a two color pump-probe spectroscopy (400/800 nm) [164]. In their work, the hot electrons were identified to decay with two different characteristic time scales. The fast process was attributed to scattering of electrons with lattice-vibration modes, and the slow one to the spin-lattice thermalization.

In this study, we improved the quality of our samples by making films, which had smoother, well-defined layers which allow us to better interpret the optical data. We performed pump–probe reflectivity measurements and our laser source was a Coherent amplified Ti:sapphire oscillator with a repetition rate of 1 kHz, a wavelength of 800 nm, and a pulse duration of 100 fs with $\sim$ 1 W output power. We used 90% of the output power for the pump path and the pump pulses were delayed respect to probe using a tunable delay line. The pump pulses were frequency doubled to 400 nm via a 0.5 mm thick BBO crystal generating pulses with a maximum power of 2 mW . The probe beam of 800 nm, had a spot size of $150-200$ μm with the pump being slightly larger ($\sim$ 250-300 μm). For the range of the pump powers used in this work (0.5-2 mW), we can estimate the pump fluence to vary from $\sim$ 0.7 to 4 mJ/cm^2. For the probe pulses, the power was fixed at ($\sim$ 10 μW), corresponding to a fluence of $\sim$ 30 μ J/cm^2. Both beams were focused on the samples using lenses. At room temperature, in order to increase the signal to noise ratio, the modulation frequency of the laser (1 kHz) was used to trigger the lock-in amplifier and at 100 K we modulated the pump pulses using a chopper at 211 Hz.

3.3.1 Carrier Relaxation Dynamics in $BaTiO_3$-$BiFeO_3$ Films

In this study the dynamical aspects of several BTO-BFO films, with different layer structures using a two-color pump-probe scheme (Table. 4.1) were probed. Here I will discuss only the ones in which a strong response to the photoexcitation have been observed.

Figure 3.3(a) presents examples of the observed TRDR in our two color pump-probe scheme at room temperature, for sample 17 at different pump powers. For comparison in Fig. 3.3(b), the TRDR on an LSMO film (sample 1) shows no response (or at least a much weaker one) from just this layer.

The observed decay in the differential reflectivity can be attributed to the dynamics of the photoexcited carriers near the surface [116]. The short absorption depth of the 400 nm pump pulse leads to a nonuniform photoexcited carrier density. The carrier contribution to the differential reflectivity [116] is proportional to the change in the *surface* carrier density in a given band, divided by the effective mass of the given band, and summed over all bands and is given by:

$$\frac{\Delta R}{R} \sim -\left(\sum_i \frac{\Delta N_i}{m_i}\right). \tag{3.1}$$

Note that a differential reflectivity measurement provides different information than a differential transmission measurement. In a differential transmission experiment, one measures the total number of carriers throughout the entire sample, at a *specific energy state* in a given band, that block the absorption of the probe pulse. In contrast, in the differential reflectivity, one only measures the carriers *near the surface*. In addition, the differential reflectivity depends only on the band in which the carrier is residing and is not sensitive to the specific energy state. For instance, phonon scattering from a given energy state would produce a change in the differential transmission signal, but would not produce a change in the differential reflectivity unless the carrier scattered into a *different* band with a *different* effective mass.

Changes in the differential reflectivity due to the carrier dynamics can occur for a variety of reasons [24]. These include: 1) scattering of carriers at the surface to *different* bands with

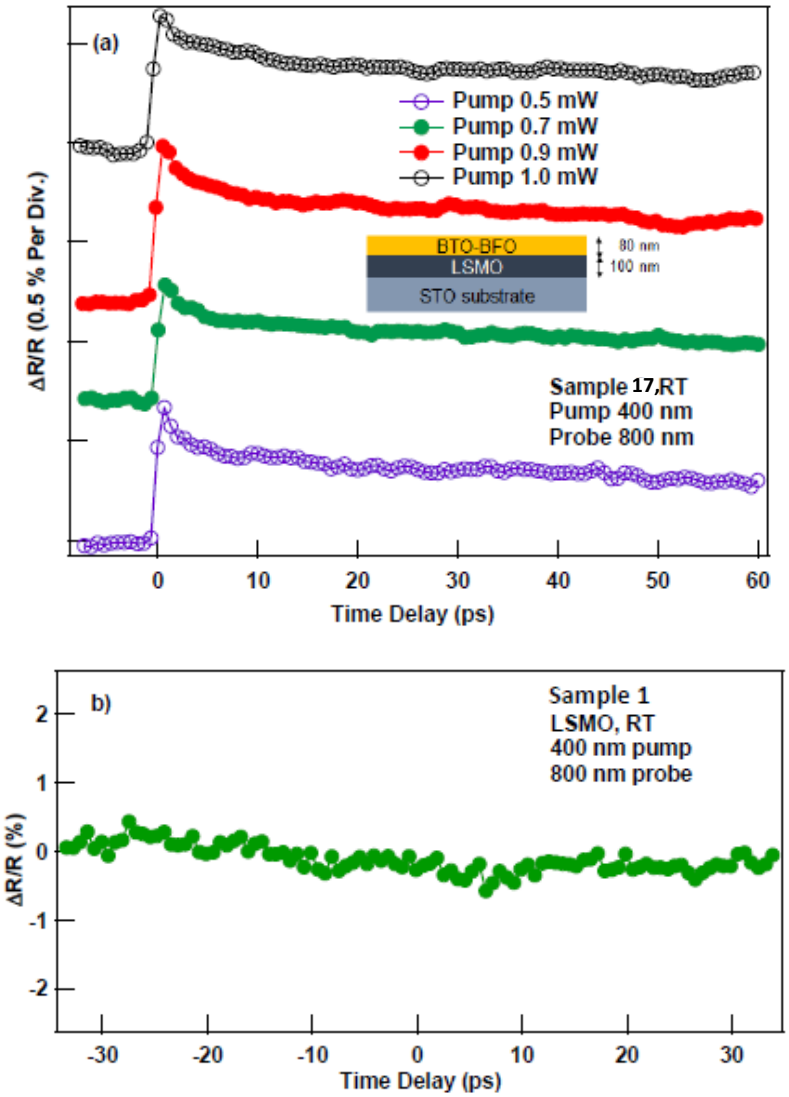

Figure 3.3: (a) TRDR of 80-nm thick $BaTiO_3$-$BiFeO_3$ (sample 17), measured at room temperature with the pump wavelength at 400 nm and probe at 800 nm, for different pump powers. The traces are offset for clarity and we refer to TRDR as the change in the transient reflectivity at positive time delay respect to the negative time delay. (b) TRDR on an LSMO (sample 1) film showing no detectable pump-induced response. Note: The labels BTO-BFO refer to $BaTiO_3$-$BiFeO_3$.

different masses; 2) recombination of photoexcited carriers (either through surface defects or band to band transitions); and 3) diffusion of carriers away from the surface. In addition, we note that the carriers can also influence the *bandgap renormalization* which can affect the differential reflectivity signal. We do not consider bandgap renormalization here.

The absorption depth of the 400-nm light in $BiFeO_3$ is 32 nm, whereas $BaTiO_3$ is transparent [167] at this wavelength. The absorption depth of the solid solution is therefore estimated to be in the range of 35-45 nm, much shorter than even our thinnest film. We therefore believe that the observed reflectivity responses are dominated by carrier diffusion away from the surface. We express the initial (t=0) depth distribution (z) of the photoexcited carriers in the sample by $N(z, t = 0) = N_0 e^{-\alpha z}$ where N_0 is the initial surface carrier density and α is the absorption coefficient. Then the carrier distribution at t>0, z>0 can be described by:

$$N\left(z = 0, t\right) = N_o e^{\alpha^2 Dt} \left[\operatorname{erfc}\left(\frac{\alpha Dt}{\sqrt{Dt}}\right)\right]. \tag{3.2}$$

Here D is the diffusion constant, and erfc is the complementary error function. Note that $1/\alpha^2 D$ has units of time and defines the time scale for the diffusion from the surface [116]. For small $t \ll 1/(\alpha^2 D)$ it decays as

$$N(0, t) \approx N_0 \left[1 - \frac{2}{\sqrt{\pi}} \alpha \sqrt{Dt}\right]. \tag{3.3}$$

This tells us that N_0 does not decay exponentially with a single time constant. (See appendix B of Ref. [116]). Instead, the decay of N_0 can be conveniently expressed with a time-dependent *instantaneous* decay rate γ(t), which is defined by:

$$\frac{d}{dt} N(0, t) \equiv -\gamma(t) N(0, t). \tag{3.4}$$

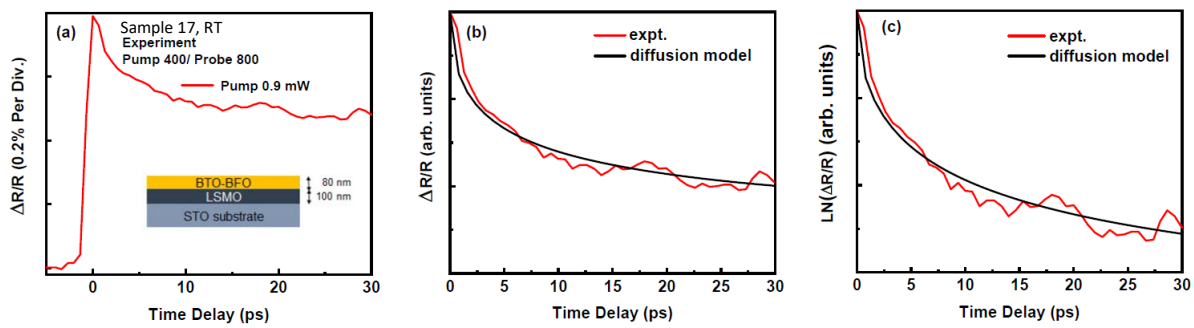

Figure 3.4: (a) The experimental differential reflectivity ($\Delta R/R$) of sample 17 at room temperature at pump power of 0.9 mW. Experimental reflectivity trace scales (red) compared with calculated $N_0(t)$ (black) from the diffusion model, assuming $1/\alpha^2 D = 10$ ps, plotted in the linear (b) and the natural log scale (c).

We can rewrite equation 3.4 as:

$$\gamma(t) \equiv -\frac{1}{N(0,t)}\frac{dN(0,t)}{dt} = -\frac{d\ \ln\ (N(0,t))}{dt}. \tag{3.5}$$

For small t, for a diffusive process, by using Eq. 3.5 and 3.3, this rate is given by: $\gamma(t) = \alpha\sqrt{\frac{D}{\pi t}}$. Note that this varies rapidly at short times and in fact, at $t = 0$ is infinite.

The model to describe surface carrier density $N_0(t)$ can reasonably reproduce the experimental data in Fig. 3.4. In doing so, we find that we get reasonable agreement if we set our diffusion time scale, $1/\alpha^2$ D = 10 ps. This would give a diffusion constant 1-2 cm^2/s, more than an order of magnitude less than the ambipolar diffusion coefficient for 400 nm photoexcitation in GaAs [168] which was estimated to be between 15 and 75 cm^2/s and seems plausible, given the disorder in the solid solution. In actuality, the diffusion coefficient could be even smaller than this since other processes can contribute to the decay of the signal as discussed above.

The relaxation mechanisms in our samples are different than those found in several recent

studies in similar systems. In a study by Doig *et al.* [20] a two-color time resolved pump-probe reflectivity (400/800 nm) of rhombohedral-like-BFO film on $LaAlO_3$ also showed non-exponential decay, where the initial relaxation was attributed to the phonon emission and the slower recovery to the non-coherent acoustic emission, spin lattice coupling or radiative recombination. Chen *et al.* [166] also probed the reflectivity dynamic of $BiFeO_3$ thin films in a two-color pump-probe where the observed excitation was triggered by transferring the electrons from the $2p$ valence band of O to the p conduction band of Bi. In this study, the number of the excited electrons generated by this non-thermal process was related to the amplitude of $\Delta R/R$. The cooling process was related to relaxation of high-energy electrons accumulated in the p conduction band of Bi, through the emission of longitudinal-optical (LO) phonons within several picoseconds. The ultrafast photo-induced absorption spectroscopy, in a single crystal of $BiFeO_3$ using sub-100-fs optical pulses in the near-infrared and ultraviolet ranges, was reported by Matsubara *et al.* [165]. In their study, It was concluded that the dominant transient absorption originated from the two-photon absorption process and collective electron-electron in addition to electron-phonon scattering, were the dominating relaxation mechanism.

3.3.2 Coherent Phonons in $BaTiO_3$-$BiFeO_3$ Film at Low Temperature

In this section, we investigated the oscillations in the TRDR of the $BaTiO_3$-$BiFeO_3$ films at low temperature which are associated with generation and propagation of coherent acoustic phonons. An example for sample 8 is shown in Fig. 3.5(a) for external fields up to 10 T at 100 K. The pump was 400 nm (with the power of $\sim$ 2 mW) and the probe, 800 nm. We note that there is an additional feature at 16-18 ps, which manifests itself as a "bump" in the decay signal, and is not sensitive to the magnetic field. We associate this feature with

the propagation of a coherent acoustic phonon generated at the surface (due to the short absorption depth (30-45 nm) of the 400 nm pump pulse) reaching the interface between the $BaTiO_3$-$BiFeO_3$ and the LSMO. The time it takes to reach to the interface is $t = L/v_s$, where L is the film thickness and v_s is the sound velocity of the solid solution.

While it is difficult to know the exact magnitude of acoustic sound velocity in the $BaTiO_3$-$BiFeO_3$ films, we do know that the Longitudinal Acoustic (LA) sound velocity is between 4.9 and 5.6 nm/ps in $BaTiO_3$ and is estimated to be in the range of 4.6-5.2 nm/ps in $BiFeO_3$ [169]. Therefore, in our samples, it is not unreasonable to estimate that the sound velocity is in the range of 4.5-5 nm/ps. If the sample thickness is 80 nm, then the coherent phonon generated at the surface that should reach the $BaTiO_3$-$BiFeO_3$/LSMO interface in about 16-18 ps which is consistent with the experimental data.

In 80 nm thick film sample, we do not see the usual periodic modulation of the transient reflectivity due to coherent acoustic phonons, in contrast to the previous studies [20, 47, 154, 166, 169]. This is because the film thickness of 80 nm is too small. The acoustic pulse, generated at the surface, is already into the LSMO layer before a single oscillation can occur.

With an 800 nm for probe pulses, using the speed of sound (v_s) to be 4.5 nm/ps and an index of refraction of 2.5 (between $BiFeO_3$ and $BaTiO_3$ for 800 nm), we would predict $T = \lambda_{probe}/(2v_s n) = 36$ ps. Considering this fact, the strain pulse has left the $BaTiO_3$-$BiFeO_3$ in 16 ps, before even half a cycle of oscillation for the CP; therefore we do not see any oscillations and the carrier relaxation is the dominant feature. We also note that the application of external magnetic field modified the reflectivity traces only modestly for the 80-nm thick sample.

As shown in Fig. 3.6, among the films studied here, only the 660 nm $BaTiO_3$-$BiFeO_3$ film (and also the nanorods) showed a clear sinusoidal modulation in the transient reflectivity

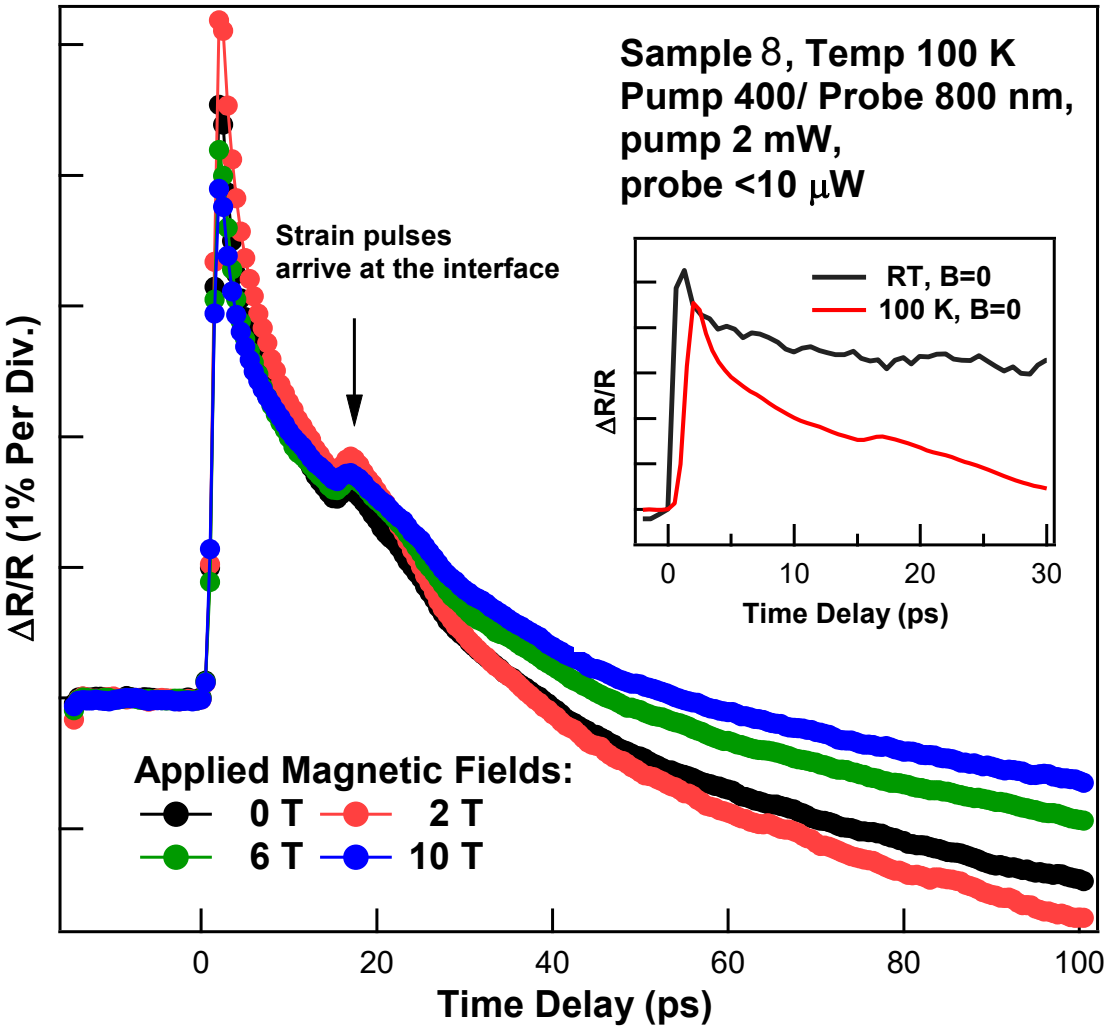

Figure 3.5: TRDR for sample 8 at 100 K for different external magnetic fields. The strain pulses arrive at the interface at $\sim$ 20 ps and CP oscillations are not observed in this sample likely due to the response being dominated by carrier relaxation in the region $<$ 20 ps where we would expect to observe them. The inset compares the reflectivity response of sample 8 at room temperature and 100 K, both without applying an external magnetic field (B=0). At 100 K, the carrier-induced change in the refractive index could be responsible for the change in the sign of $\Delta R/R$ [19].

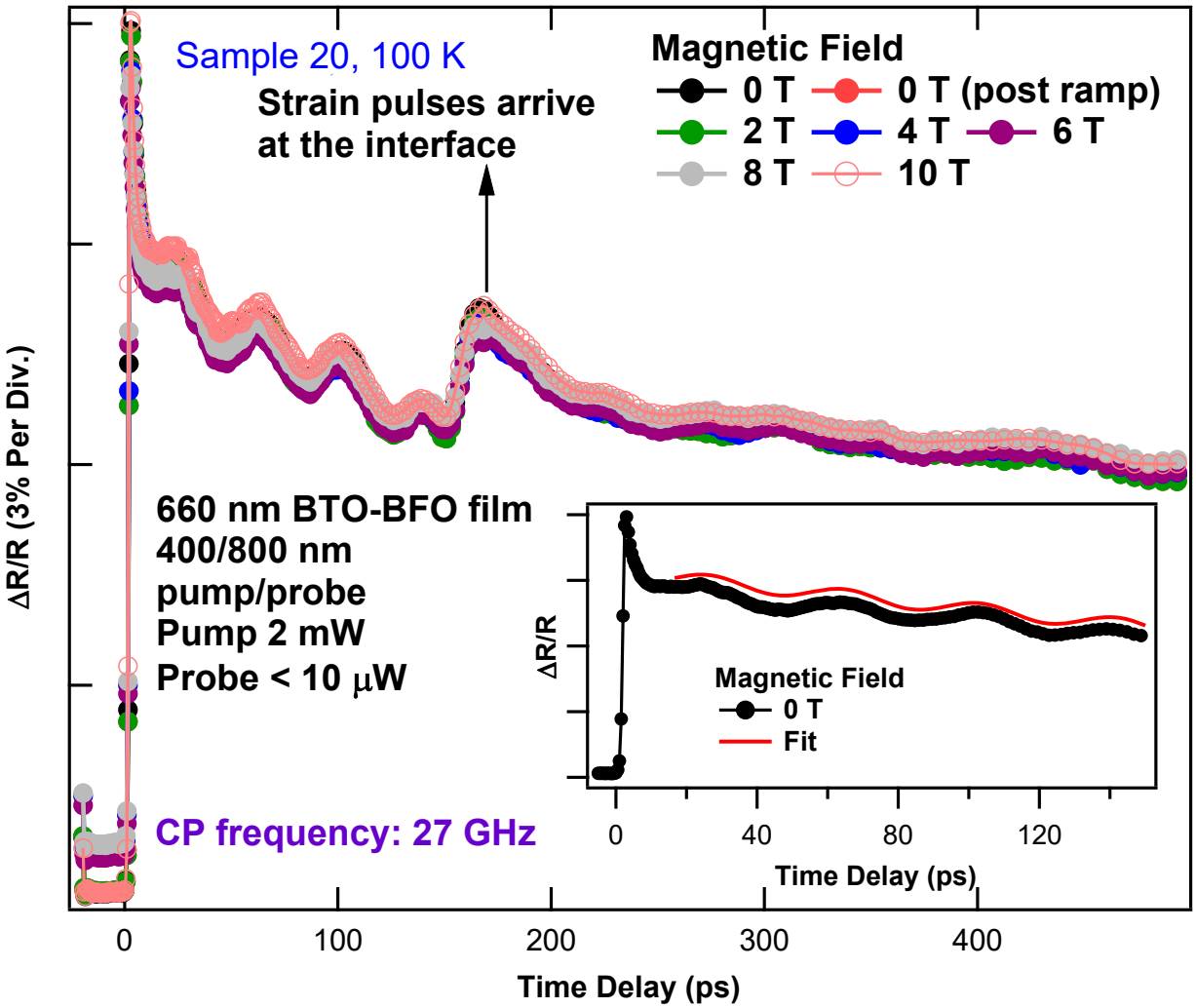

Figure 3.6: Transient reflectivity for sample 20 at 100 K for different external magnetic field. We were able to detect CPs, corresponding to an LA phonon frequency of $\sim$ 27 GHz. We observed no magnetic field dependence in the CP oscillations and the reproducibility of the observation at zero field, was confirmed by a post ramp trace, at the end. The feature at 170 ps represents the time for the strain pulses to reach to the interface. The inset shows the dynamics for the first 140 ps at zero magnetic field and the fit to the CP oscillations is to guide the eye. Note: The labels BTO-BFO refer to $BaTiO_3$-$BiFeO_3$ and the arrow shows the time that strain pulses arrive at the interface.

characteristic of coherent acoustic phonons (and also known as Brillouin oscillations). These types of oscillations have been observed in many systems including GaP layers grown on Si(001) [170]. All the data at 100 K was collected with a 400 nm pump at 2 mW power incident on the sample and 800 nm probe at less than 10 μW power. This result implies the 800 nm probe pulse can penetrate deep into the sample and detect the CPs as propagating strain pulses in the structure. Lowering temperature to reduce the damping of the phonon modes was also key to observing the CPs. [171, 172]. In this sample, we see a distinct bump in the signal at around 150 ps and the time is again consistent with the sound velocity in the $BaTiO_3$-$BiFeO_3$ in the range of 4.5-5.0 nm/ps. The bump arises when the acoustic phonon generated at the surface reaches the interface with the LSMO layer. We should note that the reflection of the strain pulses at the interface is negligible since the acoustic impedances between the $BaTiO_3$-$BiFeO_3$ and LSMO are similar.

The period of the Brillouin oscillation (for normal incidence) is given by $T = \lambda_{probe}/(2v_s n)$, where λ_{probe} is the wavelength of the probe light, v_s, the sound velocity and n, the refractive index. If we take the value of n =2.5, in between $BaTiO_3$ and $BiFeO_3$, this agrees well with the experimentally observed period. We note that we saw no such oscillation for the thinner $BaTiO_3$-$BiFeO_3$ film in Fig. 3.5, because the film thickness is too small. The acoustic pulse reaches the LSMO layer before oscillations can occur. As described earlier, the cycle of the Brillouin oscillation, 36 ps, implies that the acoustic pulse would leave the 80-nm thick $BaTiO_3$-$BiFeO_3$ film before half a cycle of the sinusoidal oscillation, making it difficult to be observed as a distinct oscillation.

The frequency of the observed Brillouin oscillation (27 GHz) in our $BaTiO_3$-$BiFeO_3$ is comparable with the thin films of $BiFeO_3$ on $LaAlO_3$ substrate studied by Doig *et al.* [20] but lower compared to the LA frequencies (ranging from 34-38 GHz) of $BiFeO_3$ single crystals studied by Ruello *et al.* [47] and Lejman *et al.* [169] where the same pump-probe wavelengths

(400/800 nm) as our experimental schemes were used.

3.3.3 Coherent Dynamics in $BaTiO_3$-$BiFeO_3$ Nanorods at Low Temperature

At a temperature of 100 K, using the same experimental conditions for the films, we observed complex dynamics, including CPs propagation along the long axis of the rods. In Fig. 3.7(a) we present the TRDR of $BaTiO_3$-$BiFeO_3$ nanorods taken at magnetic fields from $0-10$ T. The pump pulse was fixed at 400 nm with 2 mW of power and the probe at 800 nm with the power $\sim$ 10 μW. Similar to our results for the 660 nm thick $BaTiO_3$-$BiFeO_3$ film, we observe a sudden change in $\Delta R/R$ (a bump) at $\sim$ 120 ps time delay, when coherent longitudinal acoustic phonons generated at the surface of the $BaTiO_3$-$BiFeO_3$ nanorods reached the interface between the $BaTiO_3$-$BiFeO_3$ and the Pt. The time delay of the bump $\sim$ 120 ps (the time that the acoustic pulse entering the Pt layer) is again consistent with the propagation of a coherent acoustic phonon with a longitudinal sound velocity of 4.5-5.0 nm/ps. Focusing on Fig. 3.7(a), we observe two oscillation frequencies in the TRDR; the higher frequency oscillation (33 GHz), occurs only before the longitudinal acoustic mode encounters the interface and arises from the CP propagating in $BiFeO_3$ [20, 47, 166]. The lower frequency (8.1 GHz) in Fig. 3.7(b), is very close to that of a theoretically predicted magnon frequency expected for 800 nm probe in $BiFeO_3$ [20], where de Sousa *et al.* [173] by solving the Landau-Lifshitz equations, mapped the low frequency magneto-static spin wave dispersion for a $BiFeO_3$ film.

If this coherent oscillation is caused by the magnons, then it does not significantly increase in strength with magnetic fields [174]. In addition, this mode cannot be seen until after the coherent phonon travels from the surface, to reach the interface. Matching all traces at the

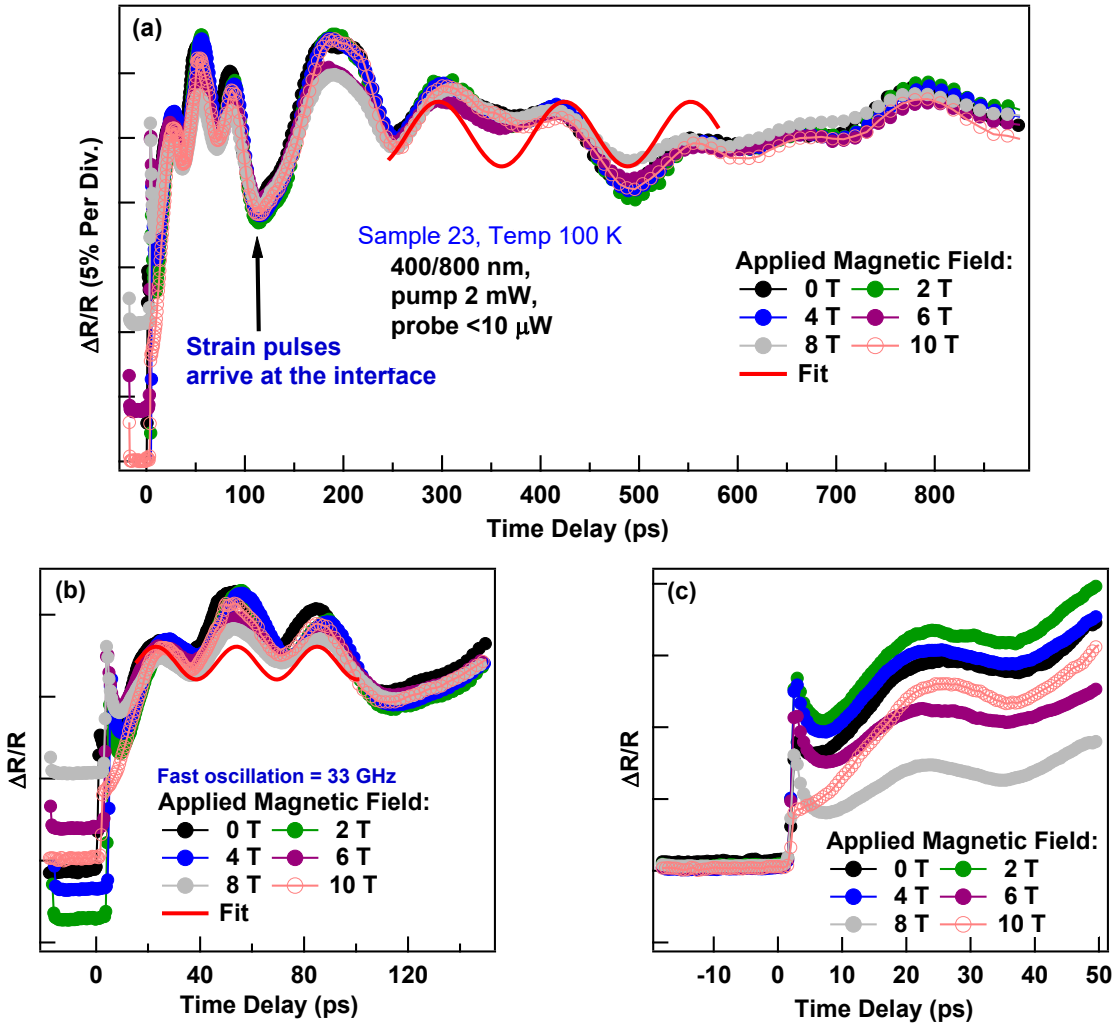

Figure 3.7: a) The magnetic field dependence of TRDR and CPs in nanorods (sample 23) at 100 K showing nearly periodic modulations at two different frequencies, 33 and 8.1 GHz. This lower frequency mode (8.1 GHz) is very close to the theoretically predicted magnon frequency [20]. Panels (a-c) show the same traces with different x ranges and y offsets. In panel (c) matching the traces at the negative delays and focusing on the first 50 ps, a weak magnetic field dependence was noted. The fits to the CP oscillations are shifted for clarity and are the guides to the eye. Note: The labels BTO-BFO refer to $BaTiO_3$-$BiFeO_3$ and the arrow shows the time that strain pulses arrive at the interface.

negative time delay in Fig. 3.7(c), we can see only a small variation in the observed TRDR as a function of magnetic field, for the first 50 ps of the dynamics.

Talbayev *et al.* showed the sensitivity of the rocking magnon mode frequency to external magnetic fields in $Ba_{0.6}Sr_{1.4}Zn_2Fe_{12}O_{22}$ (BSZFO) [175]; on the other hand, in an earlier study on $BiFeO_3$ by Doig *et al.* [20], no shift in the frequency of the magnon mode was observed by applying small magnetic fields (0.5 T) to unpin the AFM spin cycloid [20]. The static ME coupling in BFO is weak as the FE and AFM orders originate from different ions and the presence of spin cycloid does not allow for a linear ME effect but the presence of a strong magnetic field (20 T, expected in case of $BiFeO_3$) can suppress the cycloid, to establish a linear ME effect [92].

For a magnon in a simple AFM or FM an increase in frequency with applied magnetic field would be expected [174]. For example, in BSZFO at 0.1 T a distinct oscillatory response appears and further increase of the field leads to an increase in the oscillation period. At 1.2 T, in the collinear ferromagnetic phase, the oscillatory response changes and almost disappear at 2.5 T [175]. This fact demonstrates that magnon frequency can be sensitive to both the intensity of the external field and the fine details of the magnetization in the sample. In the case of our newly developed nanorods, more extensive studies are required to probe the interaction of the external magnetic fields and optically generated coherent oscillations.

We note that there is an interesting effect that might lead to a second possible origin of the slower oscillation. It could be related to the propagation of the strain pulses into the 100 nm thick Pt below the nanorods, as shown in Fig. 3.2(b). The propagation of the CP deep into the Pt layer can not be detected by the optical probe pulse since the probe pulse can not penetrate into the Pt owing to its large extinction coefficient at 800 nm (4.148) which is equivalent to an absorption depth of 15 nm, similar to most metals. However, the differential

reflectivity would be sensitive to the strain pulse at the interface. One possible explanation could be that the strain pulse in the 100 nm Pt layer is undergoing multiple reflections off of the Si substrate and coming back to the $BaTiO_3$-$BiFeO_3$/LSMO/Pt interface. This fact could result in a quasi-periodic modulation at the interface and lead to the observed oscillations in the differential reflectivity. It is also possible, that one is seeing reflections between the BTO/BFO -Pt layer and the surface or some combination of the two.

Why then did not we see reflections of the strain pulses in the previous samples? We note that for the previous samples, the $BaTiO_3$-$BiFeO_3$ was on LMSO and then on STO. The acoustic impedance $Z = \rho v_s$ (here ρ is the density and v_s is the sound velocity) for the layers is almost equal and hence, there is little acoustic reflection from the interfaces. For $BaTiO_3$-$BiFeO_3$ we estimate an acoustic impedance Z = 38 (in units of g/cm^3 nm/ps) based on densities of $BiFeO_3$, $\rho = 9.15$ g/cm^3 and $BaTiO_3$, $\rho = 6.02$ g/cm^3, taking a weighted average (0.75 to 0.25), using a sound velocity 4.5 nm/ps. For LSMO, the acoustic impedance is Z=42 (using $\rho = 6.5$ g/cm^3 and a sound velocity 6.5 nm/ps.) For STO, we find Z = 40 (using $\rho = 5.11$ g/cm^3 and $V_s = 7.8$ nm/ps. Since the acoustic impedances are nearly equal, we find little reflection at the interfaces, (less than 1%).

However, for the nanorod samples, which are on a Pt layer, the density of Pt is much larger than Si (and also the $BaTiO_3$-$BiFeO_3$ density) and leads to a large acoustic mismatch at the interface. For instance, for the longitudinal modes, the acoustic impedance for Pt is 85 g/cm^2-sec $\times$ 10^5 compared to that for Si which is 20 g/cm^2-sec $\times 10^5$. As a result, the reflectivity at the Si-Pt interface represented as: $R = \left|\frac{Z_{Pt}-Z_{Si}}{Z_{Pt}+Z_{Si}}\right|^2$, is about 0.4. It is possible that one is getting multiple reflections in the Pt layer at the two interfaces (or possible from the first interface and the surface). If this were the case, one would get pulses at a frequency given by: $f = v_{Pt}/200$ nm. Since the initial strain generated by the photoexcited carriers at the surface is fairly wide (two times the 30-45 nm absorption depth, which is

significant compared to the width of the Pt layer, the "echo" pulses will be fairly broad. For a longitudinal sound mode in Pt (with velocity 3.96 nm/ps) this would correspond to a come-back time of 51 ps corresponding to a frequency of 19.8 GHz. This seems a bit too slow to explain the features. However, it is interesting to note that for the Transverse Acoustic (TA) mode in Pt, this would correspond to a return time of 120 ps corresponding to a frequency of 8.35 GHz, very close to the observed frequency in this work. In a single crystal of $BiFeO_3$ for one of the grain sizes, Lejman *et al.* reported a TA frequency of ~ 10 GHz [169].

How would one generate the TA mode in the Pt system? We conjecture that since the nanorods do not cover the entire Pt interface, when the LA modes in the nanorods reach at the interface, they can excite TA modes through the non-uniform longitudinal strain at the surface which gives rise to a shear strain. That is, there is a net shear strain at the interface which could be responsible for generating the TA modes. While both the magnon and reflecting TA phonon mode in Pt are intriguing explanations for the observation of the 8.1 GHz feature, it is clear that additional studies will be needed to more accurately elucidate and verify the origin of this feature.

Strongly coupled magnon–phonon dynamics within a single thin nickel nanomagnet has been observed recently, in which a hybridized magnon–phonon quasiparticle was formed. This hybridization can be presented as not having a magnon or phonon character, but rather exist in both states where the avoided crossing between these two states can result in a two-level state with possible Rabi oscillations between the two states [74].

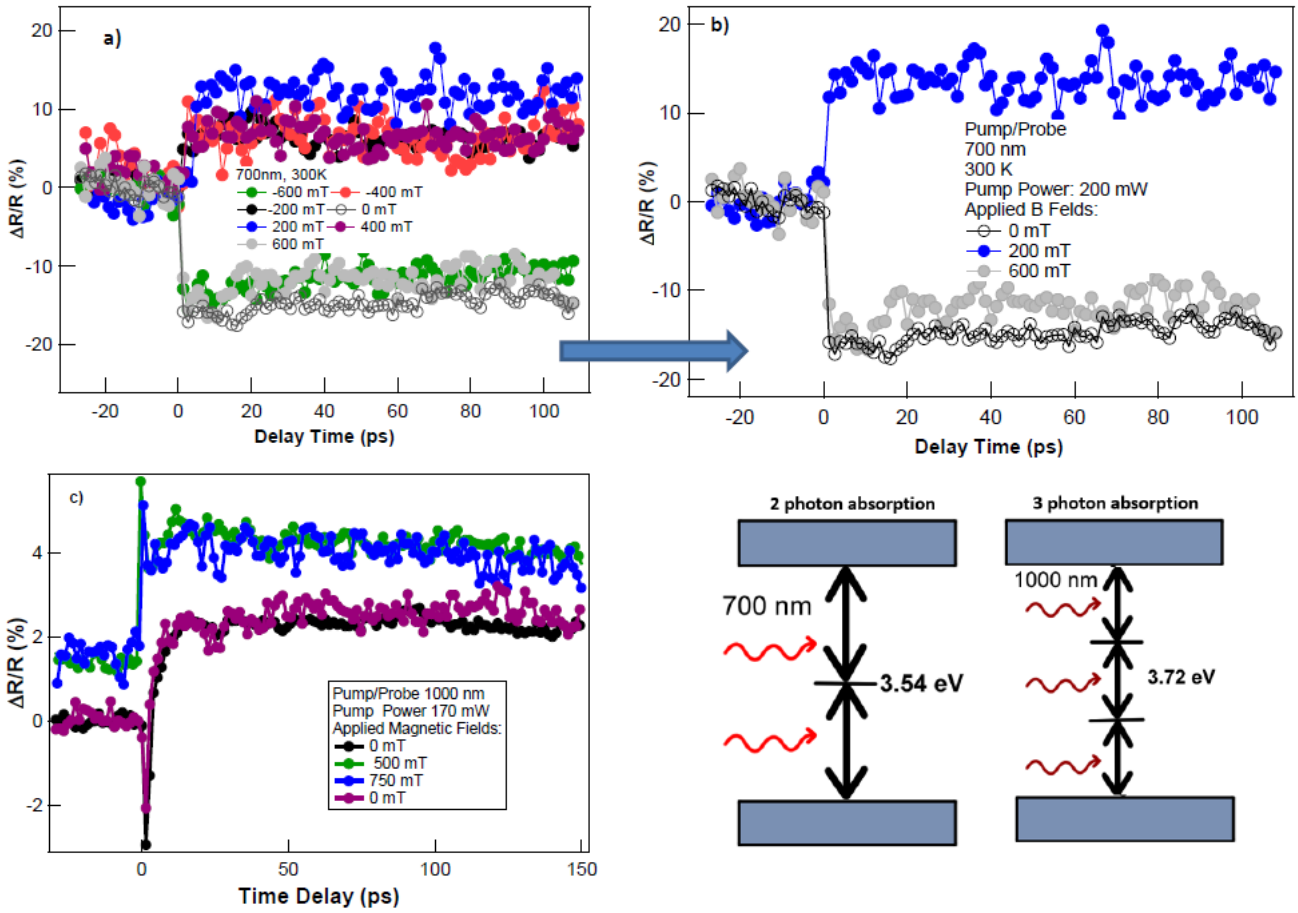

Figure 3.8: TRDR at 700 nm for sample 23, (a) Sensitivity to the external magnetic felds. The measurements were started from -600 mT and ended at +600 mT. The magnitude of TRDR is a factor of 10 larger in this scheme. (b) A smaller subset of the observation in panel (a). (c) TRDR at 1000 nm for sample 23 with smaller amplitude but with a similar sensitivity to external magnetic felds at 700 nm. The signal recovers after increasing the field from zero to 750 mT and come back to zero field.

3.3.4 Carrier Relaxation Dynamics in $BaTiO_3$-$BiFeO_3$ Nanorods Using a Degenerate Pump-Probe Scheme

In this section, I will be discussing additional set of measurements we conducted at room temperature, on BTO-BFO nanorod structures using a degenerate pump-probe scheme. These are unpublished and preliminary results which should be pursued further. Here, we have probed magnetic field dependence measurements with multiple NIR wavelengths, where we expected to observe multiphoton absorption. The light source for the TRDR was a Coherent Chameleon Ti: sapphire laser system with 100 fs laser pulses with a wavelength range of 700-1050 nm and a repetition rate of 80 MHz. The laser beam was split into pump and probe beams using a beam splitter. Similar to the non-degenerate setup the pump pulses were delayed respect to probe using a tunable delay line and the pump beam was modulated using a mechanical chopper with a frequency of 1 kHz. Both the pump and the probe beams were focused on the sample using lenses, where the spot diameter of the pump was 150-200 μm with a pump fluence of 6.76 μJ/cm^2 and the probe beam with a lower fluence. The sample was mounted inside an electromagnet with a magnetic field range of 0-1 T. The reflected probe beam was monitered via a Si detector which was fed into a lock-in amplifier.

As shown in Fig. 3.8(a), TRDR was observed in nanorods, and unlike the films, showed sensitivity to external magnetic fields. In Fig. 3.8(b) we show the observation for three different cases. The pump pulses had a spot size of $150 - 200$ μm exciting multiple rods and the substrate did not show any TRDR responses. At 700 nm (1.77 eV), it requires at least two photons to excite a charge carrier into the conduction band via an intermediate state as we are not close to the expected bandgaps of this material system ($\sim$ 3 eV). The observed TRDR could be related to a nonlinear process with the optical field resulting in simultaneous absorption of two or more photons as shown in the schematic illustration in

Fig. 3.8(d). The amplitude of the TRDR is 10 times larger than the observed TRDR films where the excitation wavelength was at 400 nm. In addition, the tunability of the TRDR to the external magnetic films suggests that the magnetic coupling could be stronger in a lower dimensional system. At 1000 nm (1.24 eV), it requires at least three photons process to excite charge carriers into the conduction band via an intermediate state. We should note that the amplitude of the TRDR, in the three photon process, is much smaller compared to the case with the pump at 700 nm during a two-photon absorption process.

3.4 Conclusions

We have studied the dynamical properties of a variety of BTO-BFO films and nanorods using ultrafast TRDR spectroscopy. Adding $BaTiO_3$ to $BiFeO_3$ can reduce the conductivity of the mixture and improve the multiferroic behavior. This is an interesting lead-free system, and our ultrafast optical measurements of these less explored systems [9] can provide insights to employ these complex materials for applications such as optical switching in multiferroics.

One of the main features, was the detection of CAPs in these BTO-BFO structures where, coherent phonons were generated near the surface using 400 nm pump pulses. We observed a clear sinusoidal modulation in the transient reflectivity, a characteristic of CAPs (known as Brillouin oscillations). Our time resolved measurements can be used to probe dynamical properties on picosecond time scales and the information obtained is vital towards the design and understanding of high speed devices that incorporate multifunctional materials.

While CPs are typically used to provide detailed spectroscopy information and characterize surfaces and buried interfaces [170], it has recently been demonstrated that dynamical strains in Surface Acoustic Wave (SAW) devices can interact with spins in SiC [176]. This suggests that our approach of employing ultrafast optical generation of the strain offers a

potentially better means of generating the dynamic strain that can bypass the need to fabricate a SAW device and allow for higher frequencies and faster manipulation. For future applications, the ability to generate strain via ultrafast optics offers the intriguing possibility of dynamically manipulating the strain, opening the possibility of creating a new class of devices. In this fashion, the strain is manipulated in time and one can generate and control the photo-generated CPs to ultimately control electric, magnetic and strain fields leading to revolutionary new devices [177, 178, 179, 180]. Furthermore, a material system where the ME coupling can be enhanced could be a powerful method for tuning coherent modes such as magnons.

Chapter 4

Probing Sensitivity of Longitudinal Coherent Acoustic Phonons to External Magnetic Fields in $BaTiO_3$-$BiFeO_3$

Earlier, I have discussed the probe of coherent acoustic phonon oscillations in BTO-BFO films and nanorods using transient reflectivity measurements. The approach presented in this chapter is a complementary approach to the measurements in Chapter 3. Here, we focused on probing optical properties of $BaTiO_3$-$BiFeO_3$ by employing transient birefringence and magneto-optical Kerr effect. Employing these measurements, we were able to demonstrate the magnetic field dependence of coherent phonons. We have also probed the second harmonic generation in BTO-BFO film structures to study the underlying symmetries of these structures. I made the measurements on available BTO-BFO to characterize the best possible structure for the MOKE and OIB measurements. I contributed to this work by conducting the SHG measurements of BTO-BFO structures. Here, I have conducted both wavelength dependence and incident polarization dependence measurements. I also wrote a large portion of

the experimental sections.

4.1 Introduction

In this study we focused on probing BTO-BFO via Time Resolved Optically Induced Birefringence (TROIB) and Time Resolved Magneto-Optical Kerr Effect (TRMOKE). These techniques allowed us to probe the dynamics of the non-linear and magneto-optical properties of BTO-BFO. The high speed electro-optical properties of this material are of current interest as BTO-BFO has potential to be used in high speed electro-optic modulators (EOM) [181, 182]. EOM are devices that are of fundamental importance to the telecommunications industry and currently $LiNbO_3$ single crystals are utilized in electro-optic applications, but interest has been growing in thin film EOM devices employing BTO [183] or BFO [161]. In addition, TROIB has the advantage of being able to generate coherent phonons when pumping below the band energy allowing us to potentially explore a greater variety of coherent phenomena in our sample [184]. The dynamical magneto-electric (ME) coupling is also of interest if we want to couple to the magnon spectrum of these materials. Our results and choice of materials system could provide new opportunities in this direction.

Furthermore, TROIB and TRMOKE as a function of magnetic fields can allow us to explore signatures of ME coupling in optical frequency limit. Recent Raman [185, 186] and optical second harmonic generation (SHG) [187, 188, 189, 190] studies suggest the possibility of strong ME coupling in $BiFeO_3$. One promising way to enhance the ME coupling of $BiFeO_3$ is by designing compositions close to the phase transition regime such as the morphotropic phase boundary (MPB). Recent investigations on BTO-BFO compositions near MPB show the emergence of strong ME coupling [167, 191, 192, 193, 194, 195]. The enhancement of magnetic properties with decreasing $BiFeO_3$ mole fraction, from 0.775 to 0.750, was attributed to

active spin modulation of ordered Fe-O-Fe [196, 197]. It was found that the substitution of large Ba^{2+} and Ti^{4+} ions on the A^{-} and B^{-} sites respectively enlarges the distortion of bond angle of Fe-O-Fe to release the spiral magnetic modulation. This material was found to be rhombohedral, on average, with local monoclinic distortions/symmetry [2, 196], indicating the possibility of polarization enhancement through the presence of intermediate bridging phases. Our magnetic field dependence measurements in this work demonstrate new insights on how the coherent time resolved dynamics in this material system can interact with external magnetic fields.

4.2 Samples Characteristics

In this study we probed TROIB, TRMOKE, as well as SHG in two BTO-BFO epitaxial films grown on $La_{0.67}Sr_{0.33}MnO_3$ (LSMO) with STO substrate (sample 8, sample 20). The details of the growth are described in Chapter 3 [2] and the characteristics of the samples investigated in this chapter, are summarized in Table 4.1. These two structures were probed earlier where the carrier dynamics and coherent phonon (CP) generations were characterized under the exact same experimental conditions as in this study [2]. Our observations of TROIB and TRMOKE might suggest that the sensitivity of CPs to the external magnetic fields could be probed or affected more significantly using these methods compared to time resolved differential reflectively (TRDR) reported earlier [2].

Table 4.1: The samples studied in this work. The thicknesses refer to the BTO-BFO layers and LSMO layers.

Sample	Thickness LSMO (nm)	Thickness BTO-BFO (nm)	STO Orientation	Structure
8	40	80	(001)	BTO-BFO/LSMO/STO
20	100	660	(001)	BTO-BFO/LSMO/STO

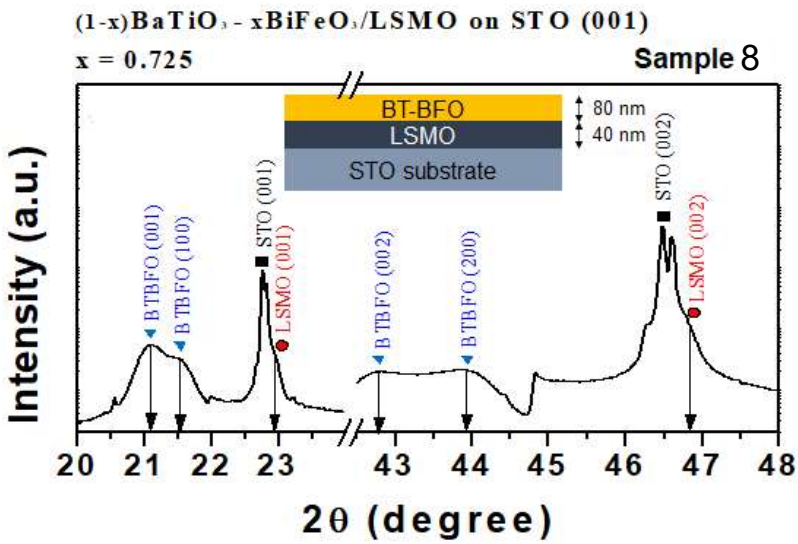

Figure 4.1: Here we present an example of x-ray diffraction for the sample 8, displaying the single phase nature of our BTO-BFO films.

Here we present some basic characteristics of the two samples before introducing the dynamical aspects. As an example in Fig. 4.1(a), we present the crystal structure of one of the BTO-BFO/LSMO films grown on STO substrates (sample 8) and the x-ray measurement of the sample 20 was presented in Chapter 3 [2]. As was confirmed through the x-ray diffraction (XRD) analysis, these samples were epitaxially grown along the c-axis of the STO substrate without any secondary phases.

4.3 Results and Discussions

4.3.1 TROIB and TRMOKE Measurements of BTO-BFO Films

In this study, we report the TROIB observed by measuring the evolution of the polarization

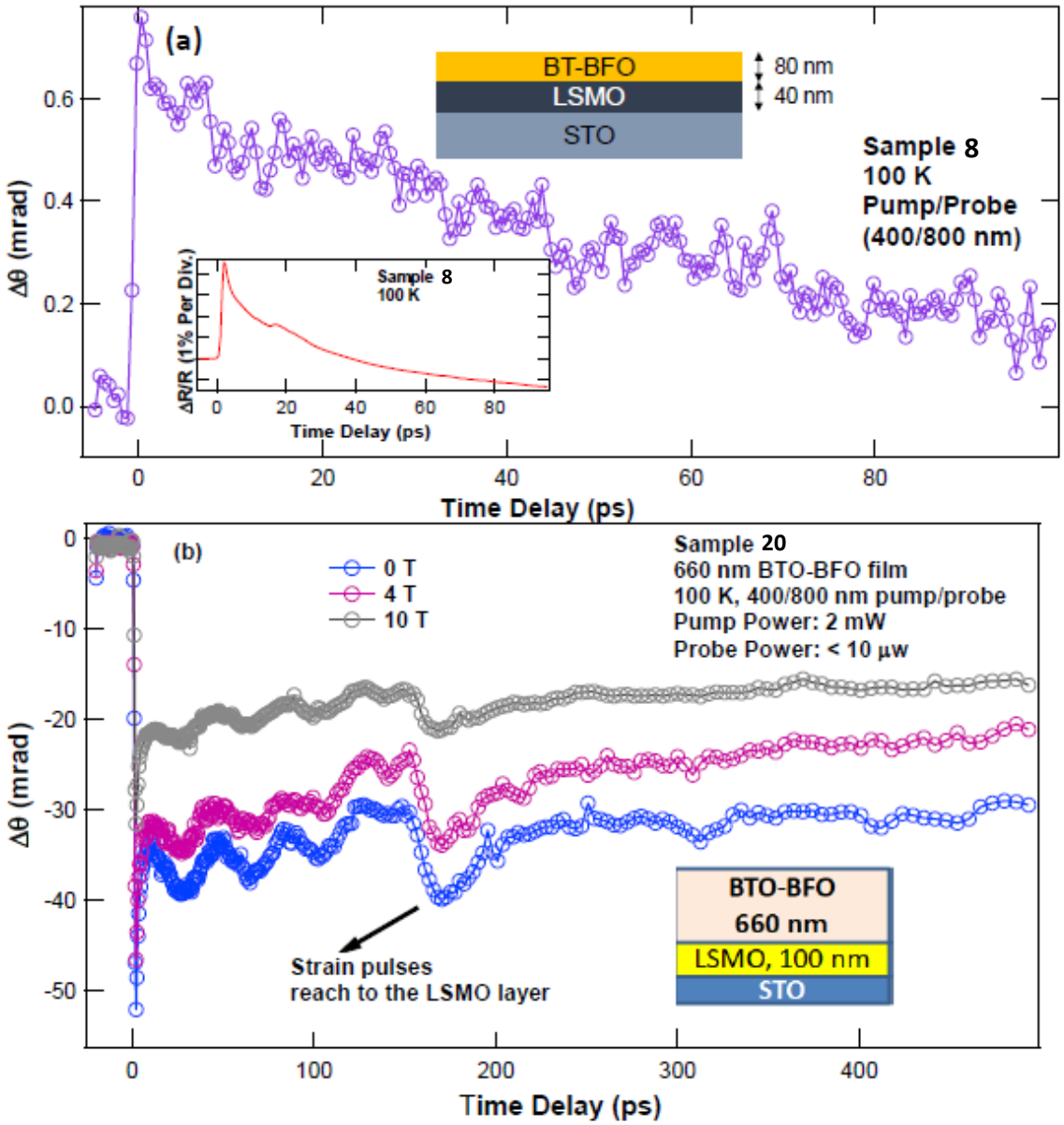

Figure 4.2: (a) The TROIB response of sample 8 with pump-probe of 400/800 nm at 100 K. The inset shows the transient reflectivity at the same temperature and experimental condition. (b) The TROIB detected in sample 20 at 100 K, clearly shows the CLAPs and the sensitivity to the external magnetic fields.

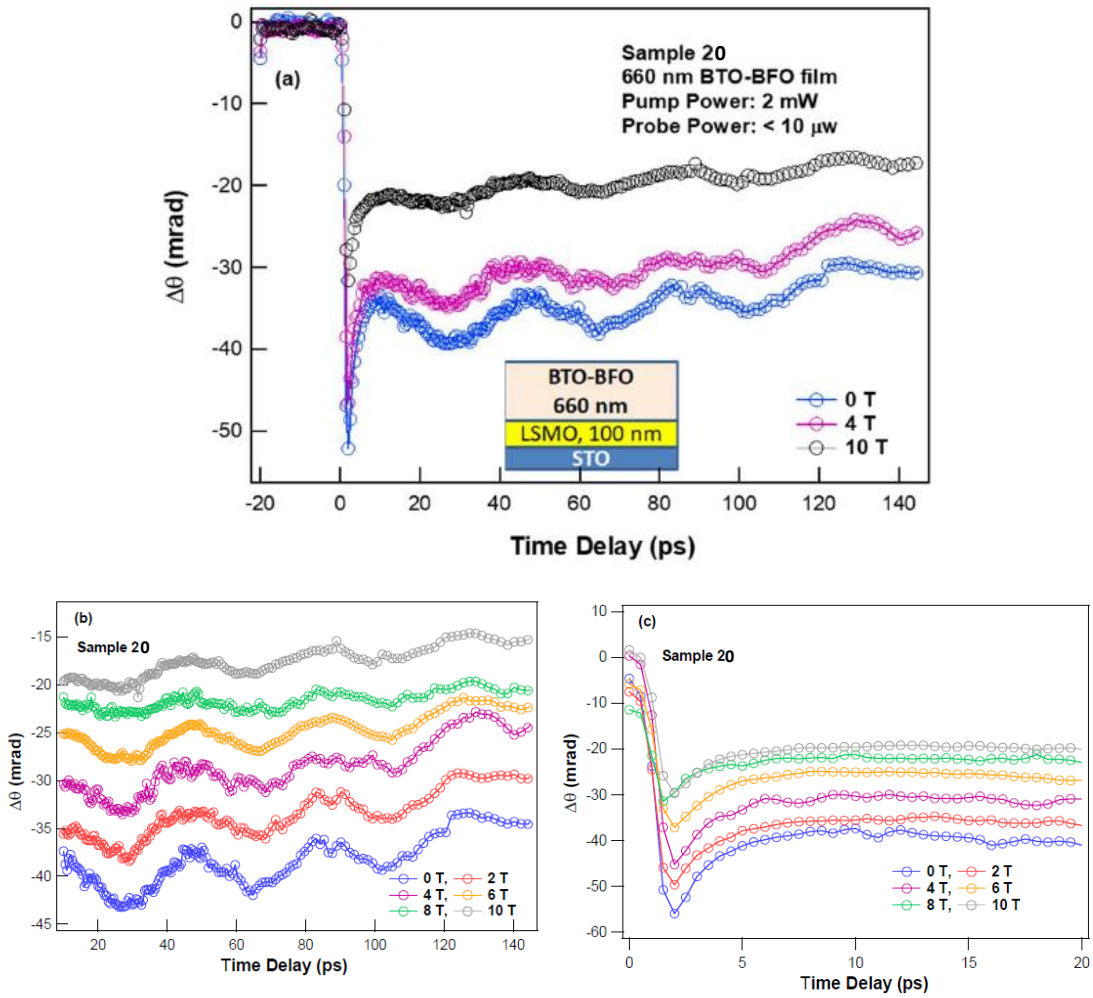

Figure 4.3: (a) Focusing on the first 140 ps of the TROIB for 3 different magnetic fields we can see both the amplitude of $\Delta\theta$ and the strength of CPs are affected by the field's strength. (b) The evolution of CPs' amplitude by increasing the magnetic field. We expect the magnetic field modifies the bandgap and alter the absorption strength of the pump pulses reducing the amplitude of the CPs. (c) Focusing on the first 20 ps one can see the amplitude of $\Delta\theta$ reduces by increasing the external magnetic field.

shift ($\Delta\theta$) of the reflected probe beam [198]. In this process the laser source was a coherent amplified Ti:sapphire oscillator with a repetition rate of 1 kHz, a wavelength of 800 nm, and a pulse duration of $\sim$ 100 fs, with $\sim$1 W output power. We used 90% of the oscillator's output power to frequency double to 400 nm using a 0.5 mm thick BBO crystal and generated 2 mW of power with an estimated fluence of 4 mJ cm^{-2}. The pump pulses were modulated by a chopper at 211 Hz. The probe pulses were attenuated to $\sim$10 μW, corresponding to a fluence of 30 μJ cm^{-2}. For the OIB measurements, the reflected probe pulses from the sample were directed through a Wollaston prism to separate the S and P polarizations. Balanced photodiode detection was used to measure the differences between the S and P polarizations as a function of the time delay between the pump and probe pulses. The changes in the polarization of the reflected probe pulse ($\Delta\theta$) as a function of the time delay was mapped.

Figure 4.2(a) shows the TROIB at 100 K in sample 8 by probing the changes in the polarization of the reflected probe pulses (800 nm) with the pump pulses at 400 nm. The estimated absorption length for 400 nm pump pulses is in the range of 35-45 nm and the 800 nm probe pulses with the absorption length of ($\sim$ 1 μm) allowing us to probe the dynamics in the entire sample's volume. The birefringence amplitude in the sample 20, as shown in Fig. 4.2 (b) is much larger than that of sample 8.

These measurements were performed under the exact experimental conditions, as earlier reports on these two films, where the focus was probing CPs and carrier dynamics. Previously, by employing transient reflectivity, we reported clear signatures of CPs in the sample 20 and monitored the magnetic dependence from zero to 10 T [2]. Here, in the process of measuring the OIB and MOKE, in the case of the sample 20 with 660 nm BTO-BFO thickness, CPs were also detected (Fig. 4.2 (b)). The energy of the incoming pump pulses with 100 fs duration was incident on the BTO-BFO film over an area (150-200 μm pump beam diameter) generating Coherent Longitudinal Acoustic Phonons (CLAPs) [2]. The below-gap (800 nm)

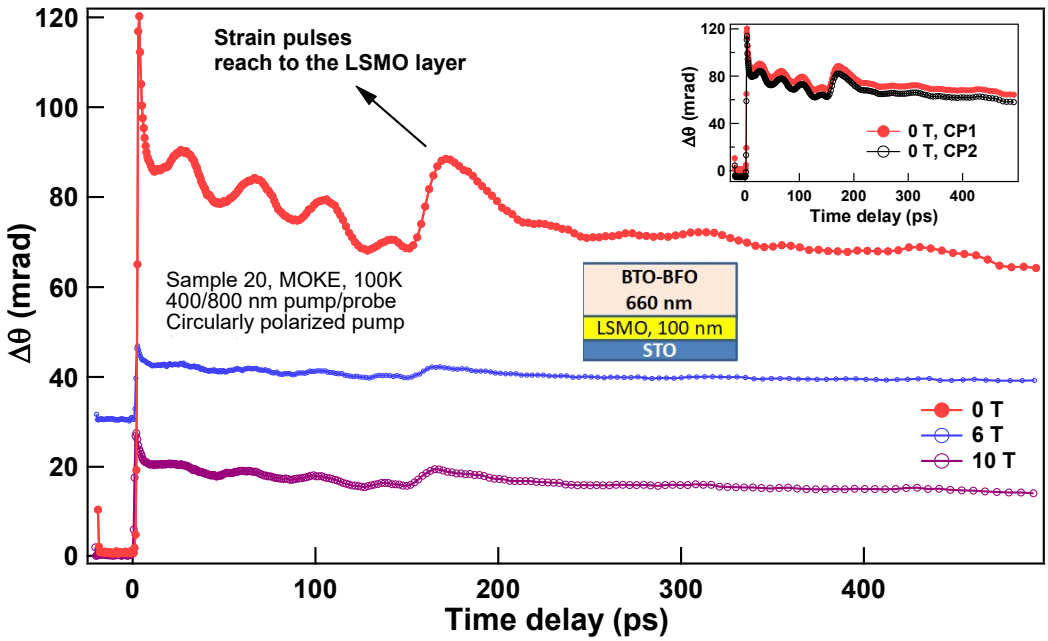

Figure 4.4: (a) TRMOKE at 100 K with the pump pulses at 400 nm being circularly polarized. The over all feature of the CP dynamics including the frequency and the arrival time at the interface remained mainly similar to the OIB measurements and by increasing magnetic field both the amplitude of the MOKE signal as well as the CPs' strength decreased. The traces are shifted for clarity. The inset compares two traces for two different circular polarizations and are shifted slightly for clarity. As shown in this inset, we did not observe any differences when the pump circular polarization was switched between left and right.

probe pulses reflect off the whole excitation volume, creating a strong oscillation, known as Brillouin oscillations. As identified in Fig. 4.2 (b), the bump at 170 ps is when the strain pulses reach to the BTO-BFO interface, after the propagation of the CLAPs generated at the surface using the 400 nm pump pulses, reaching the interface between the BTO-BFO and the LSMO. This feature is consistent when the transient reflectivity that was measured under the same experimental conditions and the observed CLAPs frequency of $\sim$ 27 GHz extracted in this measurement is the same as we reported earlier, using transient reflectivity measurements, and similarly we attribute these oscillations to CLAPs [2].

Focusing on the first 140 ps for three different magnetic fields, as presented in Fig. 4.3 (b), we observed sensitivity of CLAPs' amplitudes to the external magnetic field. These measurements were performed exactly under the sample experimental conditions of previously reported CLAPs [2]. In contrast to the previous study, in Chapter 3 [2], the CLAPs detected in this case using TROIB scheme demonstrated sensitivity to magnetic fields. In Fig. 4.3 (b) we display the evolution of the CLAPs' amplitudes, where the significant decrease can be observed at 8 and 10 T.

Furthermore, under the same experimental condition as our TROIB, we probed TRMOKE with circularly polarized pump pulses (Fig. 4.4). Similarly, the amplitude of the Kerr rotation ($\Delta\Theta$) and the CLAPs decrease by increasing the magnetic field. It is known that the static ME coupling in $BiFeO_3$ can be suppressed where the ferroelectric (FE) and antiferromagnetic (AFM) orders originate from different ions. In the presence of spin cycloid a linear ME could be weak and applying a strong magnetic field, larger than 20 T in case of $BiFeO_3$, was predicted to establish a linear ME effect by suppressing the cycloid orders [92]. Our observations presented here show that the ME in BTO-BFO could be tuned in more moderated magnetic fields.

As an additional approach to probe the non-linear properties of BTO-BFO, we explored the second harmonic generation (SHG) in these films. SHG is the lowest order nonlinear process where incoming photons interact with a nonlinear media and emit light with twice the energy of the initial. SHG can be generated in structures where the inversion symmetry is broken. Thus, it is commonly observed in non-centrosymmetric media, at the surfaces and interfaces of material structures, and magnetically ordered materials [27, 28, 29, 30, 31, 32, 110, 127, 135, 136].

4.3.2 SHG in BTO-BFO Films

As discussed in section (2.2) nonlinear optical techniques are powerful tools to understand the underlying electronic and magnetic structure of materials by probing light-matter interactions. In nonlinear optical media, induced polarization *P(t)* can be expanded in terms of external electric field $E(t)$ as follows [124].

$$P(t) = P_0 + \varepsilon_0 \chi_e E(t) + \chi^{(2)} E(t)^2 + \chi^{(3)} E(t)^3 + ..., \tag{4.1}$$

where P_0 denotes a constant polarization, χ_e is the linear susceptibility, and $\chi^{(2)}$,$\chi^{(3)}$ are higher order susceptibility terms. Thus, the second term describes linear optical properties and the higher order terms give rise to nonlinear optical properties such as SHG. Moreover, the dielectric properties of a material are a result of these higher order susceptibility terms. For an example, optically induced birefringence (OIB), where an artificial optical axis is induced by an extant electric field in the sample or by an externally applied electric field, is a consequence of these higher order terms [198].

In a magnetically ordered material, the second-order nonlinear electric susceptibility has both structural and magnetic order parameter contributions: a time-invariant component with a crystallographic contribution and a time-variant component with a linear spin-dependent contribution. Therefore, SHG is a vital tool to study underlying electric and magnetic symmetries in multiferroic materials [198]. Bulk $BifeO_3$(BFO) has a rhombohedral distorted Perovskite structure in the space group R3c, which permits both for the FE atomic displacement and AFM G-type spin configuration. Due to strain associated with lattice mismatch and different thermal expansion coefficients of different substrates, both rhombohedral and tetragonal BFO have been reported. SHG has been used to understand the structural and magnetic properties of BFO [185, 187, 188, 189, 199].

Wang *et al.* [199] conducted a polarization dependence SHG measurement on BFO in a reflection geometry. They reported the structural symmetry of the BFO changes from tetragonal to rhombohedral with increasing thickness [199]. The authors have also reported, the SHG observation of non-zero minimum for thicker BFO films due to the overlapping of SHG signal generated from rhombohedral and tetragonal phase domains. [199]. In another study, Kumar *et al.* [200] employed SHG measurements to distinguish tetragonal and rhombohedral distortions in mixed phase strained BFO films. They have observed a double lobed configuration which authors have attributed to a combination of the monoclinic point group symmetry in BFO of each phase [200].

Most of the SHG studies have been conducted on either single crystal systems or nearly single crystal structures, to determine the crystal symmetry of BFO. However, hetero-epitaxial systems increase the complexity while determining the symmetry point groups of the material structure. This is due to the fact that in multi-domain systems the observed SHG intensity could be either the intensity related to the net polarization of the domain pattern, or the collective intensity of each contributing domain state [201]. In our previous study, both far-field and near-field SHG imaging were reported in a polycrystalline BTO-BFO. In this study, distinct ferroelectric domain contrast was observed in near-field SHG imaging. Additionally, the observed results were associated to optically driven polling in BTO-BFO thin films [198].

For our SHG studies, we probed the wavelength dependence (850-1050 nm) and polarization dependence ($0^0 - 360^0$) of the SHG response of the sample 8 and the results are presented here. The laser source was a Coherent Chameleon Ti:sapphire laser with a repetition rate of 80 MHz, a wavelength range of 700-1050 nm, and a pulse duration of 100 fs. The SHG was measured using the iHR550 spectrometer with a LN_2 cooled Symphony II CCD detector. In the polarization dependent measurements, the incident polarization was varied via a Thorlabs Half-Wave Liquid Crystal Variable Retarder/Wave Plate (Thorlabs; LCC1221-B).

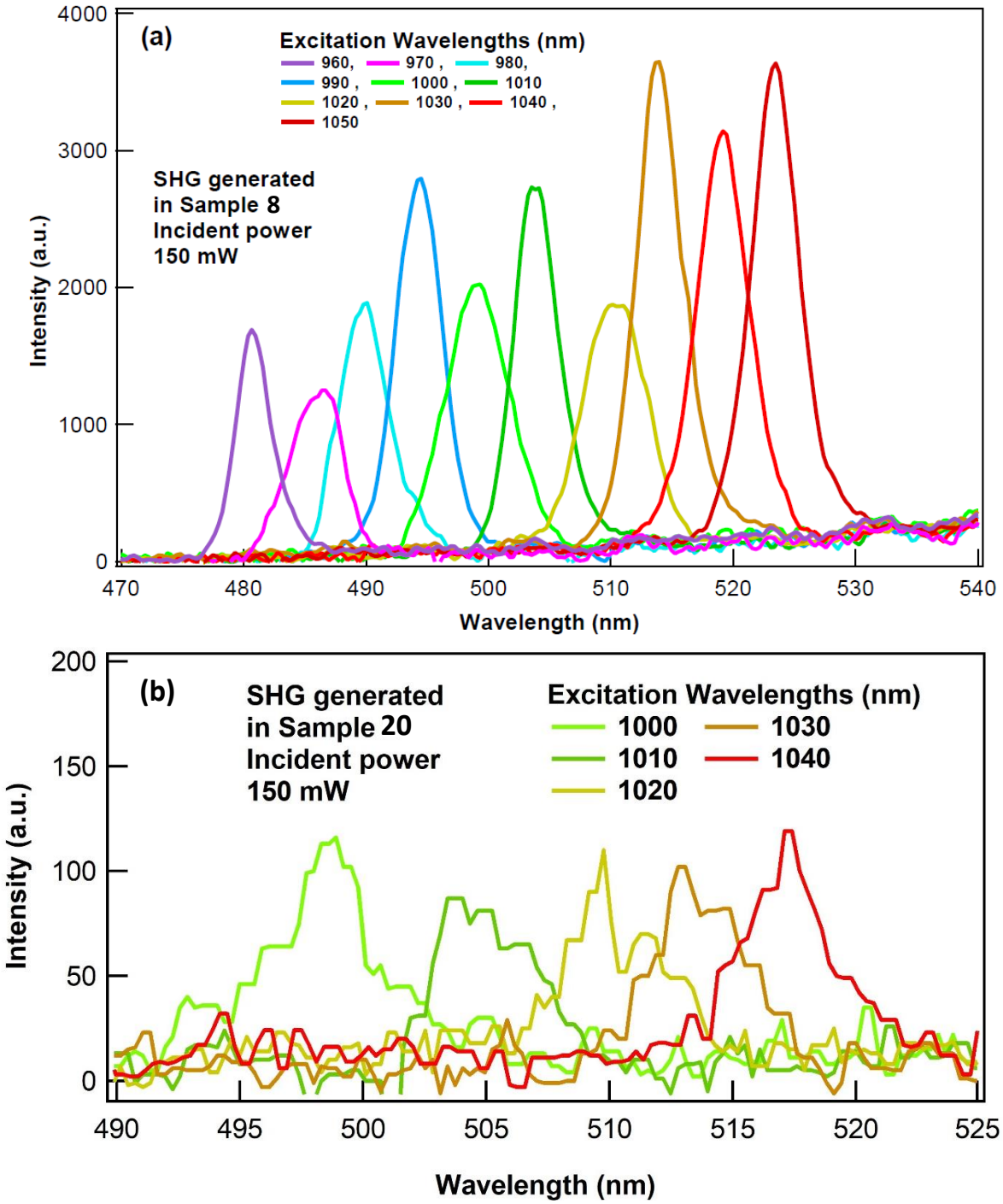

Figure 4.5: SHG in (a) sample 8 and (b) sample 20 intensity distribution of incident wavelength with 150 mW incident power at room temperature with 120 s exposure time.

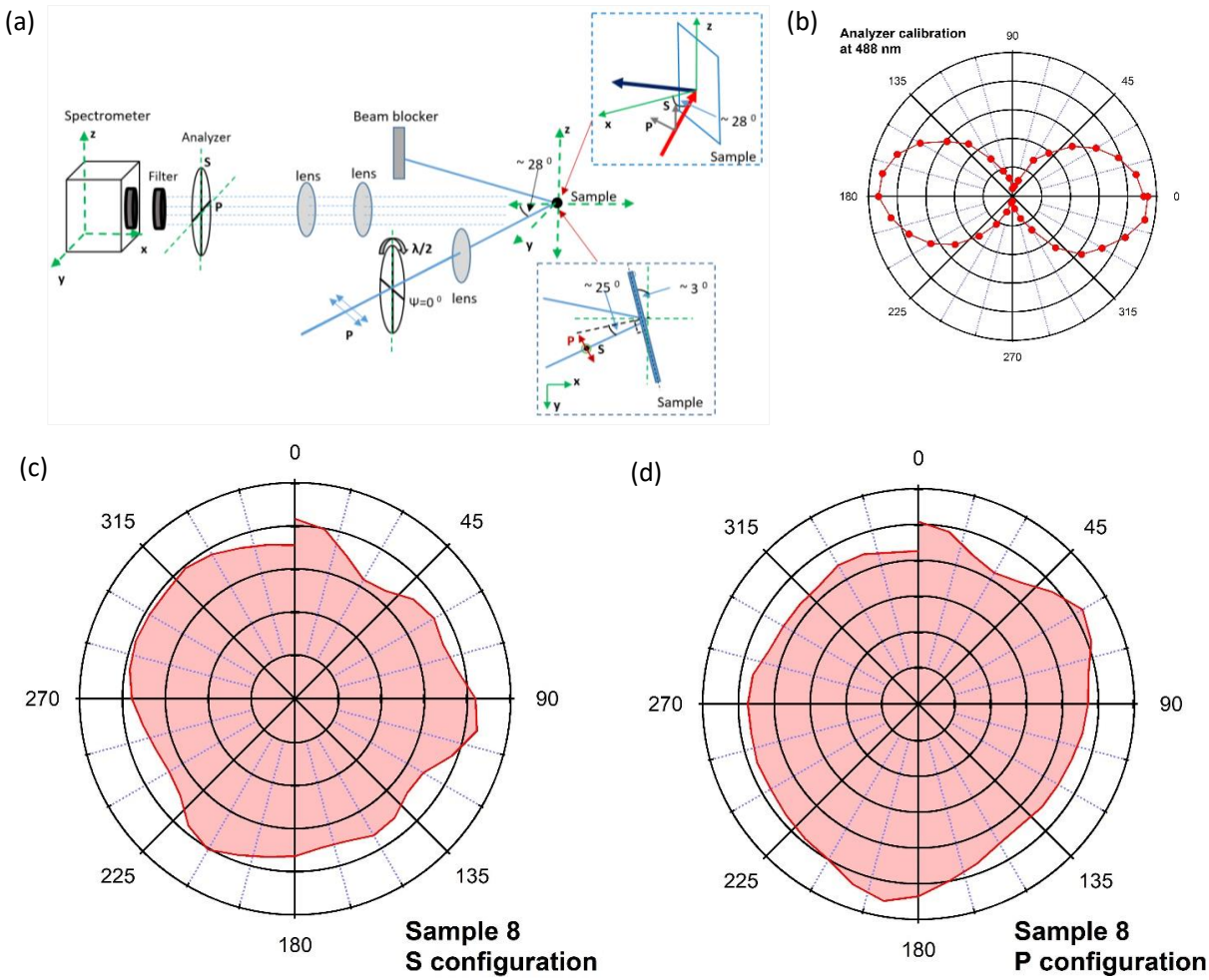

Figure 4.6: (a) Schematic diagram of the SHG incident polarization setup. (b) Testing the analyzer sensitivity to polarization with a laser at 488 nm. We used this wavelength as the SHG in the nanorods are close to this range.The incident polarization dependence of SHG in the sample 8 at 980 nm using an analyzer on the emission path. (c),(d) analyzer configuration for S and P respectively.

The SHG measurements were taken with two analyzer configurations, S and P, where S is referring to the polarization perpendicular to the plane of incidence beam and P is for the polarization parallel to the plane of incidence. SHG measurements were performed on both the 80 nm thick BTO-BFO thin film structure (sample 8) and 660 nm thick BTO-BFO film structure (sample 20). As we reported in our previous study these films were grown with rhombohedral phase [2, 196]. Figure 4.5 displays the SHG measurements taken for different incident wavelengths in the 950-1050 nm range. As presented in Fig. 4.5 sample 8 has a better SHG intensity compared to the sample 20.

These measurements were taken at room temperature with 150 mW of the laser power while varying the incident wavelength. Here we have setup the spectrometer to have a 0.15 mm slit size and a 120 sec exposure time. In Fig. 4.5, we can observe the corresponding SHG peaks demonstrating that the frequency is doubled at each incident wavelength. Moreover, we can observe a random intensity variation in each signal with respect to the different incident wavelengths. However, we observe a gradual increase in the SHG intensity with the increasing incident wavelength. The maximum SHG intensity occurs at 525 nm (with 1050 nm incident light) and the minimum intensity is at 485 nm (with 970 nm incident light).

Different intensities of the observed SHG peak may occur due to a variety of reasons. Here we can consider two main reasons: (1) properties of incident light such as incident intensity and the frequency, (2) properties of the material such as nonlinear coefficients which is directly related to the point group symmetry of the material, refractive index profile and coherence length [202]. The SHG intensity is proportional to the square (${I_w}^2$) of the intensity of the incident beam, considering the incident beam transmit through the material without attenuating. In this study, we maintained constant incident intensity while changing the incident wavelength.

Another requirement for efficient SHG conversion is satisfying the phase matching condition.

That is the refractive index of the material at ω (incident beam frequency) and 2ω (SHG frequency) should be equal (discussed in section 1.2.1). In general, there exists a refractive index dispersion in materials resulting in phase mismatch lowering the SHG efficiency. This phase matching condition can be quite complicated in birefringent materials as the refractive index is anisotropic. This could lead to discrepancies in the SHG intensity with their incident wavelength dependence and polarization dependence. However, with proper material engineering SHG efficiency can be enhanced in birefringent materials, as the phase matching condition can be satisfied. An external factor could be the optical filters used in the experimental setup. These filters have different transmission profiles, resulting in a variation in the intensity of SHG signal for different incident wavelengths (transmission profile of the filters are discussed in Appendix B).

Figure 4.6 (b) and (c) present the polar plots obtained under P and S analyzer configurations. The polar plots were constructed using the area of the observed SHG peak as a function of the respective incident polarization. These films have the rhombohedral phases, however, we do not observe any characteristic features related to the symmetry group of this material structure. Also, there is no symmetrical correlation present between S and P polar plots (Fig. 4.6 (b) and (c) respectively). Unlike the study on the polycrystalline BTO-BFO [198], we could not resolve the crystal symmetry of the films using far-field SHG spectroscopy. One explanation for this is that the observed SHG could be an averaged intensity over multiple domains. Each intensity for a particular polarization results from multiple nonlinear tensor elements resulting in a complicated polar pattern. Given the nature of far-field measurements our observations are resulted from bulk effects. Thus, a systematic growth and additional characterizations would be required to study the observed differences.

4.4 Conclusions

Our observations of TROIB and TRMOKE suggest that the sensitivity of CPs to the external magnetic fields and polarization could be probed more effectively using these two methods compared to transient differential reflectively, which traditionally has been used in many materials systems [2].

In this study, we have illustrated that magnetic field dependence of CPs measured by TROIB and TRMOKE demonstrated more sensitivity to the external magnetic fields compared to the transient reflectivity reported on the same BTO-BFO film structure under the exact experimental conditions [2]. We observed the amplitude of the OIB signal, Kerr signal as well as CPs' strength decrease, with the increasing magnetic field strength. These observations raised several interesting questions: (1) Why would one observe more sensitivity of CPs to magnetic fields and polarization when probed with TROIB and TRMOKE? and (2) Why does the amplitude of the OIB signal, Kerr signal, and the CPs' strength decrease, with the increasing magnetic field strength? To address these questions we are pursuing systematic collection of measurements with new BTO-BFO samples. Nevertheless, these techniques could be important for increasing the sensitivity of CPs' detection and amplification. These multiferroics provide technological outlooks such as optical switching and EOM. In addition, one can generate and control the photo-generated CPs to ultimately control electric, magnetic, and strain fields [10, 178, 179].

The ability to generate and manipulate the time resolved dynamics and phononic degrees of freedom in materials with external optical, electric, and magnetic fields promise new opportunities for employing these high quality materials for advanced optical and quantum devices at the nanoscale. The control of coherent properties in these new generation of engineered materials will establish platforms for CPs based devices when high resolution

and sensitivity are required, including information technology and quantum sensing [10]. Very little work has been conducted in multiferroic layered structures and our results in this study will open directions for new class of engineered materials based on the ability to generate and control the vibrational properties of materials.

Nonlinear optical processes at the nanoscale can play important roles in the advancement of optoelectronics, quantum optics, information technology, and also in the development of new light sources. To the best of our knowledge, we have reported the first demonstration of SHG in multiferroic BTO-BFO layered structures using far-field SHG spectroscopy. Our SHG studies suggest that the multiferroic BTO-BFO structures are a good candidate for nonlinear optical applications. Here, we have discussed the excitation and polarization dependence of SHG in BTO-BFO layered structures where the polycrystalline nature of the films resulted in a complicated polar symmetry in the polarization dependence measurements.

Chapter 5

Optical Properties of $Pb_{0.52}Zr_{0.48}TiO_3$ Nanorod Arrays: Second Harmonic Generation and Multiphoton Carrier Dynamics

In this chapter I have discussed our findings on nonlinear optical properties of lead zirconate-titanate ($Pb_{0.52}Zr_{0.48}TiO_3$) nanorod arrays, grown on Pt-coated Si with ∼200 nm diameter and ∼600 nm height. Here we observed a clear signature of second harmonic generations, from 490-525 nm (2.38-2.53 eV) at room temperature. Furthermore, we performed time resolved differential reflectivity measurements to study dynamical properties in the range of 690-1000 nm where multiphoton processes were responsible for the photoexcitations. We compared this excitation scheme, which is sensitive mainly to the surface states, to when the photoexcited energy (∼ 3.1 eV) was close to the bandgap of the nanorods. Our results offer promises for employing these nanostructures in nonlinear photonic applications. In this work, I performed TRDR measurements and SHG measurements of PZT nanorod arrays and film structures. The TRDR measurements were conducted for multiple NIR incident wavelengths. For SHG

studies, I have conducted power dependence, wavelength dependence, and incident polarization dependence measurements. I also wrote a large portion of the experimental sections.

5.1 Introduction

Optoelectronic technologies, based on the second harmonic generation (SHG) effects, have been making impacts in devices such as ultrafast pulse laser generation [35], optical switches [38], modulators [39] , materials analysis, and sensors [33, 34, 40, 203]. Toward these advancements, employing low dimensional materials systems have attracted many research activities, aiming for more tunability, miniaturization, and integration on chips.

Beyond commonly used materials such as $LiNbO_3$, KDP, KTP, and BBO [204], low dimensional materials are being explored as promising alternatives to existing nonlinear optical materials. With the advancement in material engineering and material fabrication techniques, several emerging 2D structures have been studied including graphene [205], graphdiyne [206], 2D metal–organic frameworks (MOFs) [207], antimonene [208], and 2D transition-metal carbides, [209], and carbonitrides [210].

Furthermore, for broader photonics applications it is redundant to discover and explore materials with new functionalities. Ferroelectric nanostructures have been widely studied due to their broad range of applications where their piezoelectric and pyroelectric properties can be used in sensors [211, 212], actuators [213, 214, 215, 216, 217], transducers [218, 219], infrared detectors [220], and energy harvesting [219, 221, 222, 223, 224, 225, 226, 227]. Our $Pb_{0.52}Zr_{0.48}TiO_3$ (PZT) nanorod arrays in this study, exhibit excellent coupling between electro-mechanical parameters and display polarization switching behavior along the growth direction, making them ideal candidates for nonvolatile memories [110, 228, 229].

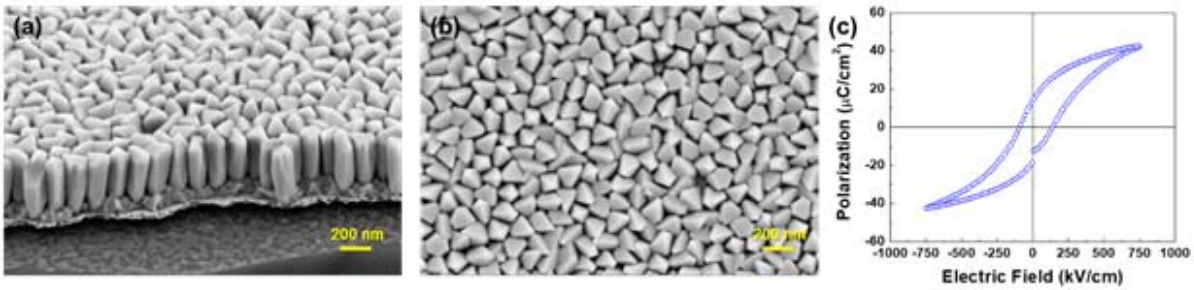

Figure 5.1: Cross-sectional FESEM image (a) and surface morphology (b) of PZT nanorod arrays. While each nanorod is a single crystal, the ensemble is composed of nanorods with random orientations. The array has a close-packed structure and is nearly homogeneous in diameter and height. (c) Polarization vs electric field (P-E) loop for the nanorod arrays displaying ferroelectric behavior.

Because the optical properties of these single crystalline PZT nanorod arrays are less explored, in this work we present SHG, in which for practical applications, these nanorods can be easily grown on commercial silicon wafers to be compatible with existing semiconductor devices. We also used time resolved differential reflectivity (TRDR) measurements to characterize the nature of carrier relaxation dynamics in this nanostructure. Near infrared (NIR) optical pulses were used, to probe multiphoton absorption, in which the relaxation dynamics are expected to be sensitive to the surface states. To directly probe the interband carrier dynamics, we employed near gap excitation at 400 nm. Probing these two schemes allowed us to probe several different relaxation mechanisms in these nanorod arrays.

5.2 Sample Preparation and Characterization

The PZT nanorod arrays in this study were synthesized through the physical vapor growth method. The nanorods were grown on 20 nm diameter $La_{0.67}Sr_{0.33}MnO_3$ (LSMO) seeds, patterned on top of Pt coated Si(100) substrate through a polymer nano-template method,

using RF sputtering at 400 ^{0}C. The microstructure of PZT nanorod arrays was observed using field-emission scanning electron microscopy (FESEM, LEO 1550). The PZT nanorod arrays were synthesized with ∼200 nm diameter and ∼600 nm height, as shown in Fig. 5.1(a,b). The PZT nanorods were found to have a close-packed structure and nearly homogeneous dimensions for diameter and height, grown on commercial grade 3 inches silicon wafer [230]. While each nanorod is a single crystal, the ensemble is composed of nanorods with random orientations. From X-ray diffraction (XRD) patterns, the nanorod arrays were found to exhibit perovskite phase without any secondary phases. The nanorod arrays exhibited randomly oriented diffraction peaks without preferred crystal orientation, which is often observed in the polycrystalline thin films due to the difference in the coefficient of thermal expansion between the substrate and thin film. The nano-structuring in PZT can overcome the influence of the substrate clamping effects [230].

The polarization-electric field (P-E) loop for the PZT nanorods was measured using the ferroelectric tester (Premier II, Radiant), and it was found that the nanorods exhibit typical ferroelectric behavior with remnant polarization of ∼16 $\mu C/cm^2$ (Fig. 5.1(c)). In order to induce the switching of the polarization direction of the nanorod arrays, the corona poling method was used [231]. A DC bias of 23 kV was applied between the Pt bottom electrode and a sharp tungsten tip placed 5 cm above the sample surface to generate a corona discharge through the partial breakdown of air. This method forms electrical charges on the sample surface and enables non-contact ferroelectric polarization switching over a large area [110].

5.3 SHG in PZT Nanostructures

Pulsed femtosecond lasers are suitable sources to observe nonlinear optical phenomena. The field generated by the incident light in a nonlinear medium gives rise to nonlinear effects like

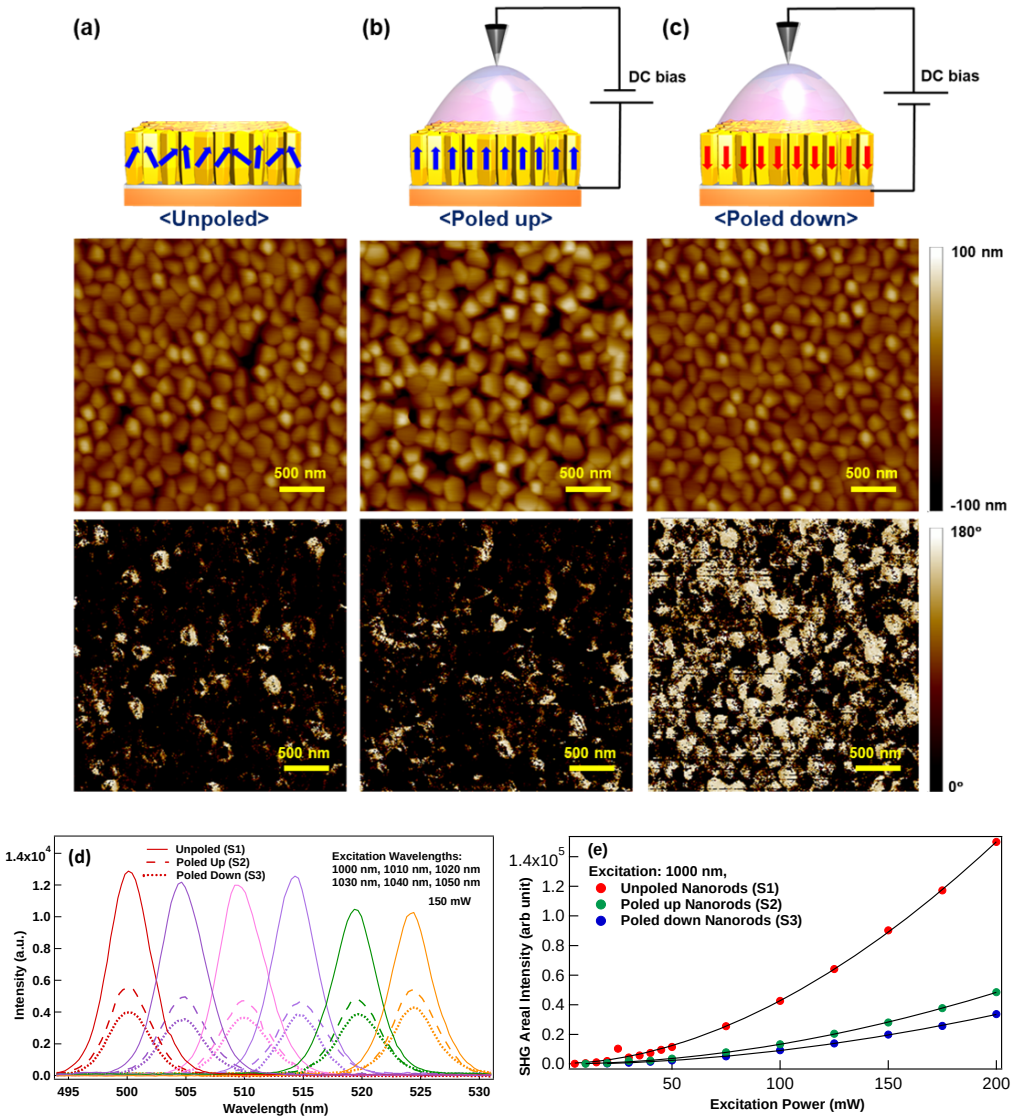

Figure 5.2: Piezoresponse force microscopy (PFM) images of PZT nanorod arrays with (a) unpoled, (b) poled down, (c) and poled up states. The images present both the topology (top panels) and phase signals indicating the polarization directions (lower panels) of the nanorods. The samples are different pieces from the same wafer. (d) The amplitude of SHG response for the unpoled (S1), poled up (S2), and poled down (S3) PZT nanorod arrays. (e) Power dependence of the samples show the SHG intensity is proportional to the square of the intensity of the incident light.

SHG where the electric field of the incident light results in an atomic dipole moment in the material. These nonlinear optical processes can be described macroscopically [202], by the induced polarization as following:

$$P(t) = P_0 + \varepsilon_0 \chi_e E(t) + \chi^{(2)} E^2(t) + \chi^{(3)} E^3(t) + ..., \tag{5.1}$$

where P_0 is a constant polarization, the second term describes the linear response, and the higher order electric field terms describe the nonlinear optical response. The third term in Eq. 5.1 gives rise to the second-order nonlinear optical phenomena, such as SHG, where $\chi^{(2)}$ is the second-order nonlinear electric susceptibility. The polarization is an odd function in a nonlinear material system with an inversion symmetry (*i.e.* a centrosymmetric medium). Therefore, second-order nonlinear phenomena can only be observed in a medium where inversion symmetry is broken. In nanostructures, SHG is generated favorably at grain boundaries, interfaces, and defects. Compared to thin films, in nanorods, the surface to volume ratio is higher, resulting in a higher surface SHG contribution, as the effective surface dipole moment is also higher [204, 232, 233].

In this work, the SHG measurements at room temperature were probed, on both unpoled and poled nanorods from the same wafer. The piezoresponse force microscopy (PFM) response confirming the surface poling and is presented in Fig. 5.2(a-c). The initial polarization state of as-grown nanorods is the upward direction (out of plane). Without poling, the initial polarization of the nanorod arrays tend to most likely follow the growth direction (5.2(a)); but the poling process is still required to align the polarization direction of the nanorods along the z-direction (Figs. 5.2(b) and (c)).

For this study, the laser source was a Coherent Chameleon Ti:sapphire laser with a repetition rate of 80 MHz, and a pulse duration of 100 fs. We carried out measurements for wavelengths

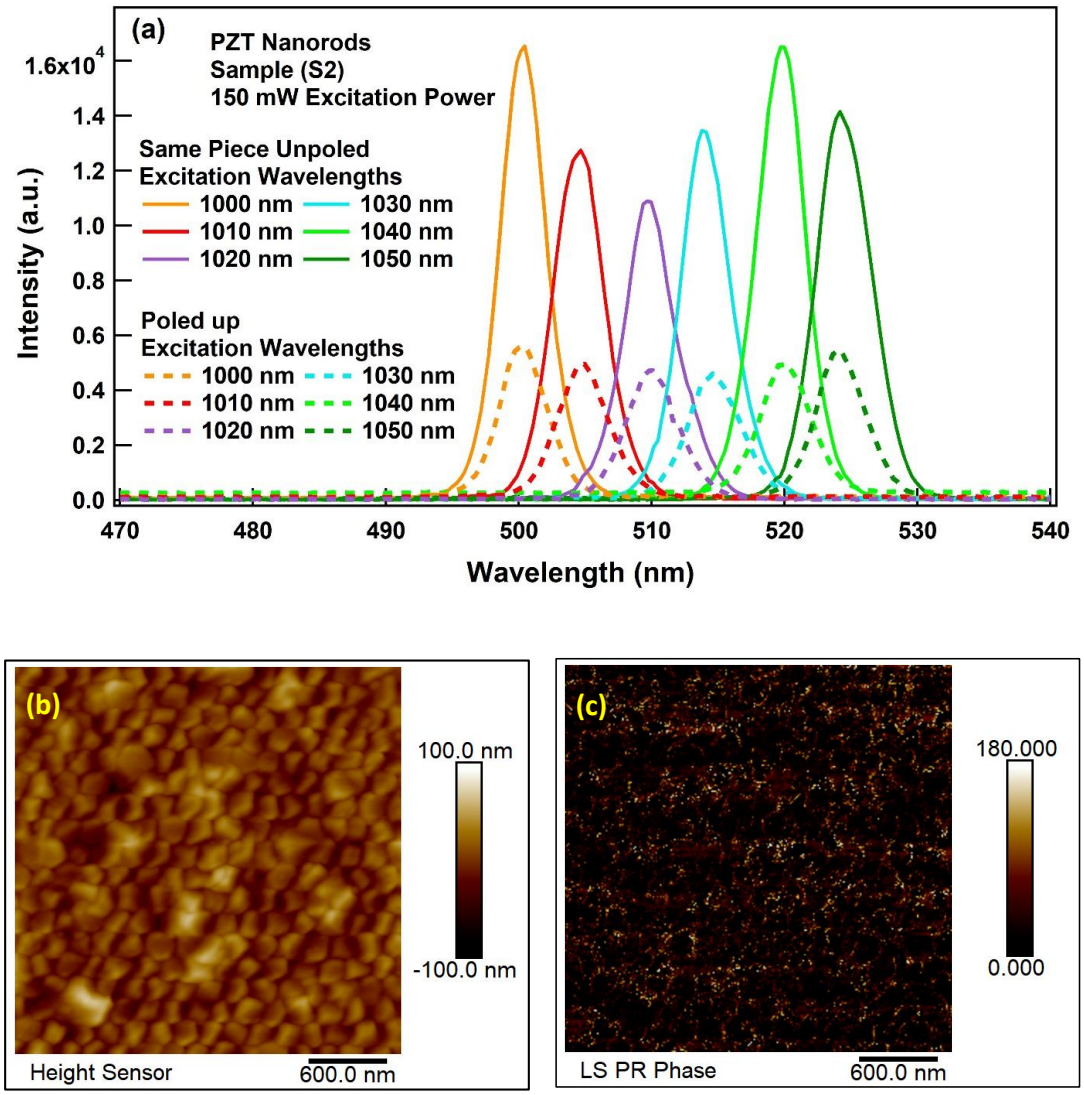

Figure 5.3: (a) Here we present the amplitude of the SHG for sample (S2) for when it was poled and then after it was heated to 400 ^0C. The measurements are under the exact same conditions. The SHG amplitude of the unpoled state of sample S2 is comparable to S1 (unpoled), in Fig. 5.2(d). (b) Topology from PFM measurements and (c) the phase of Sample S2, after it was heated to 400 ^0C for about 10 minutes, confirming the sample is unpoled after being heated.

ranging from 690 nm to 1050 nm. The laser pulses were horizontally polarized (P-polarized). Figure 5.2(d) presents SHG on the three nanorod arrays, where the unpoled sample exhibited higher amplitudes under the same experimental conditions compared to the poled structures. Furthermore, the SHG intensity is expected to be proportional to the square of the intensity of the incident light (${I_w}^2$). As shown in Fig. 5.2(e) we observe this quadratic dependence in all three samples.

In order to probe the differences between the poled and unpoled samples, in Fig. 5.3(a) we compare the SHG of sample S2 (poled up) under the exact experimental conditions before and after the sample was heated to $\sim 400\ ^0$C to be unpoled. In Sample S2, the amplitude of the SHG, after heating is comparable to the SHG amplitude of sample S1 (unpoled), in Fig. 5.2(d). In Fig. 5.3(b), We also present the PFM images of the sample S2 after it was heated, demonstrating the sample is unpoled when the SHG was measured.

To provide some insights to the observed differences in the SHG amplitudes, we should note that the phase-matching (PM) condition can play a role. For an isotropic crystal [113], SHG emitted from regions located within distances, comparable to the emission wavelength, can destructively interfere with each other. In disordered polycrystalline materials, a random quasi-phase-matching condition as an alternative method to enhance SHG conversion efficiency was demonstrated [112]. In their study they reported that SHG resulted from different domains in a polycrystalline disordered structure, with nonidentical domain parameters (orientation, shape, and size), would acquire random phases [112, 113]. In a far field measurement such as our setup, when multiple randomly oriented single crystal domains exist and can be probed, one would expect that the interference would not be a major issue and thus the resultant SHG intensity is the sum of each SHG amplitudes from different domains. [113, 234]. In Tetragonal $CH_3NH_3PbI_3$ the presence of multiple ferroelectric domains resulted in destructive interference between SHG scattered from domains with

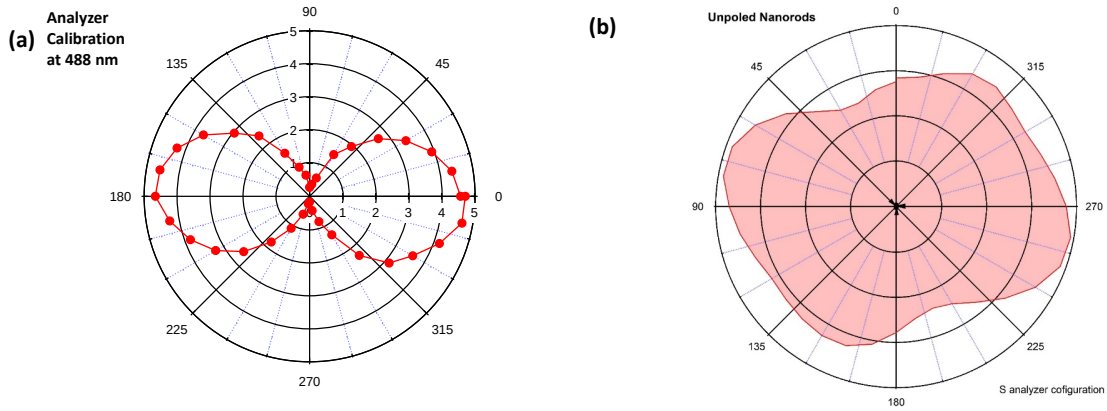

Figure 5.4: (a) Testing the analyzer sensitivity to polarization with a laser at 488 nm. We used this wavelength as the SHG in the nanorods are close to this range. (b) The incident polarization dependence of SHG in the unpoled nanorod at 980 nm using an analyzer, with an analyzer set at S polarization on the emission path, similar to the measurements in panel (a).

inverted polarity [235].

Furthermore, The coherence length, described as the distance in which the SHG intensity drops to zero due to destructive interference, depends on the excitation wavelength and the difference between the index of refraction associate with the SHG and the excitation wavelengths in a given material [202, 234]. Therefore, in our samples, we would expect the amplitude of SHG to display some dependence on wavelengths and the overall orientation of the ferroic domains.

5.4 SHG: Polarization Dependence

We also explored the polarization-dependence of SHG where the incident laser polarization was varied via a Half-Wave Liquid Crystal Variable Retarder/Wave Plate (Thorlabs; LCC1221-B), with an analyzer positioned before the spectrometer set at vertical (S) polarization. To test the sensitivity of the analyzer, we first used a 488 nm laser where the power plot as a function of polarization is presented in Fig. 5.4(a), showing a symmetric pattern.

Furthermore, Fig. 5.4(b) presents the polar plot with 980 nm, 200 mW incident power, for S1 (unpoled sample). Here we have constructed the polar plots using the area of the observed SHG peak as a function of incident light polarization. Compared to single-crystal systems, polycrystalline systems increases the complexity of determining the symmetry point groups of the material structure because, in a multi-domain system, the observed SHG intensity could be related to the net polarization of the domain pattern or the collective intensity of each contributing domain state [201].

Looking closer at the polarization dependence, as shown in 5.4(b), we observed a moderate dependence of the SHG intensity with respect to the incident polarization that displays four lobes. We note that in a previous work [236], PZT solid solutions with the composition close to x= 0.47 exhibited a morphotropic phase boundary with rhombohedral and tetragonal symmetries. Thus, the observed polar plot could be resulted from the combination of the two phases in the PZT. Similar SHG observations have been reported in $BiFeO_3$ (BFO) films, where the authors have attributed the observed double lobed configuration to the combination of the monoclinic point group symmetry in BFO of each phase [200, 237]. Moreover, Jie-su Wang *et al.* [199] reported the SHG observation of non-zero minimum for thicker BFO films due to the overlapping of SHG signal generated from rhombohedral and tetragonal phases domains [199]. We should also note that the laser beam of $\sim$ 1 mm diameter covers a large number of individual nanorods; thus, the observed SHG could be an averaged intensity over multiple nanorods resulting in less clearly resolved double lobed shape.

To show a few more examples of the polarization dependence in these nanorod arrays, Figs. 5.5(a-d) display SHG intensities, for two different excitation (S and P) and analyzer (S and P) configurations. These measurements were taken at 980 nm and 1000 nm under the exact same conditions. For all four configurations, the largest amplitude was measured when the

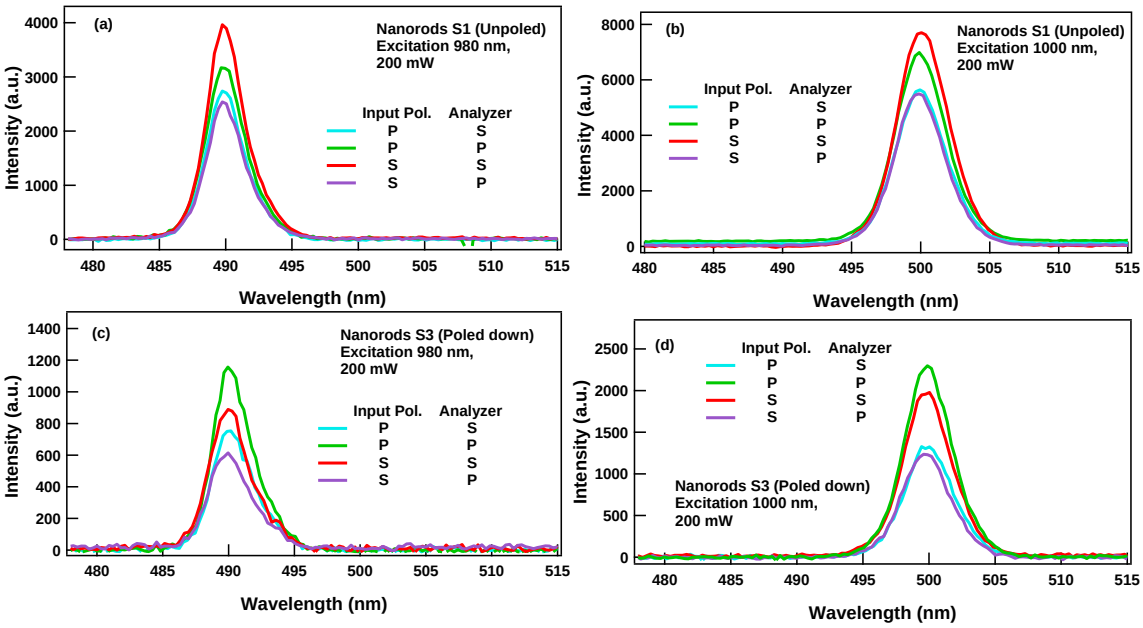

Figure 5.5: (a-d) Here we present the examples of the polarization dependence at 980 nm and 1000 nm for the samples S1 and S3. We observe some polarization dependence in the SHG, for different configurations of the incident and analyzer states.

excitation and analyzer polarizations were at the same states. For the unpoled PZT sample (S1), S excitation polarization with S analyzer (S-S) configuration has the highest amplitude. In case of the poled down sample (S3) in Figs. 5.5(c-d), the P-P configuration displayed the highest SHG emission. We should note that here the observed differences are due to the net polarization direction of the PZT nanorod array.

The second harmonic anisotropy pattern changes with the corresponding domain variant of the ferroelectric domain structure. [238, 239] The sample S1 (unpoled) has a net polarization direction to be partially upward whereas the net polarization direction sample S3 (poled down) is downward with respect to the sample structure resulting in different in-plane and out-of-plane contributions to the final SHG amplitude. This results in different SHG anisotropy patterns with different intensities. Thus, the observed change in the SHG amplitude with the different incident polarizations and the analyzer configurations for the

two samples (S1 and S3) could be due to the different in-plane out-of-plane contributions of each sample. Similarly in a recent study, Zhang *et al.* [239] reported a significant difference in the shape and the intensity of the SHG polar pattern with different in-plane and out of plane domain components. In their study the authors have illustrated the relationship between azimuth polarization dependent SHG signals and domain variants, for BFO, BTO, and PZT films. Moreover, they demonstrated that in-plane domain components were distinguished by analyzing the azimuth-polarization-dependent SHG patterns whereas out of plane domain components were analyzed by comparing the variation in the SHG patterns taken at the initial position (0 ^0C), and after rotating the sample 180 ^0C around sample plane. We should note that for all the measurements presented here,the incident angle was kept $\sim$ 25 degrees and the sample holder was tilted by about 3 degrees(Fig. 4.6 (a)).

5.5 Carrier Relaxation Dynamics in PZT Nanorods

Ultrafast time-resolved spectroscopy can be a useful tool for studying the energy relaxation processes and carrier dynamics in a wide variety of nanostructures. The extracted information can be used toward developing fast optical switches. Two types of ultrafast spectroscopy are commonly employed: Time Resolved Differential Transmission Spectroscopy (TRDT) and TRDR. In carrier dynamics studies, TRDT measurements usually provide information on the exact energy state within a given band a carrier occupies and how it scatters into/out of that state. Photoexcited carriers within a given state block the absorption of further carriers through the Pauli exclusion principle (phase space filling). The TRDT signal is sensitive to all the photoexcited carriers throughout the entire thickness of the sample. TRDT measurements can provide detailed information on scattering rates from specific electronic states, but have the drawback that they are limited to thin samples (compared to the absorption

depth) since the light must get through the sample.

In contrast to TRDT, transient reflectively measurements depend upon the changes to the index of refraction that result from the photoexcited carriers. As a result, the TRDR measurements are not sensitive to the exact state within a band the photoexcited carrier occupies, but rather are sensitive to the effective mass of the bands, in which the carriers reside; therefore, the scattering of a carrier *within* a band does not produce a change in the TRDR spectrum. Furthermore, the TRDR signal depends on the gradient of the change in the index of refraction due to the photoexcited carriers. This process is typically stronger at the surface of the sample, and as a result, TRDR measurements studying carrier dynamics are mainly sensitive to the carriers near the surface [2, 24].

We employed TRDR and Fig. 5.6(a) displays degenerate pump/probe measurements at different NIR wavelengths, where we expected to observe multiphoton absorptions . The pump pulses had a spot size of 150-200 μm exciting multiple rods. For the carrier contribution, the TRDR signal, as noted above, is sensitive to the *photoexcited carriers at the surface* (or in layered structures, possibly at the interfaces). We should note that we required the maximum possible pump powers for the different NIR excitations to observe the multiphoton process, but these pump powers could not have been identical for each wavelength.

In TRDR, the differential reflection is related to the gradient of the change in the index of refraction that results from the pump pulse. This gradient is largest were there is a discontinuity in the change in index such as at the surface or an interface. The change in index comes about because, the carriers generated by the pump pulse, will change the real and imaginary parts of the dielectric function and hence, the index of refraction. As a result, TRDR measurements are sensitive to the density of photoexcited carriers near the surface of the sample. Photoexcited carriers can change the index of refraction in several ways. Some of the ways are described in detail by Zollner *et al.* [24] which we just summarize here. They

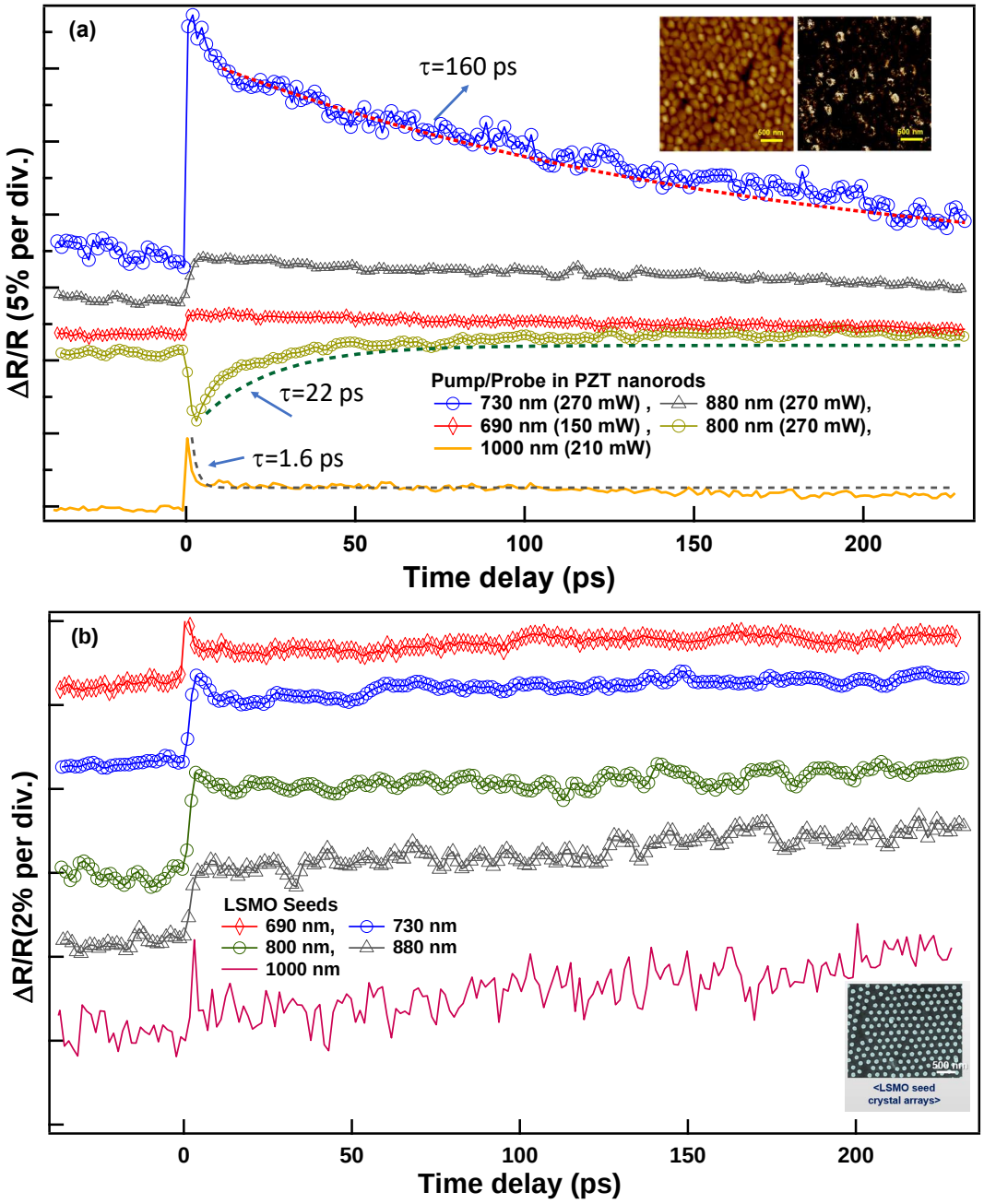

Figure 5.6: (a) Room temperature TRDR of PZT nanorods of the unpoled sample (S1). We observed carrier dynamics where both the pump/probe wavelengths were tuned in NIR. We should note, except at 800 nm, we observed an increase in the transient reflectivity, with the largest increase of $(\Delta R/R)$ at 730 nm. The inset shows the topology and the phase of the nanorods using SEM. (b) Similar measurements on the LSMO seed show a much smaller response to the NIR optical excitations with no sensitivity to the variations in the excitation wavelengths. The inset displays the SEM image of the LSMO seeds to compare with the PZT nanorods' topology.

include:(1) Drude Model/induced free carrier absorption: Photoexcited carriers can screen internal electric fields and hence change the Drude part of the dielectric function (this is equivalent to have an photoinduced enhancement of the free carrier absorption). (2) Many body effects which include both the renormalization of the band gap by the photoexcited carriers as well as the change to the Coulomb enhancement of the optical matrix element arising from the screening of the photoexcited electron-hole Coulomb interaction by the other photoexcited carriers. (3) Phase space filling of the interband contribution to the dielectric function, which has a strong effect on the absorption and thus must also effect the index. While the first effect is considered to be the dominant effect, the relative importance will depend on the exact details of the electronic band structure of the material as well as the excitation wavelength of pump laser pulse and the wavelength of the probe pulse.

Typical ways that the surface carrier dynamics can be altered include: (i) scattering of carriers at the surface to *different bands* (with different effective masses), (ii) recombination of photoexcited carriers (across the gap), (iii) diffusion of photoexcited of carriers away from the surface (including possible drift effects if there are internal fields) [2, 24] and (iv) trapping/recombination of carriers at surface/interfaces. The thickness of layered structures can also influence the relaxation dynamics. More specifically, for thin layers, photoexcited electrons can reach a surface or interface and recombine with the surface states in a few picoseconds without any radiative or thermal recombination. Carrier dynamics in an InN nanorod arrays demonstrated wavelength dependence, where similar to our observations the sign change of $\Delta R/R$ was attributed to nonlinear effects such as band gap renormalization and the bleaching of the absorption near the absorption edge.

Since the band gap of PZT ($\sim$ 3.4 eV) is greater than the excitation energy of the laser pump pulse, the absorption depth is fairly large $\approx 0.5 - 1.0\ \mu m$ or more, one initially might not expect diffusion to play a role. However, the dominant method of photoexcitation is

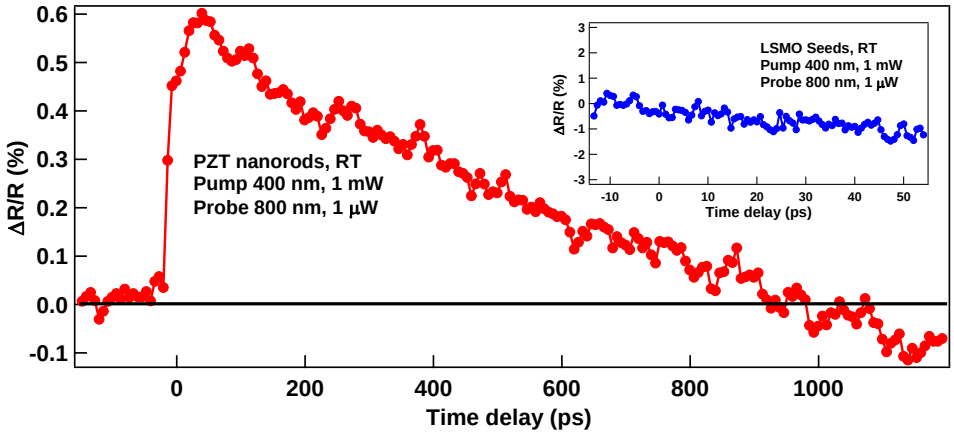

Figure 5.7: The transient reflectivity of the nanorods in a two color scheme where the pump tuned at 400 nm is close to the expected bandgap of PZT. The inset shows the pump-probe measurements on the LSMO seeds under the exact experimental condition.

not through *single* photon absorption, but is instead through *two* photon (or multi-photon) absorption. It is well known, that carriers generated by two (or multiple) photon absorption can be highly spatially confined or localized. Depending on the focus, this is typically near the surface. This allows one to investigate carrier dynamics and transport in these systems. As carriers generated near the surface, diffuse into the sample.

Our observation of TRDR in the nanorods with the photoexcited carriers generated along the rods, could be more complex than what one would expect in films, specially when we articulate that multiphoton processes are involved. Furthermore, the additional surface area of the nanorods could lead to a larger number of surface traps/defects which in turn could affect the carrier relaxation dynamics. As shown in the Fig. 5.6(a), in the case of the pump/probe at 800 nm, the dynamics start with a negative rise in the $\Delta R/R$ where the decrease at timing zero can be attributed to the Pauli blocking when conduction states fill up, causing the refractive index to decrease, resulting in a negative $\Delta R/R$. The dynamics at this pump/probe scheme can be fitted with one single exponential decay with the time constant of 22 ps.

For the pump/probe excitations at 690 nm and 880 nm, we observed positive changes in $\Delta R/R$ followed by decays characterized by slow time constants. The slow relaxation phenomena are typically attributed to carrier diffusion where there will be a large positive offset at long time delays. In this case, all the absorbed energy could heat up the lattice indicating a slow thermal diffusion in these two pump/probe cases. Furthermore, for excitation at 730 nm and 1000 nm with positive changes in $\Delta R/R$ we can describe the relaxation with a single exponential fit resulting in decay component of 160 ps and 1.6 ps, respectively.

The sensitivity of the carrier dynamics to the excitation wavelength was reported in GaAs [240]. In their work, they observed an increase in the initial differential reflectivity for the incident pump wavelengths of 820, 875, and 880 nm and a decrease for 885 nm. Their observations of the sign changes in $\Delta R/R$ were consistent with the theoretical investigations of refractive index nonlinearities near the bandgap of GaAs. They associate the near band edge transient nonlinear optical response, to band-gap renormalization where the excitation energies were near bandgap. In our study, the incident wavelengths 690-1000 nm (1.80-1.24 eV), are below the bandgap for PZT nanorods of 3.4 eV [241]. But for two or three photon absorption, can either be above the band gap, or close to the band gap.

Thus, we observe several multiphoton processes in these measurements. At 690 nm (1.80 eV) it requires at least two photons to excite a charge carrier into the conduction band via an intermediate state. Similarly, at 1000 nm (1.24 eV) it requires at least three photons to excite carriers into the conduction band via an intermediate state. Although we did not expect the pump/probe excitations could reach to the substrate, we tested the bare LSMO patterned on top of Pt coated Si(100) substrate. As shown in Fig. 5.6(b) the observed dynamics for the substrate are different under the exact experimental conditions as the ones for the nanorods, and we observed only small response with no sensitivity to the excitation wavelengths. This fact confirms that the multiphoton excitations are mainly probing highly

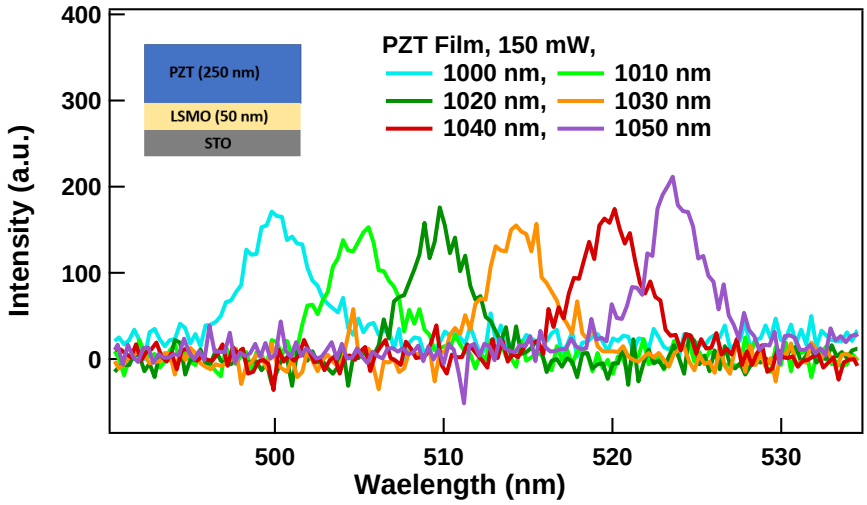

Figure 5.8: SHG response for PZT thin film structures. These measurements were taken with 120 second exposure time.

localized states of the nanorods on the surface.

Furthermore, As shown in Fig. 5.7 in order to probe the interband relaxation time scale, we used pump pulses closer to the bandgap of the PZT nanorods and we employed a two-color pump-probe scheme [2]. The pump and probe wavelengths were 400 nm and 800 nm, respectively where we used an amplified Ti:sapphire system with a repetition rate of 1 KHz. Our laser spot size was $\sim$ 150 μm in diameter with a pump power of 1 mW, and a pump/probe ratio of 1000:1. In this scheme we used a BBO non-linear crystal to upconvert the pump pulses from 800 to 400 nm. In this case, we observed a much smaller amplitude of $\Delta R/R$ with an initial sharp increase at the timing zero, followed by a slower increase. This fact suggests that the 400 nm pump pulse creates carriers in higher energy bands and the 800 nm pulses probe lower energy bands which see an increase in carrier density as the carriers in higher energy bands relax. This is similar to what is seen in Ge where one sees scattering and relaxation from the light hole bands to the heavy hole band (Figure 1(b) in Zollner *et. al* [24]).

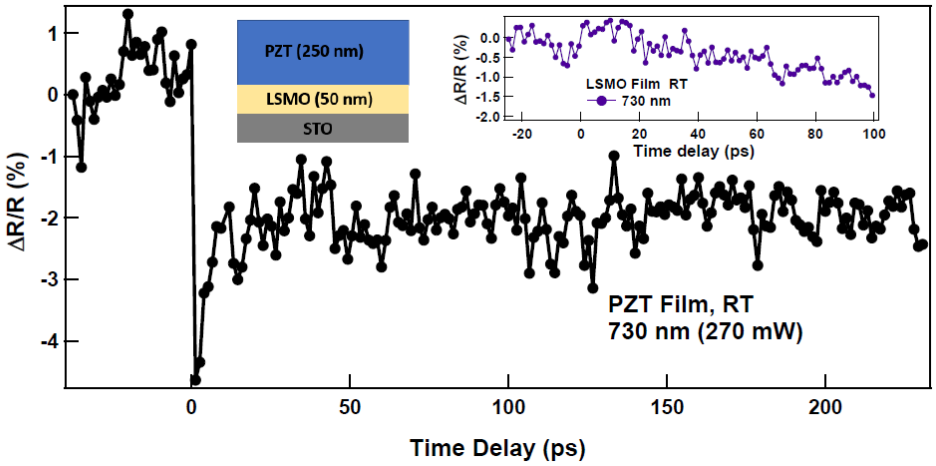

Figure 5.9: Room temperature TRDR of PZT thin film structure. Similar to nanorod structures in thin film structures, we observe carrier dynamics where the pump-probe wavelengths are tuned at 730 nm (∼1.70 ev) where two photon absorption were involved in the photoexcitation. The inset shows the pump-probe measurements on the LSMO substrate with same experimental condition.

We note that the photo excited carrier lifetime is much longer than the cases presented in Fig. 5.6(a), created via two or three photon processes. In this two color scheme the initial slow relaxation, is attributed to the carrier lattice heating (10-100 picoseconds) followed by an interband relaxation process of large carrier population (lasting $\sim$ 1 ns), after the initial thermalization. In addition, in the two color scheme, at 1 ns, $\Delta R/R$ changes sign, where we expected the system should have reached to equilibrium.

5.6 SHG and Carrier Relaxation Dynamics in PZT Films

We have also probed hetero-epitaxial PZT/LSMO thin films, which were grown on STO substrates by off-axis RF magnetron sputtering. These films were probed under the same experimental conditions as the nanorods to detect the SHG emission. Figure. 5.8 displays SHG on the PZT thin film structure, that shows much lower emission intensity compared to

the nanorod arrays (Fig.5.2(d)). Compared to thin films, the surface to volume ratio is higher in nanorods, resulting in a higher surface SHG contribution, as the effective surface dipole moment is also higher [204, 232, 233]. As we discussed earlier, for practical applications higher conversion efficiency of SHG is needed. Our observations showcase that these newly engineered PZT nanorod structures have enhanced SHG conversion efficiency compared to PZT films.

Furthermore, we also probed this PZT film using degenerate TRDR at room temperature (Fig. 5.9). Similar to nanorod structures, in this film we observed carrier dynamics where the pump-probe wavelengths are tuned at 730 nm (1.70 eV) where two-photon absorption was involved in the photoexcitation. The response was much smaller and could be only detected at this pump-probe wavelength.

5.7 Conclusion

Our optical characterizations presented in this study, provide new directions to employ PZT nanorods, with enhanced piezoelectric and ferroelectric performance, for devices on the basis of SHG when low dimensionality and compatibility to Si are desirable. The choice of PZT, with a bandgap of $\sim$ 3.4 eV, has the additional advantage of avoiding the re-absorption of the SHG emissions in the observed range of (2.36-2.5 eV). Employing nonlinear optical processes at the nanoscale can play important roles in quantum optics, information technology, and in the development of new light sources.

Furthermore, we used TRDR spectroscopy to study the dynamical properties of the nanorods. Probing the carrier dynamics, both close to the bandgap, as well as through multiphoton processes allowed us to identify several relaxation dynamics. The TRDR through multiphoton excitations displayed strong wavelength dependence, where the dynamics are typically

occurring near the surface and the relaxation processes can be dominated by carrier diffusion. Moreover, we used near gap excitation at 400 nm to identify the interband relaxation time scale, and estimated to be about 1 ns. These results provide insights for different paths toward optical manipulation of these less explored PZT nanorods in time domain; suggesting that they have potentials for fast optoelectronic applications. The possibility of employing NIR excitation provide an opportunity to go beyond traditional visible spectroscopy in which multiphoton time resolved spectroscopy can shade light to new and important dynamical tunability.

Chapter 6

Contributions to Other Studies

6.1 TRDR Measurements of Self-Assembled $CH_3NH_3PbI_3$ Perovskites

This section was adapted from the manuscript: Congcong Wu, et al. Highly Stable OrganoLead Halide Perovskites Synthesized Through Green Self Assembly Process. Semicond. Sol. RRL , 2, 1800052 (2018). © 2018 WILEY-VCH Verlag GmbH & Co. KGaA, Weinheim

This paper was selected as the cover page in Solar RRL, 2, No.6 (2018)

My contribution to this work was performing TRDR measurements of these Perovskites structures and setting up the experiment.

Organic-inorganic hybrid perovskite solar cells (PSCs) has gained increased attention in recent years, due to the higher efficiency and cost-effective fabrication procedures. Methylammonium lead iodide, $CH_3NH_3PbI_3$ ($MAPbI_3$), is one such organic-inorganic semiconductor that has higher potential in photovoltaic applications. In addition to solar cell applications, these perovskite material are also used in thermoelectric [242] and optoelectronic technologies [243]. However, these materials suffer from a lack of long-term stability. This study demonstrates a highly stable $MAPbI_3$ perovskite using a newly-developed self-assembly (SA) process. The newly developed perovskite system comprised of $MAPbI_3$-PMMA and it demonstrates excellent stability under high moisture conditions. Moreover, it exhibits no

phase change under $\sim$ 70% humidity for 31 days and excellent performance in 50 to 70% humidity for 50 days. The time scale and the efficiency of photoexcited carriers' propagation across multilayer structures is critical to device performance on the basis of hot electron injections. Our contribution to this paper was conducting Time Resolved Differential Reflectivity (TRDR) measurements to explore the hot-carrier kinetics for the perovskite films. In this study, we employed a two-color Time Resolved Differential Transmission (TRDT) pump-probe measurements where the laser source was an amplified Ti:sapphire oscillator with a repetition rate of 1 KHz. The pump-probe pulses were tuned at 400 nm and 800 nm, respectively and the pulses had a duration of 100 fs, defining the resolution of the measurements. Both beams were focused onto the sample with a spot size of around 150-200 μm for probe pulses, and slightly larger for the pump. The pump-probe ratio of 1000:1, was kept for all the measurements, and the TRDR as a function of the time delay between the pump and probe pulses, using a Si detector, was recorded. The pump power of 0.3 mW is corresponding to a laser fluence of 1 mJ/cm^2 and a resulting photo-induced carrier density of the order of 10^{18} cm^{-3}.

Three different samples have been studied: pristine perovskite film ($MAPbI_3$), perovskite capped with PMMA layer ($MAPbI_3$+PMMA), and perovskite complexed with PMMA via self-assembly process (SA) ($MAPbI_3$-PMMA). As shown in Fig.6.1(a), the relaxations of the photo-induced carriers in these samples can be modeled by three-time constants, τ_1, τ_2, and τ_3, where τ_1 is attributed to the initial carrier cooling, τ_2 to the relaxation of hot electrons toward the bottom of the conduction band (τ_1 and τ_2 were extracted from a double exponential fit), and τ_3 to the recombination time scale. The calculated cooling time τ_1 of the pristine perovskite is 23.6 ps, the PMMA capped one is 27.7 ps, while for the SA PMMA film the cooling time is increased to 34.5 ps. The results indicate that the carrier transport in perovskite is not impeded in the novel structure ($MAPbI_3$-PMMA). The time

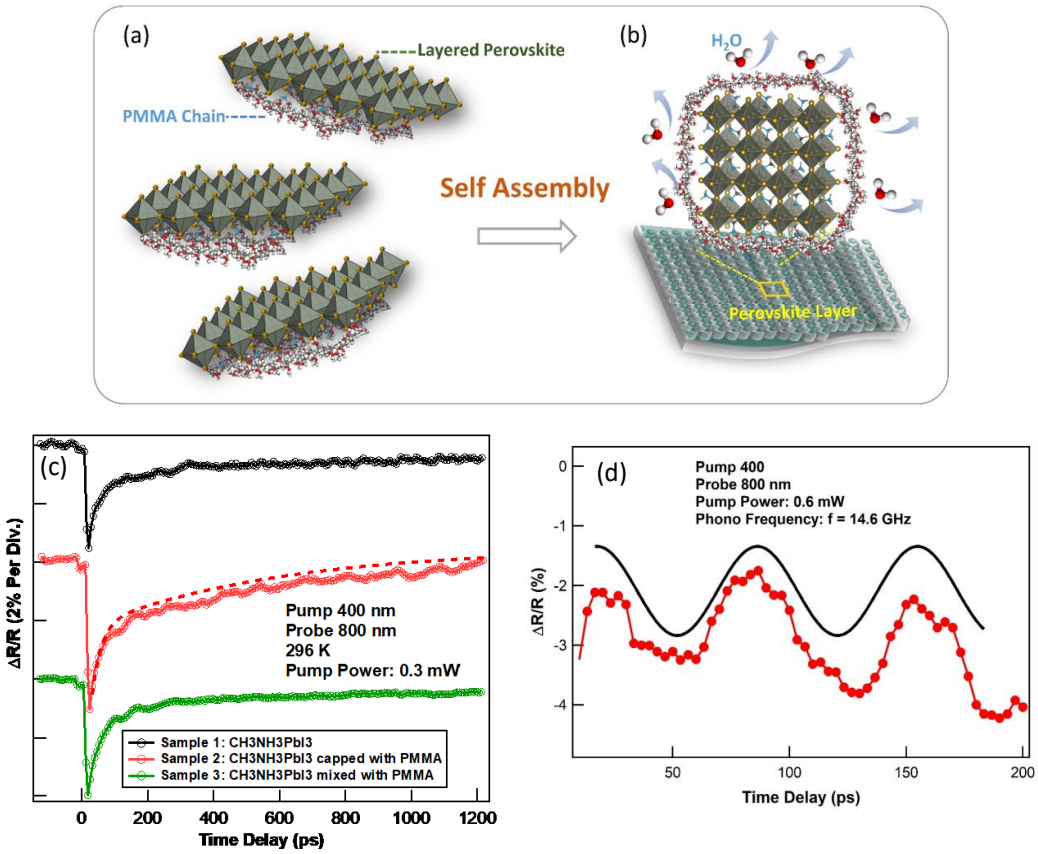

Figure 6.1: Schematic illustration of procedure for fabrication of coated perovskites through the self-assembly process and TRDR spectra of perovskite films. (a) The complexation between PMMA polymer chain and 2D layered perovskite intermediates. (b) Upon evaporation of solvent, the layered perovskite will be self-assembled, leaving PMMA anchored at the boundary of perovskite grains (c) TRDR of $MAPbI_3$ film (sample 1), $MAPbI_3$+PMMA film (sample 1), and $MAPbI_3$-PMMA film (sample 1) as a function of time delay, represents the relaxations of the photo-induced carriers in three samples. An example of a double exponential fit to extract τ_1 and τ_2 is shown for sample 2 and it is shifted for clarity. The exponential fits identify τ_2 to be ∼260 ps for sample 1 and 3 and much longer, ∼590 ps, for sample 2. We observed CP in all three samples in the panel (c) but increasing the pump power from 0.3 mW to 0.6 mW made the amplitude larger. (d) Close up of the CP oscillations from the perovskite film (sample 1), in which the fit is shifted for clarity and is corresponding to a phonon frequency of 14.6 GHz.

scale associated with the carrier cooling toward the conduction band (τ_2) is much longer for the sample capped with PMMA, while the carrier recombination (τ_3) remains the same for all three samples (longer than 1.2 ns). After the hot electrons are created, the lattice temperature rises and subsequently, the number of LO-phonons can increase. In the regime of large electron densities, due to screening effects and hot phonons, the photo-excited electrons experience a significant reduction in their energy loss rate through the emissions of LO phonons. We identify τ_1 as the thermalization time of the hot electrons to be $\sim$30 ps in the three samples presented in Fig. 6.1(a).

In addition to creating non-equilibrium electron-hole pairs, laser pulses can trigger oscillations in the optical properties due to Coherent Phonons (CP) . The CP then modulate the refractive index, which modulates the optical reflectivity of the sample, and can be measured by probe pulses. The thermoelastic stress and the deformation potential contributes, to generating CAP, following a photoexcitation via a pump pulse. As shown in Fig. 6.1(c) we observed clear CP oscillations in this structure, the fit to the oscillation is corresponding to a phonon frequency of 14.6 GHz, which is similar to the 12 GHz frequency observed by Mante *et al.* in single crystal $CH_3NH_3PbI_3$ [244]. Methods of tailoring and controlling vibrational properties in the past have relied on complex inter-digitated transducers to generate surface acoustic waves in a variety of structures. Vibrational properties can be controlled more efficiently through transient coupling between carriers and dynamic strains, using optical fields from femtosecond laser excitations and we have demonstrated we can generate CAPs in a perovskite layered structures.

6.2 Photoluminescence Measurements of InAs/AlAsSb Multi-quantum-well Hot Carrier Absorber

This section was adapted from the manuscript: V R Whiteside, et al. Valence band states in an InAs/AlAsSb multi-quantum well hot carrier absorber. Semicond. Sci. Technol. 34, 025005 (2019). *© IOP Publishing. Reproduced with permission. All rights reserved*

My contribution to this work was setting up and assisting with photoluminescence measurements of these multi-quantum-well structures.

The focus of this study was to provide detailed temperature-dependent simulations for absorption and photogenerated recombination of hot electrons and a comparison of the experimental photoluminescence (PL) data for an InAs/AlAsSb multi-quantum-well. Photovoltaic solar cells are a clean source of energy where light is directly converted into electricity via the photovoltaic effect. Photovoltaic cells are an established technology where considerable attention has been given to increase their efficiency. In the process of photogeneration, the excess energy of the photogenerated carriers is lost through efficient carrier thermalization where the system thermalizes through the emission of longitudinal optical (LO) phonons that decay into two Klemens phonons. This process limits the efficiency of photovoltaics to ∼30% [245]. The highest recorded efficiency of photovoltaic cells is from multi-junction devices. But due to their high cost, they are only limited commercial terrestrial applications.

A cost-effective solution to reduce the energy lost to phonons is a "hot-carrier" solar cell. Here the photoexcited carriers are extracted before they lose all of their excess energy to the surrounding. The two main underlying principles employed to design hot carrier solar cell (HCSC) prototypes are: (1) increase the hot carrier density through re-absorption of phonons by the carriers [246] or inhibiting the cooling process [247, 248, 249], (2) use narrow

range contacts to cover only a limited portion of the distribution of hot carriers, to allow efficient collection of hot carriers. The proposed hot carrier absorber structure to investigate is comprised of 30 InAs quantum wells that are 2.4 nm thick with 10 nm thick $AlAs_{0.16}Sb_{0.84}$ barrier layers. The composition is such as to be lattice-matched to InAs; the growth conditions have been described previously [250]. The material structure was modified by removing the substrate, buffer layer, and cap to only probe the hot carrier absorber material.

This study reports the band structure calculation and the absorption and recombination spectra for the interband transitions, between the lowest energy electron subband and the lowest four-hole sub-bands, for the periodic well/barrier system. Our contribution to this study was to conduct photoluminescence (PL) measurements as a comparison to the simulations. The simulations of PL and the band structure calculations have a good agreement with the experimental PL. The room temperature e1-hh1 simulated transition energy of 805 meV closely matches the 798 meV transition energy of the experimental PL spectra with only a difference of only 7 meV. Likewise, the expected energy separations between local maxima (p1-p2) in the simulated/experimental spectra have a difference of just 2 meV: a simulated energy separation of 31 meV compared to the experimental value of 33 meV. Utilizing a non equilibrium generalized Planck relation, a full spectrum fit enables individual carrier temperatures for both holes and electrons. This results in two very different carrier temperatures for holes and electrons: where the hole temperature, T_h, is nearly equal to the lattice temperature, T_L; while, the electron temperature, T_e, is 'hot' (i.e., $T_e > T_L$). By fitting the experimental spectra via three different methods a 'hot' carrier temperature is associated with electrons only; all three methods yield similar 'hot' carrier temperatures. These results deduce that the hot carrier temperature is associated with electrons only. Thus, narrow gap heterostructures [5, 251] are a potential candidate for hot-carrier absorbers [252, 253, 254, 255].

6.3 TRMOKE Measurements of InAsP Films

In this work, I assembled the TRMOKE setup and conducted TRDR and TRMOKE measurements of InAsP films. Here, I have performed TRMOKE measurements at room temperature up to 800 mT.

Present day state-of-the-art electronic and optoelectronic devices use III-V compound semiconductors. Fundamental characteristics of materials are important when implementing them in devices to harness the desired characteristic. III-V layers heterostructures with different alloy composition and carrier confinements have gained substantial interest for microelectronic and optoelectronic applications owing to the ability to engineer the band structure of these material structures.

InAsP ternary alloys are one such III-V semiconductor that can be grown with a wide range of bandgaps from 0.36 to 1.35 eV by changing the alloy composition. This characteristic of InAsP opens up a wide variety of optoelectronic applications such as broadband photodetectors [256], mid-IR lasers [257], and optical telecommunication [258]. Moreover, InAsP has gained considerable interest in semiconductor-based quantum communication applications, owing to its wide range of g-factors (from 1.2 to -17.5) including g = 0 [259]. In order to implement quantum communication in real-life applications, one requires entanglement preserving photodetectors which can transfer photon polarization to electron spin coherently. Thus, to preserve the entanglement it is important to fabricate photodetectors using a material which has a conduction band g-factor much smaller than the valence band so that the photodetector can excite equally to the spin split states [259]. Another important factor to achieve in such photodetectors is to have a long spin relaxation time. InAs [260, 261] and InP [262, 263, 264] are two widely researched III-V compound semiconductor material which possess moderately long spin relaxation times. InAsP is a ternary compound which

demonstrates characteristics between InAs and InP, hence making it suitable for developing the above mentioned photodetectors.

Probable applications in spintronic, quantum communication and quantum information are the driving force for investigations of spin dynamics in semiconductor heterostructures. Having a fundamental understanding of electron spin relaxation and the magneto-optical aspect of it not only allows us to evaluate and develop sample quality but also benefits device optimization. Here we performed Time Resolved Differential Reflectivity (TRDR) and time resolved Magneto-Optical Kerr Effect (TRMOKE) measurements to investigate spin relaxation dynamics in InAsP.

We employed degenerate TRDR and TRMOKE at room temperature to investigate carrier and spin relaxation in InAsP thin films. The schematic diagram in Fig. 6.4 (a) displays the experimental setup of TRMOKE. Our light source was a Coherent Chameleon Ti:sapphire laser system with 100 fs laser pulses with a wavelength range of 700-1050 nm and a repetition rate of 80 MHz. The laser beam was split into pump and probe beams using a beam splitter. In the case of TRDR, after reflecting off of a retro-reflector on a delay stage, the linearly polarized pump beam was passed through a mechanical chopper with a frequency of 1kHz and focused on the sample using a lens. The spot diameter of the pump was 150-200 μm with a pump fluence of 9.55 μJ/cm^2 and the probe beam had a lower fluence of 95.5 nJ/cm^2. In order to assure the homogeneity of the observed transient dynamics the diameter of the probe beam was set to be smaller than the pump beam. The sample was mounted inside an electromagnet with a magnetic field range of 0-1 T. The reflected probe beam was focused on a Si balance detector.

For TRMOKE measurements, the pump beam was circularly polarized using a quarter-wave plate and the probe beam was linearly polarized (45 degrees) using a half-wave plate. The reflected probe beam was passed through a Wollaston prism which split the probe beam into

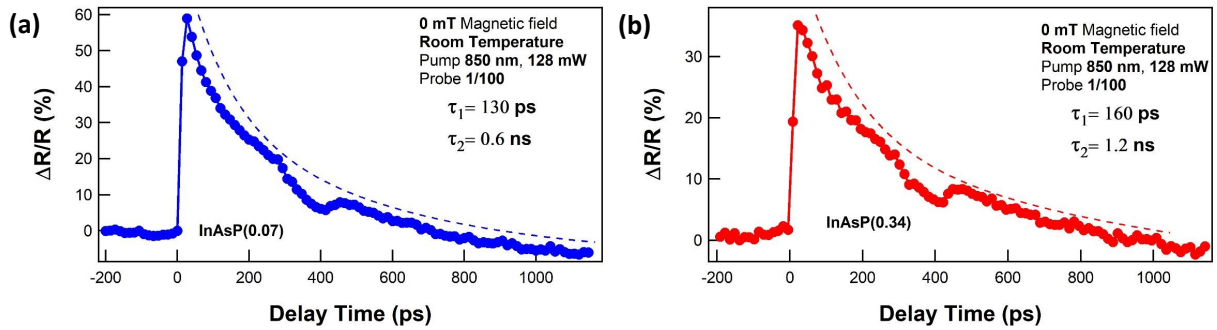

Figure 6.2: Time resolved measurements at 850 nm pump-probe excitations for $InAs_xP_{(1-x)}$ with (a) $x = 0.07$ and (b) $x = 0.34$. In both samples, we observed bumps at 500 ps. Sound velocity in InAs 3.83×10^3 m/s and for InP is $\sim 4.58 \times 10^3$ m/s. Using these values and the thickness of InAsP layer (1.2 μ m), we can conclude the pulses were reflected back at the interface to observe the bumps at 500 ps.

two beams that are perpendicularly polarized to each other. The transient Kerr rotation was detected using Si balanced detector that subtracts the two-beam and feeds into a locking amplifier.

We conducted TRDR measurements on the InAsP films at room temperature, which is displayed in Fig. 6.2. These measurements were taken at 850 nm excitations wavelength for both $InAs_{0.07}P_{0.93}$ and $InAs_{0.34}P_{0.66}$ samples. We modeled the dynamical data with a double exponential fit, where τ_1 is the thermalization time and τ_2 is the recombination time. The two time constants of the $InAs_{0.07}P_{0.93}$ are τ_1= 130 ps and $\tau_2 = 0.6$ ns whereas for $InAs_{0.34}P_{0.66}$ sample τ_1= 160 ps and $\tau_2 = 1.2$ ns. For both the samples, we observed a "bump" in the transient dynamic signal at 500 ps. The sound velocity in InAs is 3.83×10^3m/s and for InP is 4.58×10^3m/s. Thus, we can estimate the sound velocity in InAsP to be 4.20×10^3 m/s. As the time it takes to reach the interface is $t = L/v_s$, where L is the film thickness and v_s is the sound velocity in the sample, we can conclude the pulses were reflected back at the interface to observe the bumps at 500 ps. This abrupt change(bump) was clearly observed only at 850 nm pump-probe. The Fig. 6.3 shows there is no magnetic field dependence in

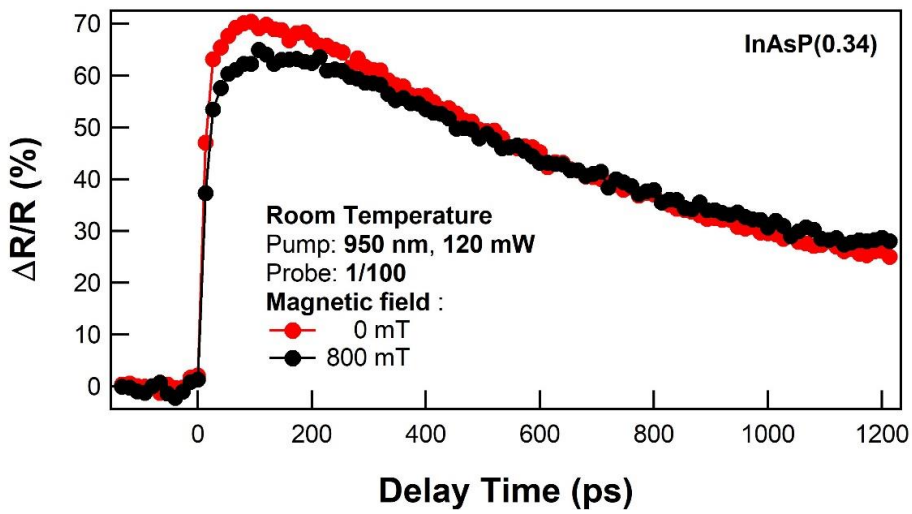

Figure 6.3: Time resolved differential reflectivity at 950 nm with 0 mT and 800 mT magnetic field.

the carrier dynamics.

Figure. 6.4 displays the TRMOKE measurements for the $InAs_{0.34}P_{0.66}$ sample with no external magnetic field. The circularly polarized pump beam selectively excites spin-polarized carriers, following the selection rules. The excited non-equilibrium spin population induce an instantaneous magnetic character (laser-induced magnetism) in the material system. The relaxation of this excited spin population is investigated through a transient Kerr rotation of the linearly polarized probe beam. We observed the change in sign of the Kerr rotation (Fig. 6.4) with the two circularly polarized beams ($+\sigma$ and $-\sigma$), validating that the pump induced spin polarization is dependent on the helicity of the pump beam. We also conducted magnetic field dependent TRMOKE measurements (Fig. 6.5). These measurements were conducted with 950 nm, 128 mW incident pump beam with $-\sigma$ polarization, and with the varied magnetic field from 0-800 mT. We observed an oscillation where the strength of the oscillation increase with the increased in the magnetic field.

We also performed Cyclotron Resonance (CR) measurements at high magnetic fields where

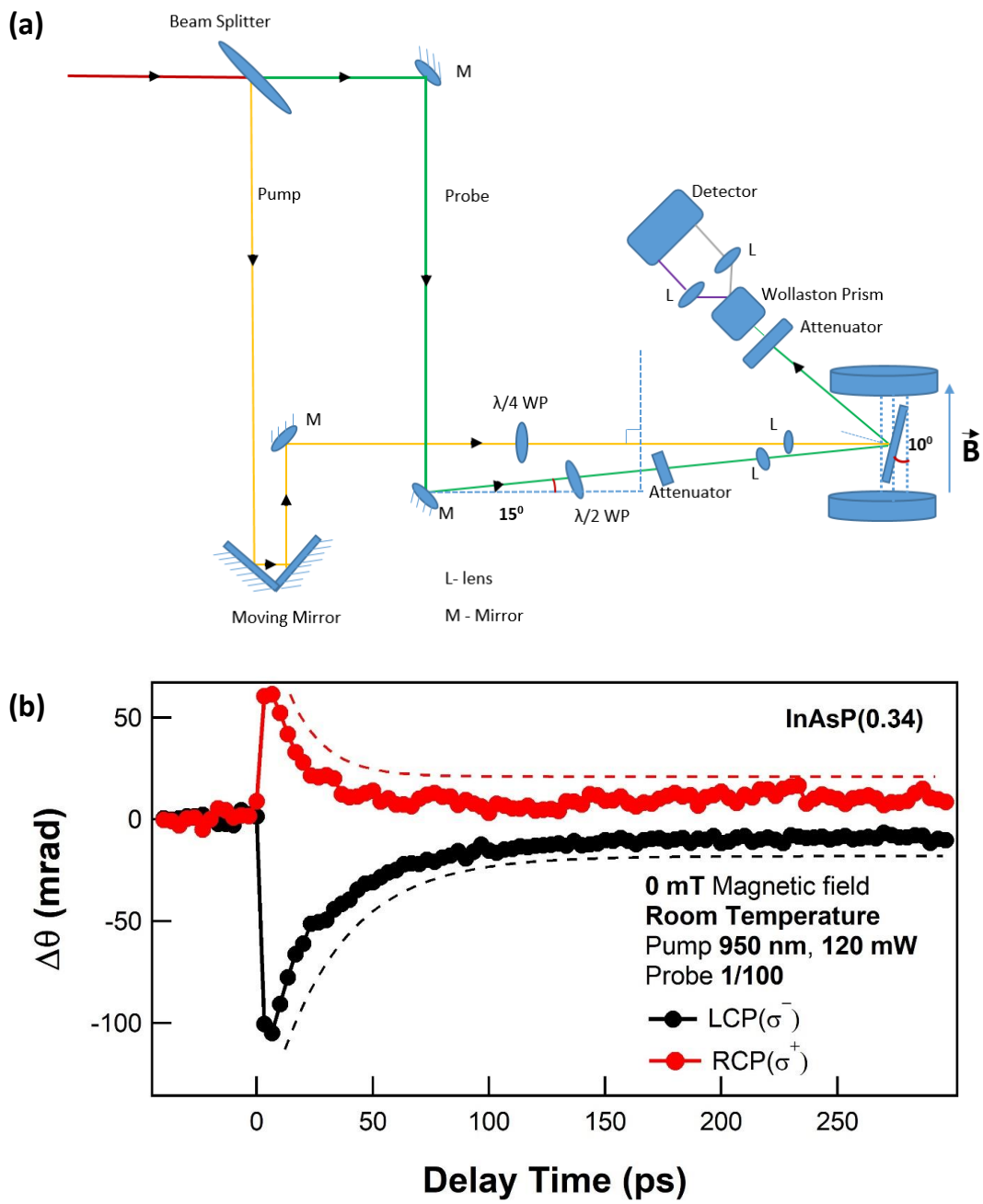

Figure 6.4: (a) Schematic representation of the experimental configuration for the TRMOKE as a function of the field. (b) TRMOKE response of $InAs_{0.34}P_{0.66}$ for two circular polarizations.

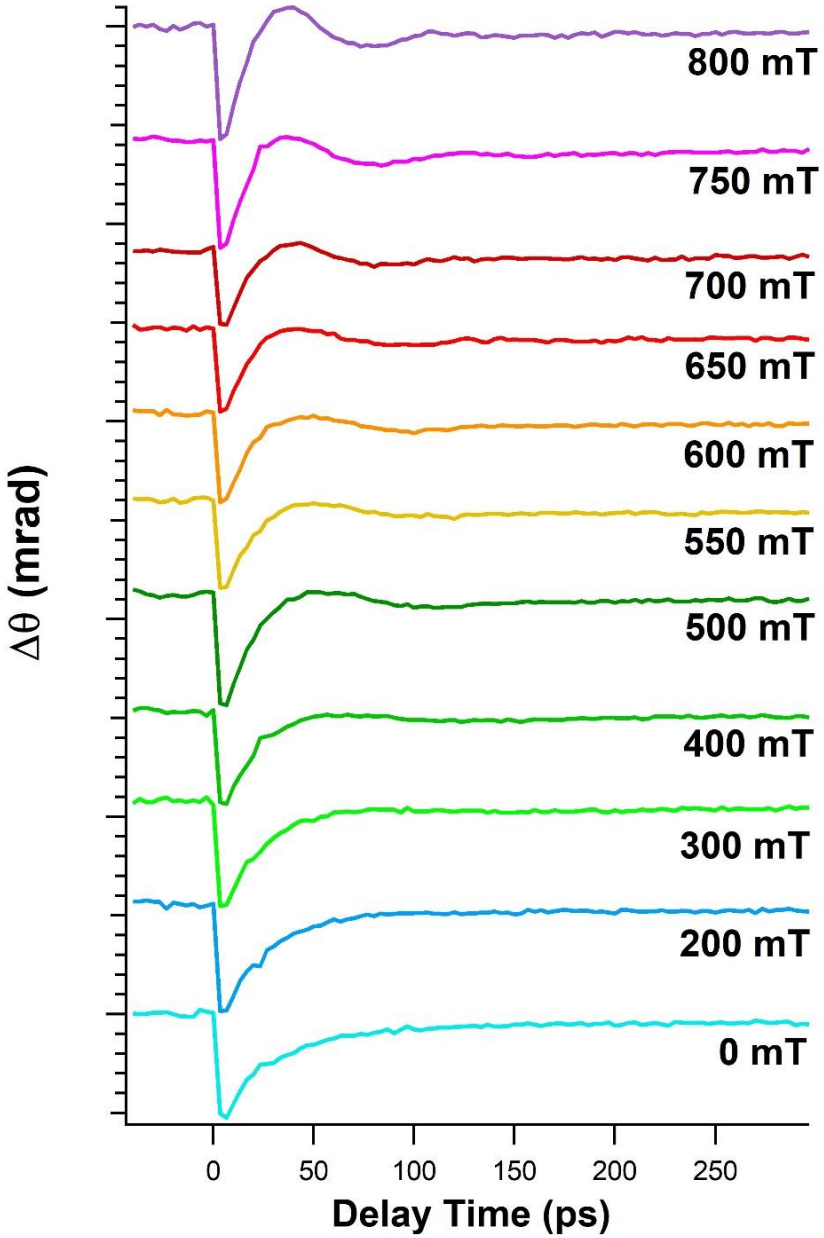

Figure 6.5: TRMOKE at different magnetic fields show the clear signature of precession above 500 mT followed by fast decay in 150 ps. These measurements were taken with 950 nm, 128 mW pump beam with -σ polarization.

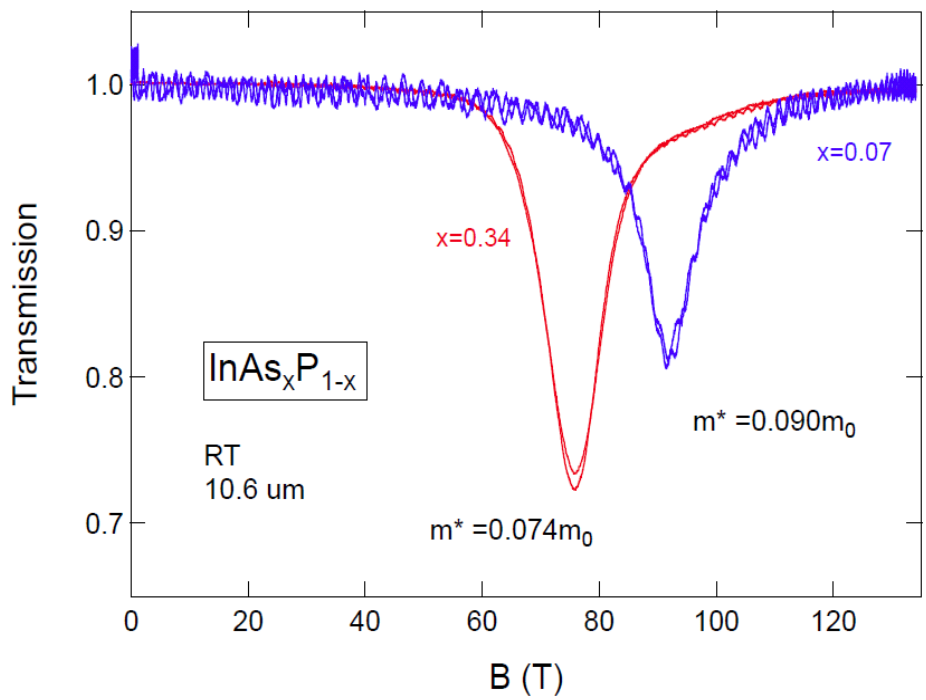

Figure 6.6: High field CR was used to measure the effective mass for the two InAsP alloys. The data was taken sweeping the field up and down.

the field was applied along the growth direction. While the carrier mobility is low, very high magnetic field is necessary to observe CR (i.e., $\omega_c\tau >> 1$) where ω_c is the cyclotron frequency and τ is the scattering time). This condition can be satisfied using a pulsed magnet and a single turn technique. As shown in Fig. 6.6 we measured the effective mass (m*) for both alloys at room temperature. This measurement were taken at the Megagauss facility in Japan in collaboration with Professor Matsuda.

6.4 SHG and Up-conversion Luminescence Measurements of Multiresonant Nanolaminate Plasmonic Crystals

My contribution to this work was conducting photoluminescence measurements to study the SHG and up-conversion luminescence spectrum of these plasmonic structures. Here, I have probed wavelength dependence, incident power dependence, and spectral shape dependence on the emission polarization of these Plasmonic structures.

The recent advances in nanofabrication and optical techniques have opened up promising new avenues for nonlinear optical applications in nanoscale. One such approach to enhance nonlinear light-matter interactions in the subwavelength scale is developing plasmonic nanostructures [265]. A few of the most promising applications of this field includes photodetection, light emission, refractive index sensing, label-free biosensing, and spectroscopy [266, 267, 268, 269, 270]. In this study, we are particularly interested in studying multiresonant nanolaminate plasmonic crystals for tunable delocalized up-conversion intraband luminescence. There are two types of regimes in plasmonic device fabrication, "*single-resonant plasmonics*," and "*multiresonant plasmonics*" [271]. Conventional plasmonic devices are generally single-resonant. However, *multiresonant plasmonic* devices are important for multiband nanophotonics applications [271].

Multiple hybridized modes that are spatially overlapping at different resonant energies can be achieved by assembling multiple plasmonic blocks in a composite system [271]. The spatial mode overlapping in multiresonant plasmonics pose a significant role in several potential and ongoing application, such as multiphoton nonlinear optical and up-conversion luminescence nanodevices. To facilitate this, a simultaneous enhancement of optical excitation and

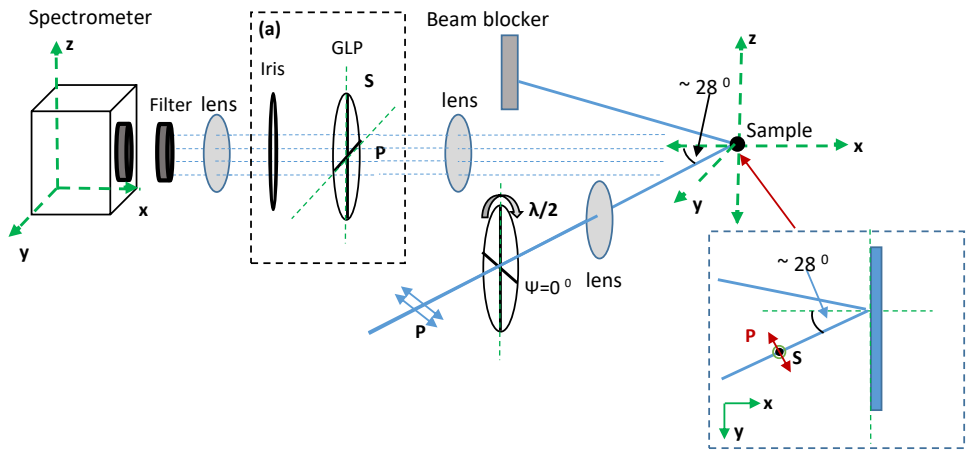

Figure 6.7: Schematic representation of the PL setup that was used to probe SHG and up-conversion luminescence of the plasmonic structures. To probe spectral shape dependence on the emission polarization a polarizer (analyzer) and an iris was introduced to the emission path (a). Note: GLP is Glan Laser polarizer.

radiation processes at multiple different wavelengths, and achieving wavelength-multiplexed optical multimodalities at the nanoscale is important [271].

Our contribution to the project was conducting photoluminescence (PL) measurements to study the second harmonic generation (SHG) and up-conversion luminescence spectrum of these plasmonic structures. We have probed wavelength dependence (960-1040 nm), incident power dependence (0-128 mW), and spectral shape dependence on the emission polarization ($0^0 - 360^0$) of these structures. These measurements were taken at room temperature with spectrometer configuration 0.15 mm slit size and a 120 sec exposure time. The sample was mounted parallel to the collection plane and laser spot size at the sample was $\sim$ 1 mm in diameter (Fig. 6.7). The laser source was a Coherent Chameleon Ti:Sapphire laser with a repetition rate of 80 MHz, a wavelength range of 700-1050 nm, and a pulse duration of 100 fs. The PL was measured using the iHR550 spectrometer with an LN_2 cooled Symphony

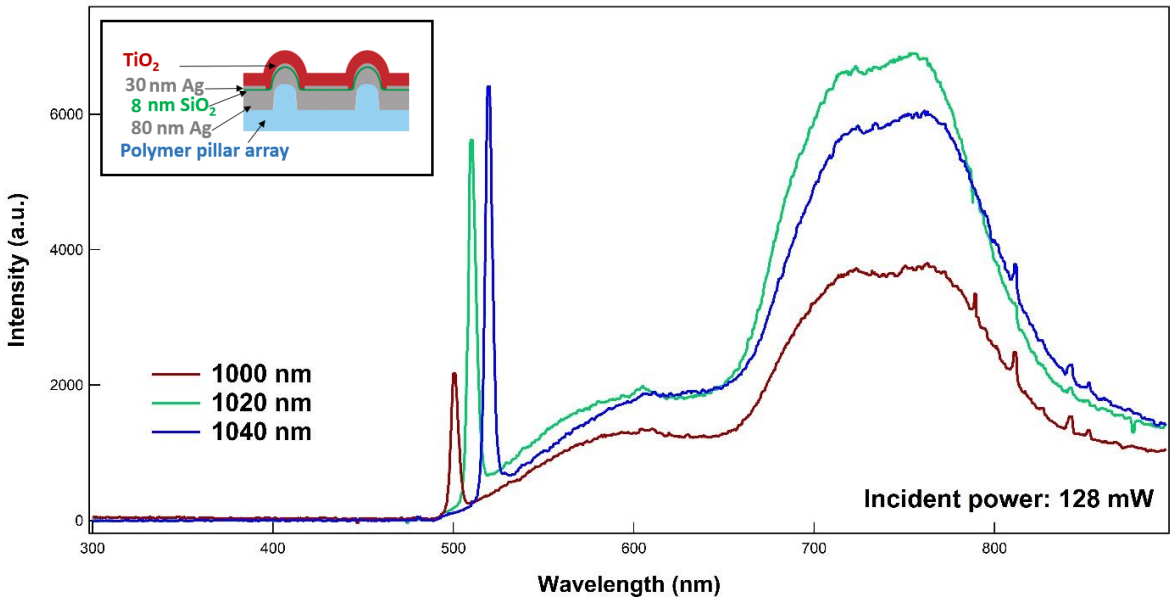

Figure 6.8: SHG and up-conversion luminescence spectrum for 1000, 1020, and 1040 nm, 128 mW, and P polarized incident beam. The inset shows the material structure where the TiO_2 thickness for this sample is 150 nm (Three samples with variable TiO_2 thickness (20, 60, and 130 nm) were studied in this project).

II CCD detector. The incident polarization was rotated via a Thorlabs Half-Wave Liquid Crystal Variable Retarder/Wave Plate (Thorlabs; LCC1221-B), where we probed both S and P incident beam configurations where S is referring to the polarization perpendicular to the plane of incidence beam and P is for the polarization parallel to the plane of incidence. The spectral shape variation of the structures (in both SHG and up-conversion luminescence) was probed as a function of emission polarization. For this measurement, we used a Thorlab Glan-Laser Calcite Polarizer (Thorlab: GL5-B) where we placed the polarizer after the collection lens (collimating lenses: Fig. 6.7) to resolve the polarization of the emission spectrum. Figure 6.8 displays the SHG and up-conversion luminescence spectrum we observed for the structure with 150 nm TiO_2 layer.

Chapter 7

Summary and Future Works

In this dissertation, I have discussed investigations focused on employing ultrafast nonlinear magneto-optical spectroscopic techniques to study newly developed material structures such as multiferroic BTO-BFO, ferroelectric PZT, InAs/AlAsSb multi-quantum-well structures, Methyl-ammonium lead halide perovskite, InAsP films, and multiresonant nanolaminate plasmonic crystals.

Investigations on multiferroic BTO-BFO have been discussed in Chapters 3 and 4. These studies provided insights into the ultrafast and nonlinear properties of less explored materials systems. This project was focused on observing and investigating coherent states such as CAP and magnons in these structures. In the first part of this study, as discussed in Chapter 3 we conducted TRDR measurements at room temperature and at 100 K for BTO-BFO films (different thicknesses) and nanorod structures. The quantitative study of ultrafast carrier dynamics in BTO-BFO describes the diffusion of the photoexcited carriers away from the surface where the ambipolar diffusion constant is below 1-2 cm^2/s. I have also discussed the observations of CAP in both film and nanorod samples at lower temperatures (100 K). The estimated CAP frequency was found to be $\sim$ 27 GHz in a 660 nm thick structure. In the nanorod arrays, two frequencies were observed, a frequency of $\sim$ 33 GHz and a lower one of $\sim$ 8.1 GHz. The higher frequency oscillations are attributed to be coherent acoustic phonons. The lower frequency is close to a theoretically predicted magnon frequency in BFO. As the strength of this oscillation only had a very weak magnetic field dependence,

these oscillations could also be due to multiple reflections of the acoustic phonons at the Pt interfaces owing to the large acoustic impedance mismatch.

Chapter 4 discusses the magnetic field dependence of Coherent Acoustic Phonons (CAP) measured by TROIB and TRMOKE. Here, we were able to demonstrate that CAP oscillations observed through these techniques have a higher sensitivity to the external magnetic fields compared to the transient reflectivity reported on the same structure, under the exact experimental conditions, in Chapter 3. I also discussed the observation of SHG in BTO-BFO in this chapter. These strong SHG signals are generated as a result of the non-centrosymmetric nature of the material. SHG is a widely used technique to investigate the underlying symmetry of material structures. Our polarization-dependent SHG measurements portrayed a complicated polar symmetry. We associated this with the poly-crystalline nature of the BTO-BFO thin films.

Multiferroic BTO-BFO are potential candidates for multifunctional devices, but there is still more scope to investigate and improve. For instance, in the nanorod sample, we observe the low-frequency oscillation that has a debatable origin. I have discussed two explanations for the origin of these low-frequency oscillations: (1) magnons, (2) multiple reflections off of the Pt layer due to the acoustic mismatch between the two layers. One of the steps forward to investigate the origin of these oscillations is to fabricate nanorod structures with different substrates that have similar acoustic impedance as the BTO-BFO/LSMO. Thus we can reduce the multiple reflections of the propagating CAP at the Pt interface. In BFO the inherent magnetization is suppressed by the spiral spin structure. By applying a high magnetic field, in case of low dimensional structures such as nanorods, where the dimensions are less than the periodicity of the spiral spin structures, and the inherent magnetization can be released. Moreover, magnetic character in BFO can also be enhanced by introducing strain. Another possible future path would be to develop lower dimensional structures like

quantum dots to enhance the magnetic character and thus enhance the magnetoelectric coupling in BTO-BFO structures.

Our observation of CAPs which are propagating strain pulses, can be triggered with ultrafast optical pulses. Our results suggest that using ultrafast optical pulse techniques offers a potentially better means of generating the dynamic strain pulses that can bypass the need to fabricate a Surface Acoustic Wave (SAW) device and allow for higher frequencies and faster manipulation. Thus, this experimental technique can be used to investigate material structures that can be potentially used in CAP applications. Recently, phonon interaction with spin has gained increased attention in long-range spin transport applications where it has been demonstrated in a recent publication that magnetization dynamics can be controlled through magnetoelastic effect [272, 273]. The elastic deformation arising from the propagating strain pulse could be a new approach to alter the magnetic properties of a media. Thus, these investigations can be further broadened to study newly engineered materials with enhanced properties such as magnetoelectric and magnetoelastic coupling.

The 5th chapter focuses on the investigations of optical properties of PZT nanorods. Here, we have conducted SHG and TRDR measurements using polycrystalline nanorods of PZT. The SHG results suggest that PZT nanorod structures have an enhanced SHG response compared to thin-film structures. The room temperature SHG in PZT shows quadratic power, indicating the observations are from the SHG process. In the case of TRDR measurements, we employed both non-degenerate (two-color) and degenerate pump-probe configurations, allowing us to investigate the carrier dynamics, both close to the bandgap (3.4 eV), as well as through multiphoton processes. In a multiphoton process, the transient effects are typically near the surface thus the relaxation processes can be dominated by heat diffusion. TRDR measurements on PZT nanorods displayed strong dependence on the excitation wavelengths, with variations in amplitudes, a significant change in the $\Delta R/R$, as well as decay times.

PZT is a well-established material in electroceramics that has a wide variety of applications with enhanced ferroelectric, piezoelectric, and photovoltaic properties. Having a better fundamental understanding of carrier dynamics and nonlinear optical properties of PZT would open up more avenues for using PZT in the optoelectronic industry. In this study we observe a difference in the intensity of unpoled and poled PZT nanorod samples which we associate with the macroscopic effects. Studies can be conducted to investigate the microscopic differences in these structures. In order to investigate the microscopic effects of poling properties on the nonlinear properties of PZT structure, near-field second-harmonic spectroscopy would be required [274].

Through material engineering, we can also fabricate materials with improved properties for higher efficiency and have better control of nonlinear properties like SHG. One such widely used technique is strain engineering. SHG manipulation in solids using strain has been theoretically modeled [275, 276] and also has been experimentally applied in semiconductor systems [277] and transition metal dichalcogenides [210]. Strain engineering can also be applied to material structures I have studied in this dissertation (PZT and BTO-BFO nanorods) to control the SHG generation.

Apart from strain, SHG can also be controlled through the application of external fields. SHG can be observed in both centrosymmetric and non-centrosymmetric materials because magnetic ordering break the inversion symmetry. Magnetic-second-harmonic generation in magnetically ordered dielectrics has been observed and successfully applied as a useful tool for studying electronic and magnetic properties [278, 279]. It is expected that the second-order optical nonlinearity is enhanced when magnetic and ferroelectric orderings are strongly coupled. Multiple experimental studies have been conducted to study the magnetic field-induced change in SHG (MSHG). An external magnetic field can influence the SHG response by altering the material's underlying symmetry [28, 280], by strengthening single domain

states [281], and also by inducing a phase change [282, 283]. Similarly, we can employ an external magnetic field to organize and enhance the un-pinned AFM domains at the edges of multiferroic BT-BFO nanostructures [284] to control the SHG emission from that material.

Bibliography

[1] J Hemminger, G Fleming, and M Ratner. Directing matter and energy: Five challenges for science and the imagination. United States:N.p., 2007.

[2] Rathsara R. H. H. Mudiyanselage, Brenden A. Magill, John Burton, Moira Miller, Joseph Spencer, Kiara McMillan, Giti A. Khodaparast, Han Byul Kang, Min Gyu Kang, Deepam Maurya, Shashank Priya, Jade Holleman, Steve McGill, and Christoh-per J. Stanton. Coherent acoustic phonons and ultrafast carrier dynamics in hetero-epitaxial batio3–bifeo3 films and nanorods. *J. Mater. Chem. C*, 7:14212–14222, 2019.

[3] V R Whiteside, B A Magill, Matthew P Lumb, H Esmaielpour, M A Meeker, R R H H Mudiyanselage, A Messager, S Vijeyaragunathan, T D Mishima, M B Santos, I Vurgaftman, G A Khodaparast, and I R Sellers. *Semiconductor Science and Technology*, 34(2):025005, 2019.

[4] Congcong Wu, Haijin Li, Yongke Yan, Bo Chi, Kristen M. Felice, Robert B. Moore, Brenden A. Magill, Rathsara R. H. H. Mudiyanselage, Giti A. Khodaparast, Mohan Sanghadasa, and Shashank Priya. *Solar RRL*, 2(6):1800052, 2018.

[5] M. A. Meeker, B. A. Magill, T. R. Merritt, M. Bhowmick, K. McCutcheon, G. A. Khodaparast, J. G. Tischler, S. McGill, S. G. Choi, and C. J. Palmstrøm. *Applied Physics Letters*, 102(22):222102, 2013.

[6] T. R. Merritt, M. A. Meeker, B. A. Magill, G. A. Khodaparast, S. McGill, J. G. Tischler, S. G. Choi, and C. J. Palmstrøm. Photoluminescence lineshape and dynamics of localized excitonic transitions in inasp epitaxial layers. *Journal of Applied Physics*, 115(19):193503, 2014.

[7] Seied Ali Safiabadi Tali, Junyeob Song, Wonil Nam, and Wei Zhou. *Advanced Optical Materials*, (2001908: doi.org/10.1002/adom.202001908), 2021.

[8] Maria Čebela, Dejan Zagorac, Katarina Batalović, Jana Radaković, Bojan Stojadinović, Vojislav Spasojević, and Radmila Hercigonja. *Ceramics International*, 43(1, Part B):1256 – 1264, 2017.

[9] S.-C. Yang, A. Kumar, V. Petkov, and S. Priya. *J. of Appl. Phys*, 113:144101, 2013.

[10] Brenden A. Magill, Sunil Thapa, Jade Holleman, Stephen McGill, Hiro Munekata, Christopher J. Stanton, and Giti A. Khodaparast. *Phys. Rev. B*, 102:045306, 2020.

[11] F. Godejohann, A. V. Scherbakov, S. M. Kukhtaruk, A. N. Poddubny, D. D. Yaremkevich, M. Wang, A. Nadzeyka, D. R. Yakovlev, A. W. Rushforth, A. V. Akimov, and M. Bayer. *Phys. Rev. B*, 102:144438, 2020.

[12] Rathsara R. H. H. Mudiyanselage, John Burton, Brenden A. Magill, Kiara McMillan, GabiGagliano, Ada J. Morral, Han-Byul Kang Min Gyu Kang, Shashank Priya, ChristopherJ. Stanton, and Giti A. Khodaparast. *Under review*, 2021.

[13] Guido Burkard, Hans-Andreas Engel, and Daniel Loss. *Fortschritte der Physik*, 48(9-11):965–986, 2000.

[14] S. A. Wolf, D. D. Awschalom, R. A. Buhrman, J. M. Daughton, S. von Molnár, M. L. Roukes, A. Y. Chtchelkanova, and D. M. Treger. 294(5546):1488–1495, 2001.

[15] D. Awschalom, N. Samarth, and D. Loss. *Semiconductor spintronics and quantum computation*. Springer, 2011.

[16] Nicola A. Spaldin and Manfred Fiebig. *Science*, 309(5733):391–392, 2005.

[17] Ying-Hao Chu, Lane W. Martin, Mikel B. Holcomb, and Ramamoorthy Ramesh. *Materials Today*, 10(10):16–23, 2007.

[18] D. Lebeugle, D. Colson, A. Forget, M. Viret, A. M. Bataille, and A. Gukasov. *Phys. Rev. Lett.*, 100:227602, 2008.

[19] Joseph R. Demers Nathan P. Wells, Paul M. Belden and William T. Lotshaw. *J. Appl. Phys.*, 116:073506, 2014.

[20] A. K. Axelsson N. M. Alford K. I. Doig, F. Aguesse, S. Nawaz, V. R. Palkar, S. P. P. Jones, R. D. Johnson, R. A. Synowicki, and J. Lloyd-Hughes. *Phys. Rev. B: Condens. Matter Mater. Phys.*, 88:094425, 2013.

[21] S.D. Bader and S.S.P. Parkin. *Annual Review of Condensed Matter Physics*, 1(1):71–88, 2010.

[22] G. S. Kino. Acoustic imaging for nondestructive evaluation. *Proceedings of the IEEE*, 67(4):510–525, 1979.

[23] N. D. Lanzillotti-Kimura, A. Fainstein, A. Lemaitre, B. Jusserand, and B. Perrin. *Phys. Rev. B*, 84:115453, 2011.

[24] J. M. Dolan D. W. Bailey S. Zollner, K. D. Myers and C. J. Stanton. *Thin Solid Films*, 568:313–314, 1998.

[25] M. Bhowmick, G. A. Khodaparast, T. D. Mishima, M. B. Santos, D. Saha, G. Sanders, and C. J. Stanton. *Journal of Applied Physics*, 120(23):235702, 2016.

[26] P. A. Franken, A. E. Hill, C. W. Peters, and G. Weinreich. *Phys. Rev. Lett.*, 7:118–119, 1961.

[27] Robert M. Corn and Daniel A. Higgins. *Chemical Reviews*, 94(1):107–125, 1994.

[28] V. V. Pavlov, A. M. Kalashnikova, R. V. Pisarev, I. Sänger, D. R. Yakovlev, and M. Bayer. *Phys. Rev. Lett.*, 94:157404, 2005.

[29] Jérémy Butet, Pierre-François Brevet, and Olivier J. F. Martin. *ACS Nano*, 9(11):10545–10562, 2015.

[30] M. Lafrentz, D. Brunne, B. Kaminski, V. V. Pavlov, A. V. Rodina, R. V. Pisarev, D. R. Yakovlev, A. Bakin, and M. Bayer. *Phys. Rev. Lett.*, 110:116402, 2013.

[31] Leandro M. Malard, Thonimar V. Alencar, Ana Paula M. Barboza, Kin Fai Mak, and Ana M. de Paula. *Phys. Rev. B*, 87:201401, 2013.

[32] B. Kaminski, M. Lafrentz, R. V. Pisarev, D. R. Yakovlev, V. V. Pavlov, V. A. Lukoshkin, A. B. Henriques, G. Springholz, G. Bauer, E. Abramof, P. H. O. Rappl, and M. Bayer. *Phys. Rev. Lett.*, 103:057203, 2009.

[33] P. J. Campagnola, M. D. Wei, A. Lewis, and L. M. Loew. *Biophysical journal*, 77(6):3341–3349, 1999.

[34] X. Zhuang, P. B. Miranda, D. Kim, and Y. R. Shen. *Phys. Rev. B*, 59:12632–12640, 1999.

[35] Ursula Keller. *Nature*, 424(6950):831–838, 2003.

[36] C. Manzoni, G. Cirmi, D. Brida, S. De Silvestri, and G. Cerullo. *Phys. Rev. A*, 79:033818, 2009.

[37] R. Baumgartner and R. Byer. *IEEE Journal of Quantum Electronics*, 15(6):432–444, 1979.

[38] Wei Li, Bigeng Chen, Chao Meng, Wei Fang, Yao Xiao, Xiyuan Li, Zhifang Hu, Yingxin Xu, Limin Tong, Hongqing Wang, Weitao Liu, Jiming Bao, and Y. Ron Shen. *Nano Letters*, 14(2):955–959, 2014.

[39] Sophie Schönenberger, Thilo Stöferle, Nikolaj Moll, Rainer F. Mahrt, Marcus S. Dahlem, Thorsten Wahlbrink, Jens Bolten, Thomas Mollenhauer, Heinrich Kurz, and Bert J. Offrein. *Opt. Express*, 18(21):22485–22496, 2010.

[40] Paresh Chandra Ray. *Chemical Reviews*, 110(9):5332–5365, 2010.

[41] A. Bruchhausen, R. Gebs, F. Hudert, D. Issenmann, G. Klatt, A. Bartels, O. Schecker, R. Waitz, A. Erbe, E. Scheer, J.-R. Huntzinger, A. Mlayah, and T. Dekorsy. *Phys. Rev. Lett.*, 106:077401, 2011.

[42] M. P. Hasselbeck, D. Stalnaker, L. A. Schlie, T. J. Rotter, A. Stintz, and M. Sheik-Bahae. *Phys. Rev. B*, 65:233203, 2002.

[43] Paul C. M. Planken, Martin C. Nuss, Igal Brener, Keith W. Goossen, Marie S. C. Luo, Shun Lien Chuang, and Loren Pfeiffer. *Phys. Rev. Lett.*, 69:3800–3803, 1992.

[44] B. B. Hu, X.-C. Zhang, and D. H. Auston. *Phys. Rev. Lett.*, 67:2709–2712, 1991.

[45] C.J Stanton, G.D Sanders, R Liu, G.W Chern, C.-K Sun, J.S Yahng, Y.D Jho, J.Y Sohn, E Oh, and D.S Kim. *Superlattices and Microstructures*, 34(3):525 – 529, 2003.

[46] E. Makarona, B. Daly, J.-S. Im, H. Maris, A. Nurmikko, and Jung Han. *Applied Physics Letters*, 81(15):2791–2793, 2002.

[47] P. Ruello, T. Pezeril, S. Avanesyan, G. Vaudel, V. Gusev, I. C. Infante, and B. Dkhil. *Applied Physics Letters*, 100(21):212906, 2012.

[48] Mariusz Lejman, Gwenaelle Vaudel, Ingrid C. Infante, Pascale Gemeiner, Vitalyi E. Gusev, Brahim Dkhil, and Pascal Ruello. *Nature Communications*, 5(1):4301, 2014.

[49] T. Saito, O. Matsuda, and O. B. Wright. *Phys. Rev. B*, 67:205421, 2003.

[50] O. B. Wright, B. Perrin, O. Matsuda, and V. E. Gusev. *Phys. Rev. B*, 64:081202, 2001.

[51] P. Babilotte, P. Ruello, D. Mounier, T. Pezeril, G. Vaudel, M. Edely, J-M. Breteau, V. Gusev, and K. Blary. *Phys. Rev. B*, 81:245207, 2010.

[52] T. Saito, O. Matsuda, and O. B. Wright. *Phys. Rev. B*, 67:205421, 2003.

[53] A. Huynh, B. Perrin, N. D. Lanzillotti-Kimura, B. Jusserand, A. Fainstein, and A. Lemaître. Subterahertz monochromatic acoustic wave propagation using semiconductor superlattices as transducers. *Phys. Rev. B*, 78:233302, 2008.

[54] O. Matsuda, T. Tachizaki, T. Fukui, J. J. Baumberg, and O. B. Wright. *Phys. Rev. B*, 71:115330, 2005.

[55] Emmanuel Péronne, Eric Charron, Serge Vincent, Sébastien Sauvage, Aristide Lemaître, Bernard Perrin, and Bernard Jusserand. *Applied Physics Letters*, 102(4):043107, 2013.

[56] Yu-Chieh Wen, Tsung-Shine Ko, Tien-Chang Lu, Hao-Chung Kuo, Jen-Inn Chyi, and Chi-Kuang Sun. *Phys. Rev. B*, 80:195201, 2009.

[57] G. Pernot, M. Stoffel, I. Savic, F. Pezzoli, P. Chen, G. Savelli, A. Jacquot, J. Schumann, U. Denker, I. Mönch, Ch. Deneke, O. G. Schmidt, J. M. Rampnoux, S. Wang, M. Plissonnier, A. Rastelli, S. Dilhaire, and N. Mingo. *Nature Materials*, 9(6):491–495, 2010.

[58] Jen-Kan Yu, Slobodan Mitrovic, Douglas Tham, Joseph Varghese, and James R. Heath. *Nature Nanotechnology*, 5(10):718–721.

[59] Ivan S. Grudinin, Hansuek Lee, O. Painter, and Kerry J. Vahala. *Phys. Rev. Lett.*, 104:083901, 2010.

[60] R. P. Beardsley, A. V. Akimov, M. Henini, and A. J. Kent. *Phys. Rev. Lett.*, 104:085501, 2010.

[61] A. Fainstein, N. D. Lanzillotti-Kimura, B. Jusserand, and B. Perrin. *Phys. Rev. Lett.*, 110:037403, 2013.

[62] T. J. Kippenberg and K. J. Vahala. *Science*, 321(5893):1172–1176.

[63] Rusko Ruskov and Charles Tahan. *Journal of Physics: Conference Series*, 398:012011, 2012.

[64] J. D. Teufel, T. Donner, Dale Li, J. W. Harlow, M. S. Allman, K. Cicak, A. J. Sirois, J. D. Whittaker, K. W. Lehnert, and R. W. Simmonds. *Nature*, 475(7356):359–363.

[65] Jasper Chan, T. P. Mayer Alegre, Amir H. Safavi-Naeini, Jeff T. Hill, Alex Krause, Simon Gröblacher, Markus Aspelmeyer, and Oskar Painter. *Nature*, 478(7367):89–92, 2011.

[66] Matt Eichenfield, Jasper Chan, Ryan M. Camacho, Kerry J. Vahala, and Oskar Painter. *Nature*, 462(7269):78–82, 2009.

[67] A. D. O'Connell, M. Hofheinz, M. Ansmann, Radoslaw C. Bialczak, M. Lenander, Erik Lucero, M. Neeley, D. Sank, H. Wang, M. Weides, J. Wenner, John M. Martinis, and A. N. Cleland. *Nature*, 464(7289):697–703, 2010.

[68] S. Kolkowitz, A. C. Bleszynski Jayich, Q. P. Unterreithmeier, S. D. Bennett, P. Rabl, J. G. E. Harris, and M. D. Lukin. *Science*, 335(6076):1603–1606, 2012.

[69] Meng Gao, Hubert Jean-Ruel, Ryan R. Cooney, Jonathan Stampe, Mark de Jong, Maher Harb, German Sciaini, Gustavo Moriena, and R. J. Dwayne Miller. *Optics Express*, 20(11):12048, 2012.

[70] O. Matsuda, O. B. Wright, D. H. Hurley, V. E. Gusev, and K. Shimizu. *Phys. Rev. Lett.*, 93:095501, 2004.

[71] S. M. Komirenko, K. W. Kim, A. A. Demidenko, V. A. Kochelap, and M. A. Stroscio. 90(8):3934–3941, 2001.

[72] Kung-Hsuan Lin, Chih-Ming Lai, Chang-Chi Pan, Jen-Inn Chyi, Jin-Wei Shi, Shih-Ze Sun, Chieh-Feng Chang, and Chi-Kuang Sun. *Nature Nanotechnology*, 2(11):704–708, 2007.

[73] Samuel J. Whiteley, Gary Wolfowicz, Christopher P. Anderson, Alexandre Bourassa, He Ma, Meng Ye, Gerwin Koolstra, Kevin J. Satzinger, Martin V. Holt, F. Joseph Heremans, Andrew N. Cleland, David I. Schuster, Giulia Galli, and David D. Awschalom. *Nature Physics*, 15(5):490–495, 2019.

[74] Cassidy Berk, Mike Jaris, Weigang Yang, Scott Dhuey, Stefano Cabrini, and Holger Schmidt. *Nature Communications*, 10(1):2652, 2019.

[75] P. Rovillain, R. de Sousa, Y. Gallais, A. Sacuto, M. A. Méasson, D. Colson, A. Forget, M. Bibes, A. Barthélémy, and M. Cazayous. *Nature Materials*, 9(12):975–979, 2010.

[76] Roman Khymyn, Ivan Lisenkov, Vasyl Tiberkevich, Boris A. Ivanov, and Andrei Slavin. *Scientific Reports*, 7(1), 2017.

[77] Andrii V. Chumak, Alexander A. Serga, and Burkard Hillebrands. *Nature Communications*, 5(1):4700, 2014.

[78] A A Serga, A V Chumak, and B Hillebrands. *Journal of Physics D: Applied Physics*, 43(26):264002, 2010.

[79] A. V. Chumak, V. I. Vasyuchka, A. A. Serga, and B. Hillebrands. *Nature Physics*, 11(6):453–461, 2015.

[80] W. Eerenstein, N. D. Mathur, and J. F. Scott. *Nature*, 442(7104):759–765, 2006.

[81] Paula Vilarinho. *Scanning Probe Microscopy: Characterization, Nanofabrication and Device Application of Functional Materials*, 186:3–33, 2005.

[82] Jordan E. Massad and Ralph C. Smith. *Journal of Intelligent Material Systems and Structures*, 14(7):455–471, 2003.

[83] Hans Schmid. *Ferroelectrics*, 162(1):317–338, 1994.

[84] Jia-Mian Hu, Zheng Li, Long-Qing Chen, and Ce-Wen Nan. *Nature Communications*, 2(1):553, 2011.

[85] Dariusz Bochenek and Zygmunt Surowiak. *Archives of Acoustics*, 33:243–260, 01 2008.

[86] M. Ye. Zhuravlev, S. Maekawa, and E. Y. Tsymbal. *Phys. Rev. B*, 81:104419, 2010.

[87] Melvin M. Vopson. *Critical Reviews in Solid State and Materials Sciences*, 40(4):223–250, 2015.

[88] L. Mitoseriu, M. Viviani, M.T. Buscaglia, Vincenzo Buscaglia, and P. Nanni. *Journal of Optoelectronics and Advanced Materials*, 10:2373–2379, 2008.

[89] Tae-Jin Park, Georgia C. Papaefthymiou, Arthur J. Viescas, Yongjae Lee, Hongjun Zhou, and Stanislaus S. Wong. *Phys. Rev. B*, 82:024431, 2010.

[90] Claude Ederer and Nicola A. Spaldin. *Phys. Rev. B*, 71:060401, 2005.

[91] R. Safi and H. Shokrollahi. *Progress in Solid State Chemistry*, 40(1):6 – 15, 2012.

[92] S. S. Krotov D. V. Belov G. P. Vorobév P. N. Makhov Y. F. Popov, A. M. Kadomtseva and A. K. Zvezdin. *Low Temp. Phys.*, 27:478, 2001.

[93] Su-Chul Yang, Ashok Kumar, Valeri Petkov, and Shashank Priya. *Journal of Applied Physics*, 113(14):144101, 2013.

[94] C. Thomsen, J. Strait, Z. Vardeny, H. J. Maris, J. Tauc, and J. J. Hauser. *Phys. Rev. Lett.*, 53:989–992, 1984.

[95] Andrey Baydin, Rustam Gatamov, Halina Krzyzanowska, Christopher J. Stanton, and Norman Tolk. *Phys. Rev. B*, 99:165202, 2019.

[96] H. P. Weber. *Journal of Applied Physics*, 38(5):2231–2234, 1967.

[97] Ursula Keller. *Nature*, 424(6950):831–838, 2003.

[98] G. Steinmeyer, D. H. Sutter, L. Gallmann, N. Matuschek, and U. Keller. *Science*, 286(5444):1507–1512, 1999.

[99] J. Y. Zhang, J. Y. Huang, Y. R. Shen, and C. Chen. *J. Opt. Soc. Am. B*, 10(9):1758–1764, 1993.

[100] Wei Li, Bigeng Chen, Chao Meng, Wei Fang, Yao Xiao, Xiyuan Li, Zhifang Hu, Yingxin Xu, Limin Tong, Hongqing Wang, Weitao Liu, Jiming Bao, and Y. Ron Shen. *Nano Letters*, 14(2):955–959, 2014.

[101] H S Tzou and C-S Chou. *Smart Materials and Structures*, 5(2):230–235, 1996.

[102] Zhen Chai, Xiaoyong Hu, Feifan Wang, Xinxiang Niu, Jingya Xie, and Qihuang Gong. *Advanced Optical Materials*, 5(7):1600665, 2017.

[103] T. N. Narayanan, B. P. Mandal, A. K. Tyagi, A. Kumarasiri, Xaiobo Zhan, Myung Gwan Hahm, M. R. Anantharaman, G. Lawes, and P. M. Ajayan. *Nano Letters*, 12(6):3025–3030, 2012.

[104] Anuja Datta, Devajyoti Mukherjee, Mahesh Hordagoda, Sarath Witanachchi, Pritish Mukherjee, Ranjit V. Kashid, Mahendra A. More, Dilip S. Joag, and Padmakar G. Chavan. *ACS Applied Materials & Interfaces*, 5(13), 2013.

[105] Su Chul Yang, Mohan Sanghadasa, and Shashank Priya. *Nanotechnology*, 24(22):225303, may 2013.

[106] Sheng Xu, Benjamin J. Hansen, and Zhong Lin Wang. *Nature Communications*, 1(1):93, Oct 2010.

[107] Dragan Damjanovic. *Reports on Progress in Physics*, 61(9):1267–1324, 1998.

[108] Daisuke Takamuro, Hidekuni Takao, Kazuaki Sawada, and Makoto Ishida. *Sensors and Actuators A: Physical*, 114(2):230 – 235, 2004.

[109] Mohamed T. Ghoneim, Mohammed A. Zidan, Mohammed Y. Alnassar, Amir N. Hanna, Jurgen Kosel, Khaled N. Salama, and Muhammad M. Hussain. *Advanced Electronic Materials*, 1(6):1500045, 2015.

[110] Min Gyu Kang, Seul-Yi Lee, Deepam Maurya, Christopher Winkler, Hyun-Cheol Song, Robert B. Moore, Mohan Sanghadasa, and Shashank Priya. *Advanced Functional Materials*, 27:1701542, 2017.

[111] Sava A. Denev, Tom T. A. Lummen, Eftihia Barnes, Amit Kumar, and Venkatraman Gopalan. *Journal of the American Ceramic Society*, 94(9):2699–2727, 2011.

[112] M. Baudrier-Raybaut, R. Haïdar, Ph. Lemasson Ph. Kupecek, and E.Rosencher. *Nature*, 432:3745, 2004.

[113] Sergey E. Skipetrov. *Nature*, 432(7015):285, 2004.

[114] J. Shah. *Ultrafast spectroscopy of semiconductors and semiconductor nanostructures*. Springer, 1999.

[115] C. J. Cook, S. Khan, G. D. Sanders, X. Wang, D. H. Reitze, Y. D. Jho, Y.-W. Heo, J.-M. Erie, D. P. Norton, and C. J. Stanton. In Ferechteh Hosseini Teherani, David C. Look, Cole W. Litton, and David J. Rogers, editors, *Oxide-based Materials and Devices*, volume 7603, pages 23 – 36. International Society for Optics and Photonics, SPIE, 2010.

[116] G. D. Sanders X. Wang D. H. Reitze Y. D. Jhod Y.-W. Heoe J.-M. Eriee D. P. Nortone C. J. Cook, S. Khan and C. J. Stanton. *Proc. of SPIE*, 7603:760304, 2010.

[117] R Wilks, N D Hughes, and R J Hicken. *Journal of Physics: Condensed Matter*, 15(29):5129–5143, 2003.

[118] John Kerr LL.D. *The London, Edinburgh, and Dublin Philosophical Magazine and Journal of Science*, 3(19):321–343, 1877.

[119] Michael Faraday. *Philosophical Transactions of the Royal Society of London*, 136:1–20, 1846.

[120] Jun-Yang Chen, Jie Zhu, Delin Zhang, Dustin M. Lattery, Mo Li, Jian-Ping Wang, and Xiaojia Wang. *The Journal of Physical Chemistry Letters*, 7(13):2328–2332, 2016.

[121] Phoebe Tengdin Cong Chen Xun Shi Dmitriy Zusin Yingchao Zhang Christian Gentry Adam Blonsky Mark Keller-Peter Openeer Henry Kapteyn Zhensheng Tao, Wenjing You and Margaret Murnane. *EPJ Web of Conferences*, 205:04002, 2019.

[122] Del Atkinson, Dan A. Allwood, Gang Xiong, Michael D. Cooke, Colm C. Faulkner, and Russell P. Cowburn. *Nature Materials*, 2(2):85–87, 2003.

[123] A. V. Kimel, F. Bentivegna, V. N. Gridnev, V. V. Pavlov, R. V. Pisarev, and Th. Rasing. *Phys. Rev. B*, 63:235201, 2001.

[124] Chunfei Li. *Nonlinear Optics: principles and applications*. Springer, 2018.

[125] Robert W. Boyd. *Nonlinear optics*. Academic Press, 2008.

[126] J.W. You, S.R. Bongu, Q. Bao, and N.C. Panoiu. *Nanophotonics*, 8(1):63–97, 2019.

[127] Manfred Fiebig, Victor V. Pavlov, and Roman V. Pisarev. *J. Opt. Soc. Am. B*, 22(1):96–118, 2005.

[128] W. Eerenstein, N. D. Mathur, and J. F. Scott. *Nature*, 442:759, 2006.

[129] T. Zhao, A. Scholl, F. Zavaliche, K. Lee, M. Barry, A. Doran, M. P. Cruz, Y. H. Chu, C. Ederer, N. A. Spaldin, R. R. Das, D. M. Kim, S. H. Baek, C. B. Eom, and R. Ramesh. Nat mater. *Nat. Mater.*, 5:823, 2006.

[130] M. Fiebig, Thomas Lottermoser, Dennis Meier, and Morgan Trassin. *Nat. Rev.*, 1:16046, 2016.

[131] Pankaj Sharma, Daniel Sando Qi-Zhang, Jiangyu Li Valanoor Nagarajan Chi-Hou Lei, Yunya Liu, and Jan Seidel. *Science Advances*, 3(6):e1700512, 2017.

[132] Young-Min Kim Duk-Hyun Lee Jin-Soo Kim Yeon-Soo Kim Taekjib Choi Ji-Hoon Jeon, Ho-Young Joo and Bae-Ho Park. *Sci. Rep.*, 6:23299, 2016.

[133] T. Choi, V. Kiryukhin S. Lee, Y. J. Choi, and S.-W Cheong. *Science*, 324:63, 2009.

[134] S. J. Byrnes T. E. Conry S. R. Basu D. Paran L. Reichertz J. Ihlefeld C. Adamo A. Melville Y.-H. Chu C.-H. Yang J. L. Musfeldt D. G. Schlom J. W. Ager S. Y. Yang, L. W. Martin and R. Ramesh. *App. Phys. Lett.*, 95:062909, 2009.

[135] S. K. Nayak F-C. Sun D. George A. Pramanick M-G. Kang H-C. Song M. M. Alexander D. Lou G. A. Khodaparast S. P. Alpay N. Q. Vinh D. Maurya, A. Charkhesht and S. Priya. *Phys. Rev. B*, 96:134114, 2017.

[136] D. Maurya Min-Gyu Kang A. Sosa R. R. H. H. Mudiyanselage M. Clavel S. Gollapudi M. K. Hudait S. Priya M. A. Meeker, S. Kundu and G. A. Khodaparast. *Optical Materials*, 73:793, 2017.

[137] R. Ramesh and N. A. Spaldin. *Nat. Mater.*, 6:21, 2007.

[138] Shuxiang Dong-D. Viehland Ce-Wen Nan, M. I. Bichurin and G. Srinivasan. *J. Appl. Phys.*, 103:031101, 2008.

[139] Manuel Bibes and Agnés Barthélémy. *Nature Materials*, 7:425, 2008.

[140] A. Barthélémy S. Fusil, V. Garcia and M. Bibes. *Annu. Rev. Mater. Res.*, 44:91, 2014.

[141] T. Nan Y. Gao-G. M. Yang M. Liu X. Yang, Z. Zhou and N. X. Sun. *J. Mater. Chem. C*, 4:234, 2016.

[142] K. Mavani K. Takahashi H. Murakami M. Tonouchi D. S. Rana, I. Kawayama. *Adv. Mater.*, 21:2881, 2009.

[143] Seung-Yeul Yang Esther Alarcón-Liadó Junqiao Wu Ramamoorthy Ramesh Jan Seidel, Deyi Fu and Joel W. Ager. *Phys. Rev. Lett.*, 107:126805, 2011.

[144] Fengang Zheng Wen Dong Liang Fang Dawei Cao, Chunyan Wang and Mingrong Shen. *Nano. Lett.*, 12:2803, 2012.

[145] B. Jusserand A. Soukiassian L. Xie X. Q. Pan T. Dekorsy D. G. Schlom A. E. Bruchhausen, N. D. Lanzillotti-Kimura and A. Fainstein. *Phys. Rev. Mater.*, 2:106002, 2018.

[146] D. A. Tenne X. X. Xi D. G. Schlomb N. D. Lanzillotti-Kimura A. Bruchhausen A. Fainstein H. P. Sun X. Q. Pan A. Cros A. Soukiassian, W. Tian and A. Cantarero. *App. Phys. Lett.*, 90:042909, 2007.

[147] B. Perrin B. Jusserand A. Soukiassian N. D. Lanzillotti-Kimura, A. Fainstein and D. G. Schlom. *Phys. Rev. Lett.*, 104:187402, 2010.

[148] P. A. Fleury and P. D. Lazay. *Phys. Rev. Lett.*, 26:1331, 1971.

[149] W. Chang R. Uecker P. Reiche Y. L. Li S. Choudhury-W. Tian M. E. Hawley B. Craigo A. K. Tagantsev X. Q. Pan S. K. Streiffer L. Q. Chen S. W. Kirchoefer J. Levy J. H. Haeni, P. Irvin and D. G. Schlom. *Nature*, 430:758, 2004.

[150] J. B. Neaton and K. M. Rabe. *Appl. Phys. Lett.*, 82:1586, 2003.

[151] Y. L. Li A. Sharan J. Schubert R. Uecker P. Reiche-Y. B. Chen X. Q. Pan V. Gopalan L.-Q. Chen D. G. Schlom K. J. Choi, M. Biegalski and C. B. Eom. *Science*, 306:1005, 2004.

[152] Arthur J. Viescas Yongjae Lee Hongjun Zhou Tae-Jin Park, Georgia C. Papaefthymiou and Stanislaus S. Wong. *Phys. Rev. B:Condens. Matter Mater. Phys.*, 82:024431, 2010.

[153] B. Madon, H. Byul Kang, M. Gyu Kang, D. Maurya, B. A. Magill, M. J. P. Alves, J.-E. Wegrowe, H.-J. Drouhin, S. Priya, and Aip Advances G. A. khodaparast. *AIP Adv.*, 8(10):105034, 2018.

[154] Y. Zhou A. Chopra D. Maurya S. Priya M. Raschke-A. Belyanin C. J. Stanton G. A. Khodaparast B. A. Magill, K.-D. Park. *Energy Harvesting and Systems*, 3:229, 2016.

[155] S. A. McGill Y. Zhou A. Chopra H.-C. Song C. J. Stanton S. Priya B. A. Magill, M. Bishop and G. A. Khodaparast. *Proc. of SPIE*, 9551:9551oT, 2015.

[156] R. Safi and H. Shokrollahi. *Progress in Solid State Chemistry*, 40:6, 2012.

[157] A. J. Viescas A. R. Moodenbaugh T-J. Park, G. C. Papaefthymiou and S. S. Wong. *Nano Lett.*, 7:766, 2007.

[158] T-J. Park, G. C. Papaefthymiou, A. J. Viescas, Y. Lee, H. Zhou, and S. S. Won. *Phys. Rev. B: Condens. Matter Mater. Phys.*, 82:024431, 2010.

[159] F. Zavaliche K. Lee M. Barry A. Doran M. P. Cruz Y. H. Chu C. Ederer N. A. Spaldin R. R. Das D. M. Kim S. H. Baek C. B. Eom T. Zhao, A. Scholl and R. Ramesh. *Nature Materials*, 5:823, 2006.

[160] S. Petit J. Kreisel H. Béa, M. Bibes and A. Barthélémy. *Philosophical Magazine Letters*, 87:165, 2007.

[161] D. Rahmedov J. Liu P. Rovillain C. Toulouse I. C. Infante A. P. Pyatakov S. Fusil E. Jacquet C. Carrétéro C. Deranlot S. Lisenkov D. Wang J-M. Le Breton M. Cazayous A. Sacuto J. Juraszek A. K. Zvezdin L. Bellaiche B. Dkhil A. Barthélémy D. Sando, A. Agbelele and M. Bibes. *Nature Materials*, 12:641, 2013.

[162] Yu-Xiang Zhang Zhenhua Shi Jian-Ping Zhou, Rui-Juan Xiao and Gang-Qiang Zhu. *J. Mater. Chem. C,*, 3:6924, 2015.

[163] Huolin L. Xin-Eugene A. Eliseev Anna N. Morozovska Sergei V. Kalinin Ryota Takahashi Mikk Lippmaa Yuji Matsumoto Akira Imai, Xuan Cheng and Valanoor Nagarajan. *ACS Nano*, 7:11079, 2013.

[164] Zuanming Jin, Yue Xu, Zhengbing Zhang, Gaofang Li, Xian Lin, Guohong Ma, Zhenxiang Cheng, and Xiaolin Wang. *Appl. Phys. Lett.*, 100:071105, 2012.

[165] Masaya Nagai Toshimitsu Ito Eiichi Matsubara, Takeshi Mochizuki and Masaaki Ashida. *Jpn. J. Appl. Phys*, 54:092201, 2015.

[166] C. W. Luo L. Y. Chen, J. C. Yang, C. W. Laing, and K. H. Wu. *Appl. Phys. Lett.*, 101:041902, 2012.

[167] N. J. Podraza S. Denev M. Ramirez Y.-H. Chu L. W. Martin J. Ihlefeld T. Heeg J. Schubert D. G. Schlom J. Orenstein R. Ramesh-R. W. Collins J. L. Musfeldt A. Kumar, R. C. Rai and V. Gopalan. *Appl. Phys. Lett.*, 92:121915, 2008.

[168] Kunie Ishioka Evan M. Thatcher Amlan Kumar Basak, Hrvoje Petek and Christopher J. Stanton. *Phys. Rev. B*, 91:125201, 2015.

[169] I. C. Infante P. Gemeiner V. E. Gusev B. Dkhil M. Lejman, G. Vaudel and P. Ruello. *Nature Communications*, 5(4301), 2014.

[170] Andreas Beyer Avinash Rustagi Christopher J. Stanton Wolfgang Stolz Kerstin Volz Ulrich Höfer Kunie Ishioka, Kristina Brixius and Hrvoje Petek. *Applied Physics Letters*, 108:51607, 2016.

[171] J. F. Scott R. Palai and R. S. Katiyar. *Phys. Rev. B*, 81:024115, 2010.

[172] Jure Demsar Kiminori Ushida Muneaki Hase, Kunie Ishioka and Masahiro Kitajima. *Phys. Rev. B*, 71:184301, 2005.

[173] Rogerio de Sousa and Joel E. Moore. *Appl. Phys. Lett.*, 92:022514, 2008.

[174] J. van Kranendonk and J. van Vleck. *Rev. Mod. Phys*, 30:1, 1958.

[175] T. Kimura A. J. Taylor D. Talbayev. S. A. Trugman, A. V. Balatsky and R. D. Averitt. *Phys. Rev. Lett.*, 101:097603, 2008.

[176] Samuel J. Whiteley, Gary Wolfowicz, Christopher P. Anderson, Alexandre Bourassa, He Ma, Meng Ye, Gerwin Koolstra, Kevin J. Satzinger, Martin V. Holt, F. Joseph Heremans, Andrew N. Cleland, David I. Schuster, Giulia Galli, and David D. Awschalom. *Nature*, 15:490, 2019.

[177] H.-S. Chang G. A. Peairs A. Bienfait M.-H. Chou A. Y. Cleland C. R. Conner E. Dumur J. Grebel I. Gutierrez B. H. November R. G. Povey S. J. Whiteley D. D. Awschalom D. I. Schuster A. N. Cleland K. J. Satzinger, Y. P. Zhong. *Nature*, 563:661, 2018.

[178] J. Kono-A. Oiwa J. Wang, G. A. Khodaparast and H. Munekata. *Journal of Modern Optics*, 51:2771, 2004.

[179] Y. Hashimoto J. Kono G. A. Khodaparast L. Cywinski L. J. Sham G. D. Sanders C. J. Stanton J. Wang, C. Sun and H. Munekata. *J. Phys.: Condens. Matter*, 18:R501, 2006.

[180] Joseph G. Tischler Michael K. Yakes, Cory D. Cress and Allan S. Bracke. *ACS Nano*, 3877, 2010.

[181] M. DrDomenico and S. H. Wemple. *Journal of Applied Physics*, 40(2):720–734, 1969.

[182] T. Otto, S. Grafström, H. Chaib, and L. M. Eng. *Applied Physics Letters*, 84(7):1168–1170, 2004.

[183] Bruce W. Wessels. 37(1):659–679, 2007.

[184] A. M. Kalashnikova, A. V. Kimel, R. V. Pisarev, V. N. Gridnev, P. A. Usachev, A. Kirilyuk, and Th. Rasing. *Phys. Rev. B*, 78:104301, 2008.

[185] Amit Kumar, Ram C. Rai, Nikolas J. Podraza, Sava Denev, Mariola Ramirez, Ying-Hao Chu, Lane W. Martin, Jon Ihlefeld, T. Heeg, J. Schubert, Darrell G. Schlom, J. Orenstein, R. Ramesh, Robert W. Collins, Janice L. Musfeldt, and Venkatraman Gopalan. *Applied Physics Letters*, 92(12):121915, 2008.

[186] Mariola O. Ramirez, M. Krishnamurthi, S. Denev, A. Kumar, Seung-Yeul Yang, Ying-Hao Chu, Eduardo Saiz, Jan Seidel, A. P Pyatakov, A. Bush, D. Viehland, J. Orenstein, R. Ramesh, and Venkatraman Gopalan. *Applied Physics Letters*, 92(2):022511, 2008.

[187] Morgan Trassin, Gabriele De Luca, Sebastian Manz, and Manfred Fiebig. *Advanced Materials*, 27(33):4871–4876, 2015.

[188] S. E. Lofland, K. F. McDonald, C. J. Metting, E. Knoesel, M. Murakami, M. A. Aronova, S. Fujino, M. Wuttig, and I. Takeuchi. *Phys. Rev. B*, 73:092408, 2006.

[189] Dong Hak Kim and D. Lim. 62(5):734–738, 2013.

[190] Jie-su Wang, Kui-juan Jin, Hai-zhong Guo, Jun-xing Gu, Qian Wan, Xu He, Xiao-long Li, Xiu-lai Xu, and Guo-zhen Yang. *Scientific Reports*, 6:38268, 2016.

[191] T.-H. Wang, C.-S. Tu, H.-Y. Chen, Y. Ding, T. C. Lin, Y.-D. Yao, V. H. Schmidt, and K.-T. Wu. *Journal of Applied Physics*, 109(4):044101–044101–4, 2011.

[192] Kenji Ueda, Hitoshi Tabata, and Tomoji Kawai. *Applied Physics Letters*, 75(4):555–557, 1999.

[193] M Mahesh Kumar, S Srinath, G.S Kumar, and S.V Suryanarayana. *Journal of Magnetism and Magnetic Materials*, 188(1):203 – 212, 1998.

[194] M Mahesh Kumar, A Srinivas, G S Kumar, and S V Suryanarayana. *Journal of Physics: Condensed Matter*, 11(41):8131–8139, 1999.

[195] Tsutomu Sasaki, Yasutoshi Hirabayashi, Hiroyuki Kobayashi, and Yukio Sakashita. *Japanese Journal of Applied Physics*, 50(9):09NA08, 2011.

[196] Su-Chul Yang, Ashok Kumar, Valeri Petkov, and Shashank Priya. *Journal of Applied Physics*, 113(14):144101, 2013.

[197] Tae-Jin Park, Georgia C. Papaefthymiou, Arthur J. Viescas, Yongjae Lee, Hongjun Zhou, and Stanislaus S. Wong. *Phys. Rev. B*, 82:024431, 2010.

[198] Brenden Magill, Kyoung-Duck Park, Yuan Zhou, Anuj Chopra, Deepam Maurya, S.Jeba Priya, Markus Raschke, Alexey Belyanin, Christopher Stanton, and Giti Khodaparast. 2016.

[199] Jie su Wang, Kui juan Jin, Hai zhong Guo, Jun xing Gu, and Xu He Qian Wan, Xiao long Li, Xiu lai Xu, and Guo zhen Yang. *Sci. Rep.*, 6:38268, 2016.

[200] Amit Kumar, Sava Denev, Robert J. Zeches, and Nikolas J. Podraza Eftihia Vlahos, Alexander Melville, Darrell G. Schlom, R. Ramesh, and Venkatraman Gopalan. *Appl. Phys. Lett.*, 97:112903, 2010.

[201] Morgan Trassin, Gabriele De Luca, Sebastian Manz, and Manfred Fiebig. *Advanced Materials*, 27(33):4871–4876, 2015.

[202] Sava A. Denev, Tom T. A. Lummen, Eftihia Barnes, Amit Kumar, and Venkatraman Gopalan. *Journal of the American Ceramic Society*, 94(9):2699–2727, 2011.

[203] Y. R. Shen. *Nature*, 337(6207):519–525, 1989.

[204] Luigi Bonacina, Pierre-François Brevet, Marco Finazzi, and Michele Celebrano. *J. Appl. Phys.*, 127:230901, 2020.

[205] Shinji Yamashitaa. *APL Photonics*, 4:034301, 2019.

[206] Leiming Wu, Yuze Dong, Jinlai Zhao, Dingtao Ma, Weichun Huang, Ye Zhang, Yunzheng Wang, Xiantao Jiang, Yuanjiang Xiang, Jianqing Li, Yaqing Feng, Jialiang Xu, and Han Zhang. *Advanced Materials*, 31(14):1807981, 2019.

[207] Xiantao Jiang, Liangjing Zhang, Shunxiang Liu, Yiyue Zhang, Zhiliang He, Wenjia Li, Feng Zhang, Yihuang Shi, Wei Lü, Yu Li, Qiao Wen, Jiagen Li, Jun Feng, Shuangchen Ruan, Yu-Jia Zeng, Xi Zhu, Yuerui Lu, and Han Zhang. *Advanced Optical Materials*, 6(16):1800561, 2018.

[208] Lu Lu, Xian Tang, Rui Cao, Leiming Wu, Zhongjun Li, Guanghui Jing, Biqin Dong, Shunbin Lu, Ying Li, , Yuanjiang Xiang, Jianqing Li, Dianyuan Fan, and Han Zhang. *Advanced Optical Materials*, 5(17):1700301, 2017.

[209] Xiantao Jiang, Artem V.Kuklinc, Alexander Baev, YanqiGea, Hans Ågrencd, Han Zhang, and Paras N.Prasad. *Physics Reports*, 848:1, 2020.

[210] Lukas Mennel, Matthias Paur, and Thomas Mueller. *APL Photonics*, 4:034404, 2019.

[211] Aneesh Koka and Henry A. Sodano. *Nature Communications*, 4(1):2682, 2013.

[212] Xudong Wang. *Nano Energy*, 1(1):13 – 24, 2012.

[213] Uri Kushnir and Oded Rabinovitch. *Sensors and Actuators A: Physical*, 150(1):102 – 109, 2009.

[214] A. M. Flynn, L. S. Tavrow, S. F. Bart, R. A. Brooks, D. J. Ehrlich, K. R. Udayakumar, and L. E. Cross. Piezoelectric micromotors for microrobots. 3:1163–1172, 1990.

[215] Toru Fujii, Shunji Watanabe, Masatoshi Suzuki, and Takamitsu Fujiu. *Journal of Vacuum Science & Technology B: Microelectronics and Nanometer Structures Processing, Measurement, and Phenomena*, 13(3):1119–1122, 1995.

[216] Ph Luginbuhl, G.-A Racine, Ph Lerch, B Romanowicz, K.G Brooks, N.F [de Rooij], Ph Renaud, and N Setter. *Sensors and Actuators A: Physical*, 54(1):530 – 535, 1996.

[217] N. A. Riza, D. L. Polla, W. P. Robbins, and D. E. Glumac. High resolution 50 nm linear displacement macroscale meander-line pzt actuator. *Electronics Letters*, 29(18):1606–1608, 1993.

[218] J. J. Bernstein, S. L. Finberg, K. Houston, L. C. Niles, H. D. Chen, L. E. Cross, K. K. Li, and K. Udayakumar. *IEEE Transactions on Ultrasonics, Ferroelectrics, and Frequency Control*, 44(5):960–969, 1997.

[219] Xi Chen, Shiyou Xu, Nan Yao, and Yong Shi. *Nano Letters*, 10(6):2133–2137, 2010.

[220] Ph Luginbuhl, G.-A Racine, Ph Lerch, B Romanowicz, K.G Brooks, N.F [de Rooij], Ph Renaud, and N Setter. *Sensors and Actuators A: Physical*, 54(1):530 – 535, 1996.

[221] Pil Gu Kang, Tae Kwon Lee, Chang Won Ahn, Ill Won Kim, Hyun Hwa Lee, Soo Bong Choi, Kil Dong Sung, and Jong Hoon Jung. *Nano Energy*, 17:261 – 268, 2015.

[222] Aneesh Koka and Henry A. Sodano. *Advanced Energy Materials*, 4(11):1301660, 2014.

[223] Long Gu, Nuanyang Cui, Li Cheng, Qi Xu, Suo Bai, Miaomiao Yuan, Weiwei Wu, Jinmei Liu, Yong Zhao, Fei Ma, Yong Qin, and Zhong Lin Wang. *Nano Letters*, 13(1):91–94, 2013.

[224] Weiwei Wu, Suo Bai, Miaomiao Yuan, Yong Qin, Zhong Lin Wang, and Tao Jing. *ACS Nano*, 6(7):6231–6235, 2012.

[225] Sheng Xu, Benjamin J. Hansen, and Zhong Lin Wang. *Nature Communications*, 1(1):93, 2010.

[226] Xudong Wang. *Nano Energy*, 1(1):13 – 24, 2012.

[227] Andreas Janshoff, Hans-Joachim Galla, and Claudia Steinem. *Angewandte Chemie International Edition*, 39(22):4004–4032, 2000.

[228] Jong Yeog Son, Jung-Hoon Lee, Seungwoo Song, Young-Han Shin, and Hyun Myung Jang. *ACS Nano*, 7(6):5522–5529, 2013.

[229] Yuan-Yuan Tang, Wan-Ying Zhang, Peng-Fei Li, Heng-Yun Ye, Yu-Meng You, and Ren-Gen Xiong. *Journal of the American Chemical Society*, 138(48):15784–15789, 2016.

[230] Min Gyu Kang, Seul-Yi Lee, Deepam Maurya, Christopher Winkler, Hyun-Cheol Song, Robert B. Moore, Mohan Sanghadasa, and Shashank Priya. *Advanced Functional Materials*, 27(29):1701542, 2017.

[231] Min Gyu Kang Kang, Han Byul Kang Kang, Michael Clavel, Deepam Maurya, Sreenivasulu Gollapudi, Mantu Hudait, and Priya Shashank Sanghadasa, Mohan. *Nano Lett.*, 18:2835–2843, 2018.

[232] Maria Cristina Larciprete and Marco Centini. *Applied Physics Reviews*, 2:031302, 2015.

[233] Y. Dang, C. Zhong, G. Zhang, D. Ju, L. Wang, S. Xia, H. Xia, and X. Tao. *Chemistry of Materials*, 28(19):6968, 2016.

[234] Robert C. Miller. *Phys. Rev.*, 134:A1313, 1964.

[235] Yevgeny Rakitaa, Omri Bar-Ellib, Elena Meirzadeha, Hadar Kaslasia, Yagel Pelega, Gary Hodesa, Igor Lubomirskya, Dan Oronb, David Ehrea, and David Cahena. *Proceedings of National Academy of Science*, 114(28):E5504, 2017.

[236] B. Noheda, J. A. Gonzalo, L. E. Cross, R. Guo, D. E. Cox S.-E. Park, and G. Shiran. *Phys. Rev. B*, 61:8687, 2000.

[237] M. Trassin, G. De Luca, S. Manz, and M. Fiebig. *Adv. Mater.*, 27:4871, 2015.

[238] Jie su Wang, Kui juan Jin, Jun xing Gu, Qian Wan, Hong bao Yao, and Guo zhen Yang. Direct evidence of correlation between the second harmonic generation anisotropy patterns and the polarization orientation of perovskite ferroelectric. *Sci Rep 7*, 7:9502, 2017.

[239] Yuan Zhang, Yi Zhang, Quan Guo, Xiangli Zhong, and Haidong Lu Yinghao Chu, Gaokuo Zhong, Jie Jiang, Congbing Tan, Min Liao, Zhihui Lu, Dongwen Zhang, Jinbin Wang, Jianmin Yuan, and Yichun Zhou. *npj,Computational Materials*, 4(39):1, 2018.

[240] S. Janz, Usman G. Akano, and Ian V. Mitchell. *Applied Physics Letters*, 68(23):3287–3289, 1996.

[241] R. Prasanth, L. K. van Vugt, D. A. M. Vanmaekelbergh, and H. C. Gerritsen. *Applied Physics Letters*, 88(18):181501.

[242] Md Azimul Haque, Seyoung Kee, Diego Rosas Villalva, Wee-Liat Ong, and Derya Baran. *Advanced Science*, 7(10):1903389, 2020.

[243] Maksym V. Kovalenko, Loredana Protesescu, and Maryna I. Bodnarchuk. *Science*, 358(6364):745–750, 2017.

[244] Pierre-Adrien Mante, Constantinos C. Stoumpos, Mercouri G. Kanatzidis, and Arkady Yartsev. *Nature Communications*, 8(1):14398, 2017.

[245] William Shockley and Hans J. Queisser. *Journal of Applied Physics*, 32(3):510–519, 1961.

[246] W. Pötz and P. Kocevar. *Phys. Rev. B*, 28:7040–7047, 1983.

[247] L. C. Hirst, R. J. Walters, M. F. Führer, and N. J. Ekins-Daukes. *Applied Physics Letters*, 104(23):231115, 2014.

[248] L. C. Hirst, H. Fujii, Y. Wang, M. Sugiyama, and N. J. Ekins-Daukes. *IEEE Journal of Photovoltaics*, 4(1):244–252, 2014.

[249] A. Le Bris, L. Lombez, S. Laribi, G. Boissier, P. Christol, and J.-F. Guillemoles. *Energy Environ. Sci.*, 5:6225–6232, 2012.

[250] J. Tang, V. R. Whiteside, H. Esmaielpour, S. Vijeyaragunathan, T. D. Mishima, M. B. Santos, and I. R. Sellers. *Applied Physics Letters*, 106(6):061902, 2015.

[251] M. Bhowmick, G. A. Khodaparast, T. D. Mishima, M. B. Santos, D. Saha, G. Sanders, and C. J. Stanton. *Journal of Applied Physics*, 120(23):235702, 2016.

[252] M. C. Hanna and A. J. Nozik. *Journal of Applied Physics*, 100(7):074510, 2006.

[253] P. Aliberti, Y. Feng, Y. Takeda, S. K. Shrestha, M. A. Green, and G. Conibeer. *Journal of Applied Physics*, 108(9):094507, 2010.

[254] D. König, Y. Takeda, and B. Puthen-Veettil. *Applied Physics Letters*, 101(15):153901, 2012.

[255] D. J. Farrell, Y. Takeda, K. Nishikawa, T. Nagashima, T. Motohiro, and N. J. Ekins-Daukes. *Applied Physics Letters*, 99(11):111102, 2011.

[256] Morio Wada and Haruo Hosomatsu. *Applied Physics Letters*, 64(10):1265–1267, 1994.

[257] Hideo Sugiura. *Journal of Crystal Growth*, 164(1):434 – 441, 1996.

[258] D. Elvira, R. Hostein, B. Fain, L. Monniello, A. Michon, G. Beaudoin, R. Braive, I. Robert-Philip, I. Abram, I. Sagnes, and A. Beveratos. *Phys. Rev. B*, 84:195302, 2011.

[259] Rutger Vrijen and Eli Yablonovitch. *Physica E: Low-dimensional Systems and Nanostructures*, 10(4):569 – 575, 2001.

[260] P. Murzyn, C. R. Pidgeon, P. J. Phillips, M. Merrick, K. L. Litvinenko, J. Allam, B. N. Murdin, T. Ashley, J. H. Jefferson, A. Miller, and L. F. Cohen. *Applied Physics Letters*, 83(25):5220–5222, 2003.

[261] K. C. Hall, Wayne H. Lau, K. Gündoğdu, Michael E. Flatté, and Thomas F. Boggess. *Applied PhMennelysics Letters*, 83(14):2937–2939, 2003.

[262] Hong Ma, Zuanming Jin, Lihua Wang, and Guohong Ma. *Journal of Applied Physics*, 109(2):023105, 2011.

[263] Bo Li, Maria C. Tamargo, and Carlos A. Meriles. *Applied Physics Letters*, 91(22):222114, 2007.

[264] Michio Ikezawa, Bipul Pal, Yasuaki Masumoto, I. Ignatiev, S. Verbin, and . *Physical Review B*, 72, 2005.

[265] Luigi Bonacina, Pierre-François Brevet, Marco Finazzi, and Michele Celebrano. *Journal of Applied Physics*, 127(23):230901, 2020.

[266] Lukas Novotny and Niek van Hulst. Antennas for light. *Nature Photonics*, 5(2):83–90, 2011.

[267] Martti Kauranen and Anatoly V. Zayats. Nonlinear plasmonics. *Nature Photonics*, 6(11):737–748, 2012.

[268] César Clavero. *Nature Photonics*, 8(2):95–103, 2014.

[269] Heykel Aouani, Miguel Navarro-Cia, Mohsen Rahmani, Themistoklis P. H. Sidiropoulos, Minghui Hong, Rupert F. Oulton, and Stefan A. Maier. *Nano Letters*, 12(9):4997–5002, 2012.

[270] Jeffrey N. Anker, W. Paige Hall, Olga Lyandres, Nilam C. Shah, Jing Zhao, and Richard P. Van Duyne. *Nature Materials*, 7(6):442–453, 2008.

[271] Seied Ali Safiabadi Tali and Wei Zhou. *Nanophotonics*, 8(7):1199–1225, 2019.

[272] Blai Casals, Nahuel Statuto, Michael Foerster, Alberto Hernández-Mínguez, Rafael Cichelero, Peter Manshausen, Ania Mandziak, Lucía Aballe, Joan Manel Hernàndez, and Ferran Macià. *Phys. Rev. Lett.*, 124:137202, 2020.

[273] Andreas Rückriegel and Rembert A. Duine. *Phys. Rev. Lett.*, 124:117201, 2020.

[274] Wendell T. Hill and Chi H. Lee. *Light-matter interaction: atoms and molecules in external field and nonlinear optics*. Wiley-VCH, 2007.

[275] Eleonora Luppi, Elena Degoli, Matteo Bertocchi, Stefano Ossicini, and Valérie Véniard. *Phys. Rev. B*, 92:075204, 2015.

[276] Kory Beach, Michael C. Lucking, and Humberto Terrones. *Phys. Rev. B*, 101:155431, 2020.

[277] S. V. Govorkov, V. I. Emel'yanov, N. I. Koroteev, G. I. Petrov, I. L. Shumay, and V. V. Yakovlev. *J. Opt. Soc. Am. B*, 6(6):1117–1124, Jun 1989.

[278] Manfred Fiebig, Victor V. Pavlov, and Roman V. Pisarev. *J. Opt. Soc. Am. B*, (1):96–118, 2005.

[279] C. Neacsu, B. V. Aken, M. Fiebig, and M. Raschke. Second-harmonic near-field imaging of ferroelectric domain structure of ymno3. *Physical Review B*, 79, 2009.

[280] Takanori Suzuki, V. Venkataramanan, and Masakazu Aono. *Japanese Journal of Applied Physics*, 40(Part 2, No. 10B):L1119–L1122, 2001.

[281] Andrei Kirilyuk. *Journal of Physics D: Applied Physics*, 35(21):R189–R207, 2002.

[282] R. V. Pisarev, I. Sänger, G. A. Petrakovskii, and M. Fiebig. *Phys. Rev. Lett.*, 93:037204, 2004.

[283] M. Fiebig, Th. Lottermoser, and R. V. Pisarev. *Journal of Applied Physics*, 93(10):8194–8196, 2003.

[284] Yu. F. Popov, A. M. Kadomtseva, S. S. Krotov, D. V. Belov, G. P. Vorob'ev, P. N. Makhov, and A. K. Zvezdin. *Low Temperature Physics*, 27(6):478–479, 2001.

[285] Razvan Dabu. *Crystals*, 9:347, 2019.

[286] Eugene Hecht. *Optics*. Pearson, 2002.

Appendices

Appendix A

Laser Systems

A.1 Ti:sapphire Oscillator

Ti:sapphire crystal is developed by introducing a small quantity of TiO_3 into Al_2O_3, where a small number of Al^{3+} are replaced by the Ti^{3+} cations. The cation responsible for the lasing action is the trivalent titanium. Ti^{3+} is a unique transition metal due to its electronic configuration. The configuration of Ti^{3+} ion is $3d^1$, where lower Ti $3d$ level is three-fold degenerate and the upper Ti 3d level is two-fold degenerate. The absorption of the crystal ranges from ∼400 nm to ∼600 nm and it peaks at 555 nm and 488 nm [285]. Whereas the fluorescence ranges from 550 nm to 1μm [285]. Due to the overlap of the absorption and the fluorescence spectra, the lasing action occurs only for the wavelengths longer than 670 nm.

The amplified laser system (by Coherent Inc.) uses Chirped Pulse amplification (CPA) to amplify the femtosecond pulses. Our amplified pulses are linearly polarized pulses with a center wavelength of 800 nm, pulse energy of $\sim$ 1 mJ and the a repetition rate of 1 kHz. We also use the coherent chameleon which is a tunable pulse laser with the wavelength range of 680 nm- 1080 nm, with a repetition rate of 80 MHz.

Appendix B

Experimental setups

B.1 Time Resolved Differential Reflectivity Setup

In the pump-probe setup, the beam is split into two beams, pump and probe. The pump beam is directed to a retroreflector, mounted on a moving stage which adjust the time delay between the pump and the probe beams. Before reaching the sample both beams pass through a set of optics where optical path lengths are coordinated. The two beams are focused on the sample using lenses where the two beams overlap with a spot-size of about 150-200 μm (pump beam is comparatively bigger than the probe beam). The ratio of pump and probe fluences was kept around 100:1 by mounting a neutral density filter on the probe path. A detector (Nirvana™ Auto-Balanced Optical Receivers-Model 2007) was placed behind the sample or to a side of the sample, to capture the transmitted or reflected light of the probe beam, respectively. A lens was employed to focus the beam on to the detector. In order to increase the signal to noise ratio, collected data was recorded using a lock-in amplifier and a computer. The modulation frequency was provided by either the laser frequency (1 kHz: Non-degenerate configuration) or by mounting a mechanical chopper (1 kHz) on the pump path. In the degenerate configuration, the light source was the Coherent Chameleon pulsed laser, where the wavelengths can be varied between 700-1050 nm and laser fluences were varied using a laser module, and the sample is mounted inside an electromagnet tunable up to 1 T.

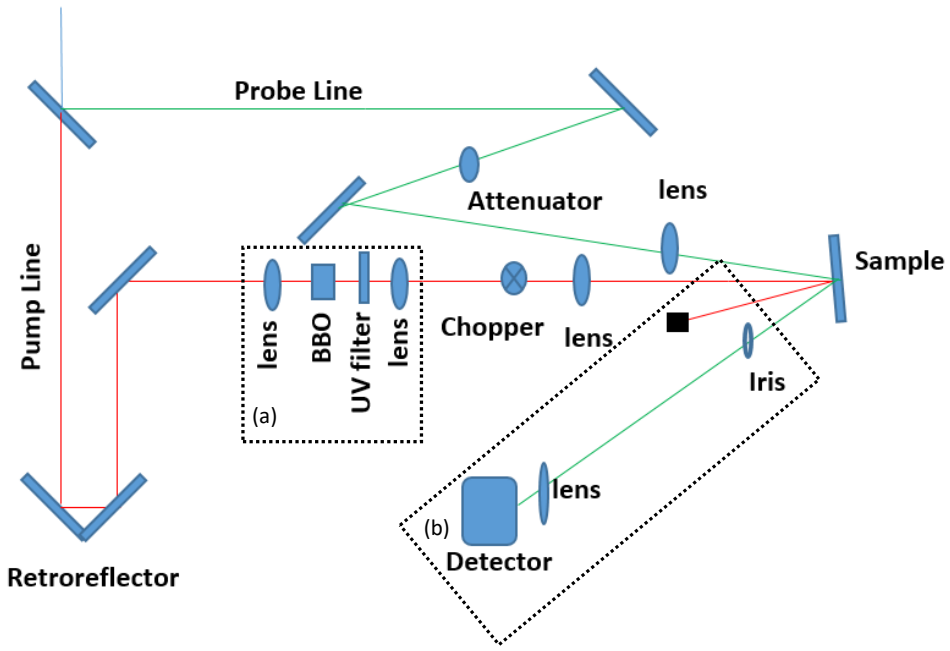

Figure B.1: Schematic diagram of the TRDR setup

In the non-degenerate case, the light source is the coherent amplifier system. Thus this is a high fluence (mJ) configuration in comparison to the degenerate setup. Also, the frequency of the pump beam was doubled using a BBO crystal (Fig. B.1; dotted box (a)), and here the laser fluences were varied using a neutral density filter.

B.1.1 BBO Crystal

BBO crystal is a non-centrosymmetric crystal that exhibit $\chi^{(2)}$ nonlinearity. Thus, these crystals are used as frequency doublers. In the non-degenerate pump-probe setup, BBO crystal converts the 800 nm femtosecond laser beam into the 400 nm beam by a second-harmonic generation with same short pulse duration without significantly distorting the spectral width.

B.1.2 Detector

The photodetector we have used in these setups is a Nirvana photoreceiver (Newport: Nirvana™ Auto-Balanced Optical Receivers: model 2007). This has a spectral response in the range of 400 - 1070 nm. This can also be used to detect two signals (that is useful in measuring TRMOKE and TROIB). The built-in low-frequency feedback loop maintains the automatic balance between the two signals.

B.2 Time Resolved OIB and MOKE Spectroscopy Setup

The basic configuration of the TRMOKE setup is the same as the degenerate TRDR setup explained in the previous section. Here, a quarter-wave plate was employed to circularly polarize the pump beam and a half-wave plate was employed to linearly polarize the probe beam (Fig. B.2). The spin relaxation is measured using the Kerr rotation of the probe beam. The reflected probe beam is passed through a Wollaston prism, that separates S and P components of the reflected beams. The intensity difference between the two polarization states is measured as a function of time delay.

B.2.1 Wave-plates

The main function of a waveplate is to alter the state of polarization of a light beam by delaying one of the orthogonal polarization components with respect to the other [286]. Waveplates are made out of birefringent materials that have two distinct indices of refraction. Thus, the incident light is separated into its parallel and orthogonal components and the phase shift between the two orthogonal components change the polarization state of the transmitted beam [286]. The common terminologies used for the two orthogonal axes are

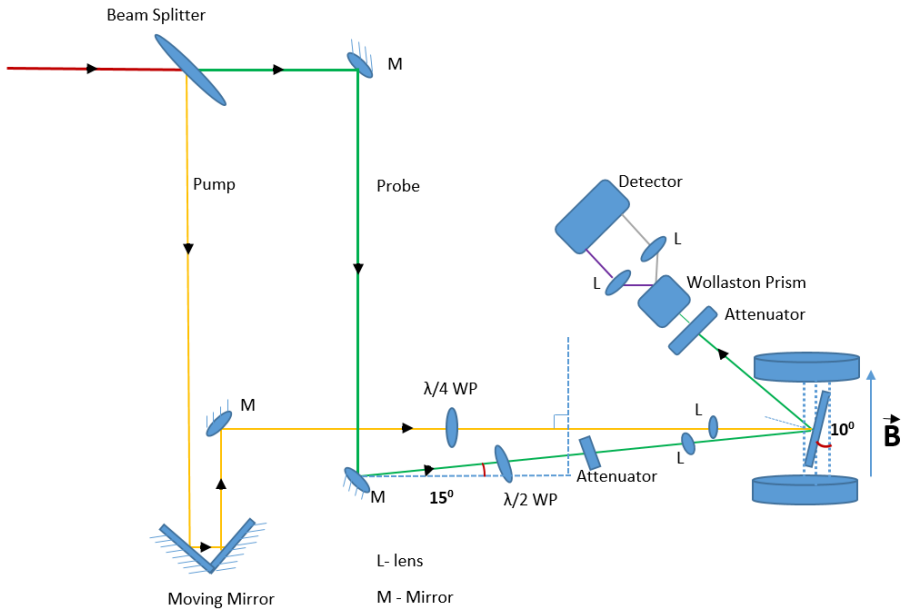

Figure B.2: Schematic diagram of the TRMOKE Setup

"fast" and "slow", where the index of refraction along the "fast" axis is smaller than the "slow" axis. The waveplates are designed with different thicknesses to produce different polarization states. The resultant phase shift ($\delta\psi$) of a waveplate is as following [286]:

$$\delta\psi = 2\pi\Delta n\frac{L}{\lambda}, \tag{B.1}$$

where Δn is the birefringence, and L is the thickness of the crystal. Most common waveplates are half-waveplate ($\lambda/2$) and a quarter-waveplate ($\lambda/4$). In the case of $\lambda/2$, the resultant phase difference is an odd multiple of a half-wave, this alters the linear polarization state of the transmitted beam. Similarly, the phase difference in a $\lambda/4$ is an odd multiple of a quarter-wave. But, here the polarization of the transmitted beam is either circular or elliptical. In order to generate a circularly polarized light beam, the wave plate is rotated such that the angle between the plane of the incident light and the fast axis is 45 degrees.

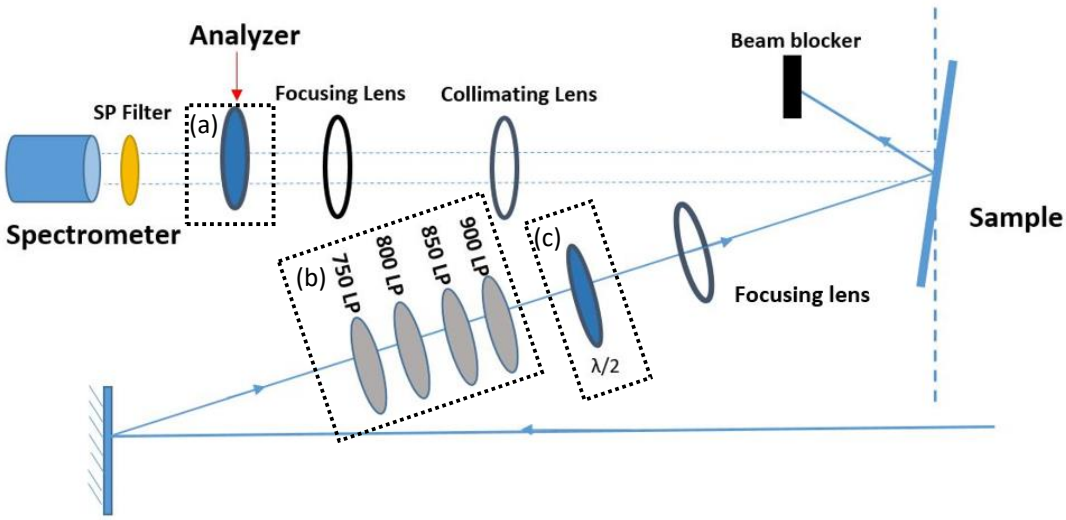

Figure B.3: Schematic diagram of the SHG setup

B.2.2 Wallaston Prism

Wollaston prism is an important component in TROIB and TRMOKE measurement setups. When an unpolarized light beam is transmitted through a Wollaston prism, it separates the light beam into two orthogonally polarized beams, S and P. The general methodology of making a Wollaston prism is by combining two orthogonal calcite prisms. The divergence angle between the two transmitted beams can be changed by rotating the prism wedge angle with respect to each wavelength.

B.3 Photoluminescence/SHG/Up-conversion Luminescence Spectroscopy Setup

Figure B.3 display the schematic diagram of the setup. The spectrometer used in the setup is the Horibe iHR Series 550 mm. In polarization dependent measurements the incident polar-

ization was varied via a Thor-Lab via a Half-Wave Liquid Crystal Variable Retarder/Wave Plate (Thorlabs; LCC1421-B) Fig. B.3,dotted box (c). Also, a combination of filter were employed for two main reasons, (1) the filter before the spectrometer is to block the laser line (fundamental beam). This filter is chosen such that it transmits the wavelength range we are interested in and block the fundamental beam. (2) The set of filters on the incident path (Fig. B.3, dotted box (b)) is used to block the fluorescence from the Ti:sapphire laser.

B.3.1 Spectral Filters

Filters are used as a protection mechanism to block fundamental beam (laser beam) going into the spectrometer. In experiments, we use both bandpass and edgepass filters. The wavelength range of the filter is chosen depending on the wavelength of the laser and the emission wavelength range of the sample we are interested in. A filter is produced by combining several dielectric stacks, where each dielectric stack is multiple alternating layers of low-index and high-index dielectric material. These filters have different transmission profiles, where depending on the quality of the filter the roughness of the transmission varies. Transmission profile of two different 900 shortpass (i.e. this filter only pass wavelengths shorter than 900 nm) filters are presented in Fig. B.4

B.3.2 Spectroscopy Artifacts

Figure B.5 illustrates a laser-induced artifact in luminescence spectra. The broad peak we observe is the broadband fluorescence of the Ti:sapphire crystal. The intensity of the fluorescence from the crystal is much lower compared to most of the luminescence spectra of material structures. However, with the combination of longer exposure time, high excitation power, and a high sensitive spectrometer can result in the observation of this artifact.

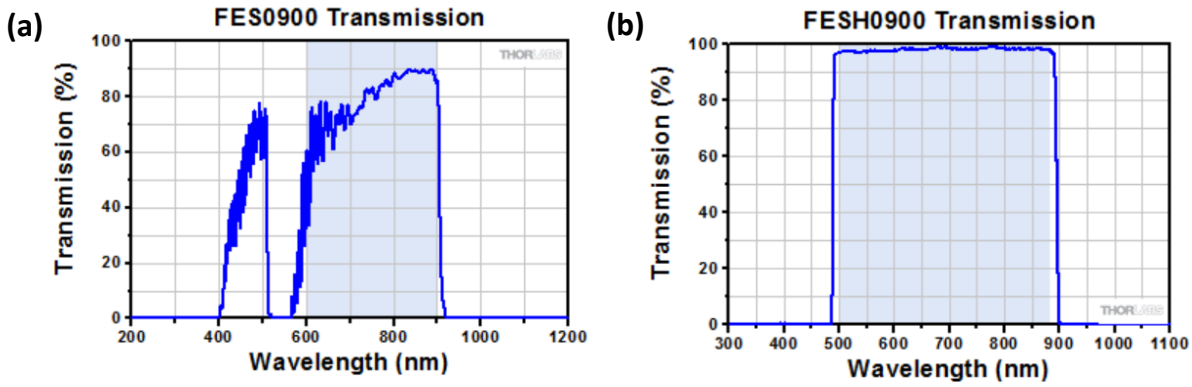

Figure B.4: Transmission profile of the two 900 shortpass filters (a) FES0900 (b) FESH0900, provided by Thorlabs, Inc.

For instance, the fluorescence is a bigger issue when observing low-intensity luminescence, as we have to use high power excitation with longer exposure time. In one of the projects, our goal was to observe up-conversion luminescence spectra around 600-700 nm range in a plasmonic nanocrystal system. Since the intensity of the up-conversion spectra of this material was weak, we conducted the experiment with longer exposure time (120 sec). But, in the resultant spectra most prominent feature was the Continuous Wave (CW) fluorescence spectra from the laser beam . Figure B.5 displays the fluorescence observed in a copper tape and frosted glass surfaces. The oscillations observed in the fluorescence spectra are as a result of the transmission profile of the 900 shortpass filter, placed before the spectrometer on the emission path (Fig. B.4(a)). In order to reduce the amount of fluorescence coming into the spectrometer, we introduced a set of longpass filters to the incident path. This includes 750 longpass (LP), 800LP, 850LP and 900LP filters (Fig. B.3). Even though this does not cover the full fluorescence spectrum, this covers the wavelength range we were interested in, for this particular experiment.

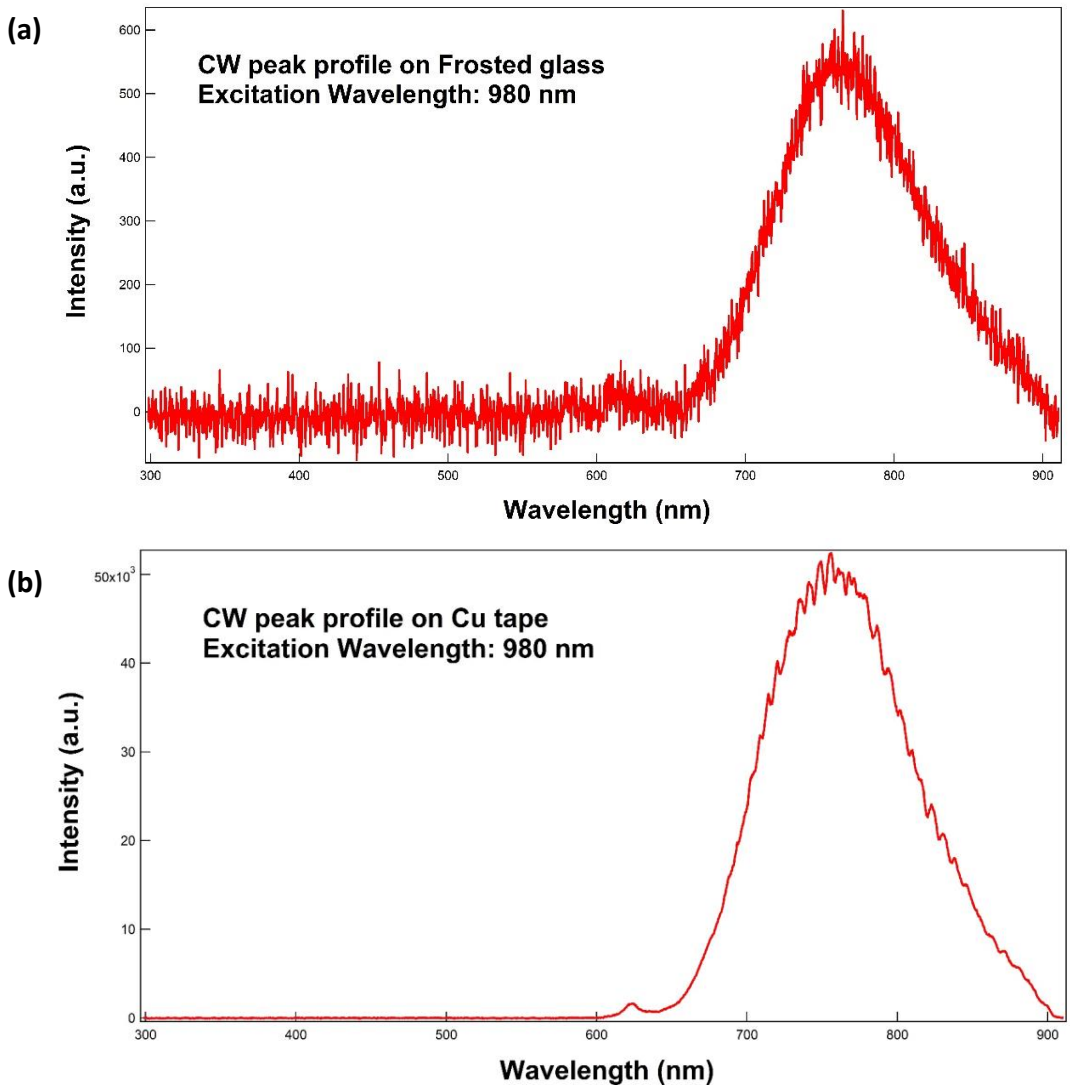

Figure B.5: Observed fluorescence from the Ti:sapphire oscillator on different reference samples (a) Cu tape (b) Frosted glass surfaces. Here the observed oscillations in (b) are resulted from the transmission profile of the 900 Shortpass filter (Fig. B.4), which was before the spectrometer.